Title

Water Mass Transport and Transformation in the Tropics and Arctic

Author

Alberty, Marion Sofia

Publication Date

2018

Peer reviewed|Thesis/dissertation

UNIVERSITY OF CALIFORNIA SAN DIEGO

Water Mass Transport and Transformation in the Tropics and Arctic

A dissertation submitted in partial satisfaction of the requirements for the degree
Doctor of Philosophy

in

Oceanography

by

Marion Sofia Alberty

Committee in charge:

Jennifer MacKinnon, Co-Chair
Janet Sprintall, Co-Chair
Ian Eisenman
Alexandre Ganachaud
Sutanu Sarkar
Shang-Ping Xie

2018

The Dissertation of Marion Sofia Alberty is approved, and it is acceptable in quality and form for publication on microfilm and electronically:

Co-Chair

Co-Chair

University of California San Diego

2018

EPIGRAPH

My life amounts to no more than one drop in a limitless ocean. Yet what is any ocean, but a multitude of drops?

— David Mitchell, Cloud Atlas

TABLE OF CONTENTS

LIST OF FIGURES

LIST OF TABLES

ACKNOWLEDGEMENTS

I would first like to thank my generous advisors, Janet Sprintall and Jennifer MacKinnon. They have been an overwhelming source of support, encouragement, and mentorship during this process. I would particularly like to thank them for fostering my scientific curiosity and allowing me to work on such a wide variety of topics; I cannot overstate how much I have valued this freedom to learn about and explore the many facets of oceanography. I would also like to thank and acknowledge Alexandre Ganachaud for hosting my time at LEGOS and serving as scientific advisor, mentor and committee member for my thesis. I also acknowledge my SIO/UCSD committee members, Sutanu Sarkar, Ian Eisenman, and Shang-Ping Xie, for their time, scientific feedback, and encouragement. Finally I would like to thank Sophie Cravatte for her work as a PI and co-author for SPICE, particularly the valuable insights and feedback she has contributed to every paper we have worked on together.

To Veronica, Kasia, Jess, Travis, Erica, Kevin, Greg, Chris, Mike, and the 2012 cohort, thank you for being some of my best teachers and friends. I also thank Cyril Germineaud for helping me feel at home in Toulouse and being a great friend and colleague. Thank you also to MOD and the SIO community for proving that one of the best parts of research is the people you get to work with. I would also like to extend a special thanks to the engineering and administrative staff at SIO, who keep this machine running and aren't thanked enough. Thank you also to the dedicated professionals at CAPS for listening and helping me to grow.

Lastly, I thank my family, who have always supported and believed in me. And to Dan, for sharing this journey with me.

Chapter Two, in full, is a reprint as it appears in the Journal of Geophysical Research: Oceans, 2017. Alberty, M. S., Sprintall, J., MacKinnon, J., Ganachaud, A., Cravatte, S., Eldin, G., Germineaud, C. and Melet, A. (2017) Spatial patterns of mixing in the Solomon Sea. *J. Geophys. Res. Oceans*, 122, doi:10.1002/2016JC012666. ©American Geophysical Union. Used with permission. The dissertation author was the primary investigator and author of this paper.

Chapter Three is currently being prepared for submission for publication of the material. Alberty, M. S., Sprintall, J., MacKinnon, J., Ganachaud, A., Cravatte, S., and Germineaud, C. The dissertation author was the primary investigator and author of this paper.

Chapter Four is currently being prepared for submission for publication of the material. Alberty, M. S., MacKinnon, J., Sprintall, J., Alford, M., Mickett, J., and Fine, E. The dissertation author was the primary investigator and author of this paper.

VITA

2011–2012	Undergraduate Student Researcher Cowen Lab, Cornell University
2012	Bachelor of Science in Civil Engineering Engineering, Cornell University
2012–2013	UC Regents First-Year Fellowship, George Mitchell Fellowship, Arete Associates–Jacobs Fellowship Scripps Institution of Oceanography, University of California San Diego
2014	Master of Science in Oceanography Scripps Institution of Oceanography, University of California San Diego
2015	STEM Chateaubriand Fellow Laboratoire d'Etudes en Géophysique et Océanographie Spatiales
2016–2018	NASA Earth and Space Fellowship Scripps Institution of Oceanography, University of California San Diego
2018	Doctor of Philosophy in Oceanography Scripps Institution of Oceanography University of California, San Diego

ABSTRACT OF THE DISSERTATION

Water Mass Transport and Transformation in the Tropics and Arctic

by

Marion Sofia Alberty
Doctor of Philosophy in Oceanography
University of California San Diego, 2018

Professor Jennifer MacKinnon, Co-Chair

Doctor Janet Sprintall, Co-Chair

This dissertation investigates the mechanisms which modulate the transport and transformation of water masses using observational techniques. Observations were made in the Solomon Sea during the Southwest Pacific Ocean Circulation and Climate Experiment (SPICE) (Chapters 2 & 3) and in the Canada Basin during the ArcticMix and Stratified Ocean Dynamics of the Arctic (SODA) experiments (Chapter 4).

The Solomon Sea connects the subtropical and equatorial Pacific, transporting water masses that supply the equatorial undercurrent and support eastern equatorial primary productivity. Chapter 2 investigates the spatial patterns of vertical diffusivity and dissipation of kinetic energy in the Solomon Sea, indirectly estimated from shipboard and Argo observations. Across the Solomon Sea, dissipation is strong relative to global estimates over the same latitudinal band and decreases by 2-3 orders of magnitude from the surface to 2000 m depth. Mixing along intermediate and deep isopycnals is indicative of tidally driven mixing. The sources of energy for thermocline mixing are temporally and spatially variable and observations do not resolve a clear relationship at this time.

Chapter 3 details the first, full-depth mooring transport time series from all three exit passages of the Solomon Sea: Vitiaz Strait, St. Georges Channel, and Solomon Strait. Vitiaz Strait is confirmed to supply the majority of transport (53%) toward the equator and is relatively steady in time. Transport through Solomon Strait supplies 34% of the total mean transport but dominates the total transport temporal variability. Thermocline transport variability in Solomon Strait is well described by the arrivals of the off-equatorial Rossby waves. St. Georges channel, which is typically not resolved in global and regional models due to the narrow channel width, supports 13% of total transport and seasonally exchanges water between the Bismarck Sea and Solomon Sea.

The Canada Basin has experienced greater than predicted losses in summer sea ice extent and the responsible dynamics are still an active area of research. Chapter 4 studies the influence of submesoscale dynamics on the transport of heat in the Canada Basin summer mixed layer using novel observations of mixed layer temperature and salinity from a bow chain. Simultaneous microstructure observations find asymmetric mixing across surface fronts. Horizontal wavenumber spectra from in-situ and satellite observations are used to infer upper ocean dynamics and evaluate satellite sea surface temperature products.

Chapter 1

Introduction

The equatorial and polar regions are climatic pulse points where we can measure rising temperature and, potentially, the dynamical effects of a changing climate. Equatorial changes in heat content have immediate consequences for regional and global weather patterns and thermosteric sea level rise. Enhanced vertical heat fluxes in the Arctic may indicate basin scale changes in water mass temperature and/or changing mixed layer dynamics in the region due to positive feedbacks associated with decreased sea ice cover. Understanding conditions at present and the relevant dynamics are crucial for accurately projecting the effects of climate change. However, these regions and the processes that modulate the transport and transformation of the waters within these areas are inadequately observed and understood. It is necessary to improve our understanding of these region in order to provide context for future changes to the climate system. In response, observational campaigns were designed and implemented to measure transport and transformation of water masses in the tropical Southwest Pacific and Arctic Ocean. Chapters 2 and 3 focus on observations of both water mass transformation and transport from the Solomon Sea in the Southwest Pacific, a region that connects equatorial and subtropical circulation. Chapter 4 investigates summer, surface mixed layer dynamics in the Beaufort Sea and the processes that lead to surface layer modification and vertical heat fluxes.

1.1 Mixing in the Solomon Sea

The low latitude western boundary currents of the South Pacific transit the Solomon Sea as they connect the South Pacific subtropical gyre and equatorial Pacific circulation (Ganachaud *et al.*, 2014). Water masses undergo significant modification as they are transported through the Solomon Sea before joining the Equatorial Undercurrent (EUC) as the primary source waters (Grenier *et al.*, 2011; Melet *et al.*, 2011). Both the strength of modification and transit time for a parcel to reach the equator will depend upon it's pathway through the Solomon Sea. While there exists some model-based evidence that suggests spatially varying water mass modification within the Solomon Sea (Melet *et al.*, 2011), most model-based studies have only focused on simulating transit time dependence on the different pathways (Grenier *et al.*, 2011; Qin *et al.*, 2016).

Water mass modification is the result of isopycnal stirring and diapycnal mixing. Diapycnal mixing is extremely heterogeneous in space and variable in time, reflecting the episodic nature of small scale processes that produce turbulence. While water property distributions are sensitive to the spatial patterns of mixing (Melet *et al.*, 2016), direct observations of turbulence are sparse and expensive (Waterhouse *et al.*, 2014). Methods that indirectly estimate mixing and turbulence using common observational platforms are thus a valuable tool for investigating the spatial patterns of mixing across the global oceans. Shipboard and autonomous observations of density and velocity profiles are leveraged to estimate the strength and patterns of mixing in the Solomon Sea in Chapter 2. The mean diapycnal mixing for the Solomon Sea is found to be relatively constant in depth but varying by 2-3 orders of magnitude along isopycnal layers. These patterns are well correlated with tide power input and topographic roughness below the thermocline indicating the importance of the internal tides for mixing at these depths.

1.2 Transport in the Solomon Sea

Regional geography constrains equatorward transport in the Solomon Sea such that waters enter through the open southern boundary and exit through three relatively deep and narrow channels (Tsuchiya, 1968; Tsuchiya *et al.*, 1989; Fine *et al.*, 1994). Synoptic shipboard observations have been fundamental in resolving the mean current pathways through the Solomon Sea but the variation of full depth transport through the three channels is not adequately resolved (Lindstrom *et al.*, 1987; Butt & Lindstrom, 1994; Fine *et al.*, 1994; Sokolov & Rintoul, 2000; Cravatte *et al.*, 2011; Gasparin *et al.*, 2012; Germineaud *et al.*, 2016). Gliders have been used to monitor the temporal variability of inflow through the southern boundary (Davis *et al.*, 2012), but these platfroms alias intraseasonal variability and cannot resolve the partitioning of transport between the straits. Moorings were previously deployed in one of the outflow channels (Murray *et al.*, 1995), but until now there were no long-term, simultaneous observation of transport in all three channels.

Direct observations of velocity from moorings concurrently deployed in all three channels are utilized to estimate mean transport and the temporal variability and partitioning of transport between the straits in July 2012 to March 2014 in Chapter 3. About half of the total transport exits the Solomon Sea through Vitiaz Strait as a strong, deep-reaching, and steady current with most of it's subinertial transport variability at seasonal timescales. While a smaller fraction of transport passes through Solomon Strait, the subinertial currents are highly variable in time with the largest fraction of variance at intraseasonal time scales.

1.3 Mixed Layer Dynamics in the Beaufort Sea

Finally, the focus is shifted to the Arctic where water mass transport and mixing rates are also of great interest as the Arctic Ocean warms and changes dramatically. The most dramatic of the changes observed in the Arctic is the loss of sea ice, particularly during the summer months. While simulations and projections from the Coupled Model Intercomparison Project Phase 5 (CMIP5) have improved at reproducing Arctic sea-ice extent observations, only 25% of simulations produce sea ice losses as strong or stronger than the observed losses over the satellite era (Stroeve *et al.*, 2012). Some advancements are credited to more physically accurate sea ice albedo parameterizations, but further work is needed to understand and accurately represent the Arctic upper ocean heat budget, specifically advection of heat and mixing (Flato *et al.*, 2013). Over the summer months in the Beaufort Sea, processes like sea ice melt, river runoff, and advection of Pacific summer water create a surface layer that is characterized by fronts in temperature and salinity. Understanding the influence of these lateral gradients on the surface mixed layer heat budget is of primary interest.

To this end, high resolution in-situ observations of temperature in the top 20 m were made in the Beaufort Sea in September 2015 and 2018 to investigate the influence of lateral gradients on vertical heat fluxes. To contextualize the synoptic observations of lateral variability, satellite sea surface observations are analyzed in a complimentary manner to investigate the inter-annual variability fronts in the Beaufort Sea. The results, discussed in Chapter 4, suggest a relationship between the variance of temperature at submesoscales and the strength of mixing within the surface mixed layer. Satellite observations also indicate seasonal variability of submesoscale temperature variance, leading to the hypothesis that the strength of vertical heat fluxes in the surface mixed layer varies on seasonal timescales as well.

Chapter 2

Spatial Patterns of Mixing in the Solomon Sea

2.1 Abstract

The Solomon Sea is a marginal sea in the southwest Pacific that connects subtropical and equatorial circulation, constricting transport of South Pacific Subtropical Mode Water and Antarctic Intermediate Water through its deep, narrow channels. Marginal sea topography inhibits internal waves from propagating out and into the open ocean, making these regions hot spots for energy dissipation and mixing. Data from two hydrographic cruises and from Argo profiles are employed to indirectly infer mixing from observations for the first time in the Solomon Sea. Thorpe and finescale methods indirectly estimate the rate of dissipation of kinetic energy (ϵ) and indicate that it is maximum in the surface and thermocline layers and decrease by 2-3 orders of magnitude by 2000 m depth. Estimates of diapycnal diffusivity from the observations and a simple diffusive model agree in magnitude but have different depth structures, likely reflecting the combined influence of both diapycnal mixing and isopycnal stirring. Spatial variability of ϵ is large, spanning at least two orders of magnitude within

isopycnal layers. Seasonal variability of ϵ reflects regional monsoonal changes in large-scale oceanic and atmospheric conditions with ϵ increased in July and decreased in March. Finally, tide power input and topographic roughness are well correlated with mean spatial patterns of mixing within intermediate and deep isopycnals but aren't clearly correlated with thermocline mixing patterns.

2.2 Introduction

Marginal seas have long been identified as regions that contribute significantly to kinetic energy dissipation and water mass modification (Munk & Wunsch, 1998; Price & Yang, 1998; Egbert & Ray, 2000). These seas are almost entirely separated from the open ocean by topographic boundaries, save for a few straits or channels which allow the exchange of water masses between the marginal seas and the open ocean. Tidal currents, enhanced by the topographic constrictions, pass over topography at the exchange points and generate internal waves. The propagation and spreading of the internal wave energy may be restricted by the islands and sills bounding the sea, leading to enhanced dissipation and mixing within the marginal sea and along the boundaries (St Laurent, 2008). The topographic properties of marginal seas make them unique regions of concentrated water mass modification, where water properties are transformed by lateral stirring and vertical mixing. In the South China Sea, for example, tidal flows through Luzon Strait produce energetic internal waves and strong turbulence throughout the region (St Laurent, 2008; Alford *et al.*, 2011,0).

The Solomon Sea is a marginal sea located in the equatorial Southwest Pacific that is important for tropical circulation and climate (Ganachaud *et al.*, 2014). The Solomon Sea is bordered by the main island of Papua New Guinea to the west, the islands New Britain and New Ireland of Papua New Guinea to the north, and the Solomon Islands to the east (Figure 2.1a). South Pacific Subtropical Mode Water

(STMW, $23.3 < \sigma_\theta < 26.7$) and Antarctic Intermediate Water (AAIW, $26.7 < \sigma_\theta < 27.5$) enter through the southern opening of the Solomon Sea with a total transport of about 26 ± 7 Sv (Figure 2.1b) (Fine *et al.*, 1994; Davis *et al.*, 2012; Gasparin *et al.*, 2012; Zilberman *et al.*, 2013; Germineaud *et al.*, 2016). The island chains constrain transport such that nearly all of the flow out of the Solomon Sea is accounted for in three relatively deep channels; Vitiaz Strait, St. Georges Channel and Solomon Strait (Lindstrom *et al.*, 1990; Murray *et al.*, 1995; Melet *et al.*, 2010*a*; Cravatte *et al.*, 2011).

Along the pathways through the Solomon Sea, the AAIW and STMW water masses undergo modification, characterized by a cooling ($\sim 0.5°$C) and freshening (~ 0.2 PSU) of the STMW, and a warming ($\sim 0.2°$C) and an increase in salinity (~ 0.04 PSU) of the AAIW along core isopycnals (Figure 2.2) (Germineaud *et al.*, 2016). Modeled power input into the internal wave field from the tides shows elevated baroclinic tide generation above ridges in Solomon Strait, the central portion of the sea and near the southern entrance region (Simmons *et al.*, 2004; Niwa & Hibiya, 2014), suggesting a rich tidally driven internal wave field within the Solomon Sea. Winds supply additional energy to the internal wave field by generating near-inertial waves. The full internal wave field supplies a potential source of energy for the observed water mass transformations as the breaking of internal waves leads to turbulent mixing. Eddy activity may also influence temporal variability and patterns of mixing (Whalen *et al.*, 2012) as the Solomon Sea has an energetic eddy field (Melet *et al.*, 2010*b*; Hristova & Kessler, 2012; Djath *et al.*, 2014), however the eddy-induced temporal variability of mixing remains to be explored.

The New Guinea Coastal Current/New Guinea Coastal Undercurrent system (NGCC/NGCU) of the Solomon Sea is the primary source of the Equatorial Undercurrent (EUC), acting as the direct connection between the South Pacific subtropical

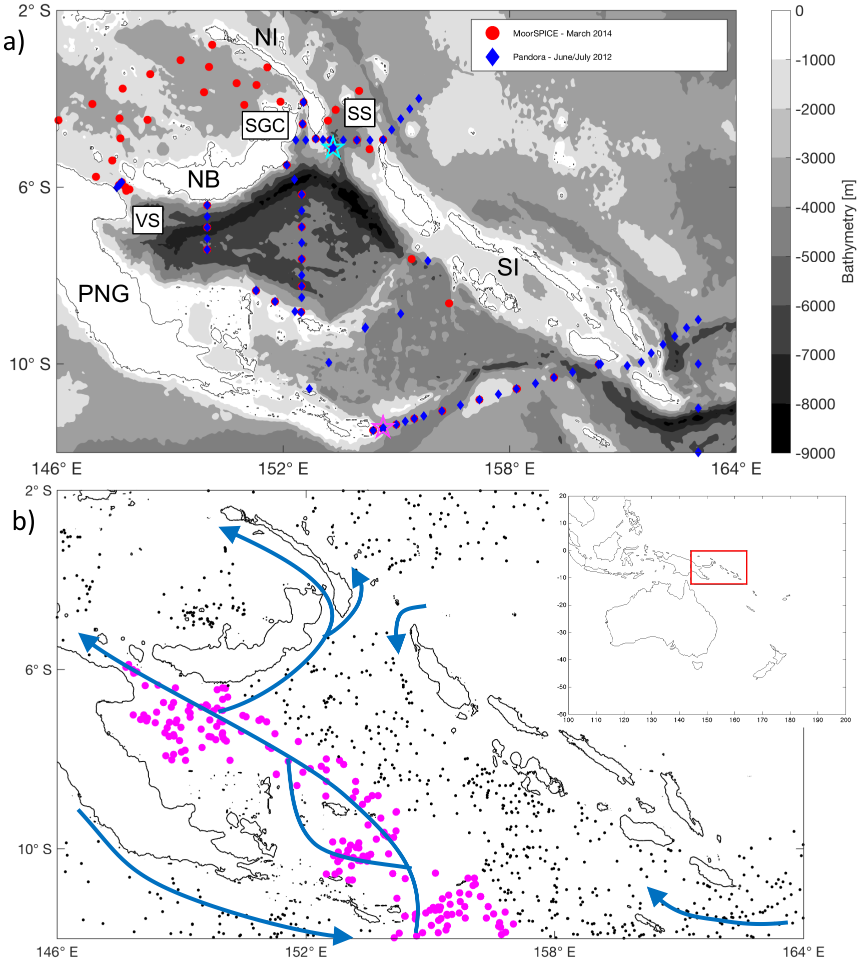

Figure 2.1: a) Map of Solomon Sea bathymetry including the main island of Papua New Guinea (PNG), New Britain (NB), New Ireland (NI) and the Solomon Islands (SI). The primary outflow channels, Vitiaz Strait (VS), St. George Channel (SGC), and Solomon Strait (SS), are noted. Red circles indicate CTD/LADCP cast locations for the MoorSPICE cruise (March 2014) while blue diamonds indicate cast locations for the Pandora cruise (June/July 2012). The cyan and magenta stars are the locations of Pandora station 42 and MoorSPICE station 50, respectively, which are referenced in Figure 2.5. b) The locations of the Argo and shipboard observations used to determine profiles of along-path mean diffusivity which are referenced in Figure 2.7 are shown as magenta dots and all other Argo observations shown as black dots. Blue lines are a schematic representation of the New Guinea Coastal Current/New Guinea Coastal Undercurrent (NGCC/NGCU) system that traverses the basin. The red box in the inset map indicates the location of the primary map within the Southwest Pacific.

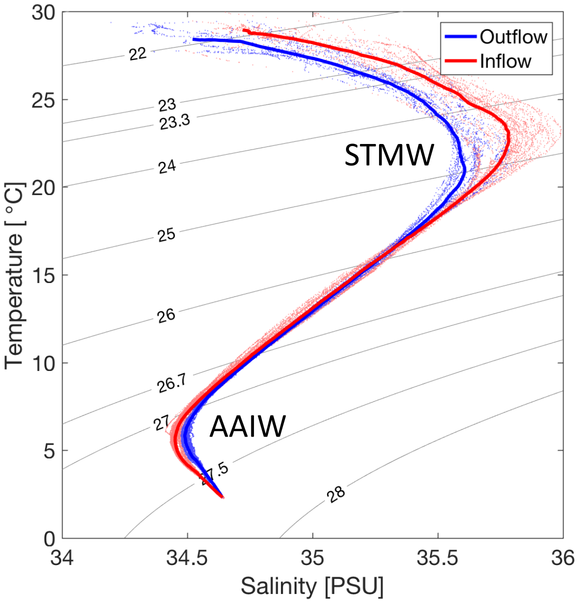

Figure 2.2: Mean temperature-salinity relationship of the Solomon Sea water mass inflow region (13 to 11° S, 153 to 156° E, red line) and outflow region north of Vitiaz Strait (7 to 4° S, 146 to 148° E, blue line) from Argo profiles. Individual observations are small dots in the corresponding color. STMW is indicated at the salinity maximum in the thermocline layer ($23.3 < \sigma_\theta < 26.7$) and AAIW is identified at the deep salinity minimum in the intermediate layer ($26.7 < \sigma_\theta < 27.5$)

gyre and equatorial Indo-Pacific circulation. The physical and biogeochemical water properties that are set by mixing in the Solomon Sea reach the surface when the EUC upwells in the tropical eastern Pacific Ocean (Tsuchiya *et al.*, 1989; Fine *et al.*, 1994; Ryan *et al.*, 2006; Kashino *et al.*, 2007; Grenier *et al.*, 2011; Qin *et al.*, 2016). The strong shear associated with the NGCC/NGCU is another potential source of energy for turbulent mixing within the Solomon Sea, likely generating shear instabilities along the water mass pathways.

The bulk of our knowledge about the quantitative transformation of water masses in the Solomon Sea is the result of several regional modeling studies (Melet *et al.*, 2011; Djath *et al.*, 2014). To model water mass mixing in the Solomon Sea, Melet *et al.* (2011) used a turbulent closure model and additionally the tide-based vertical diffusivity parameterization proposed by Koch-Larrouy *et al.* (2007) for the Indonesian Seas, a group of marginal seas with a topographically trapped internal wave field akin to the Solomon Sea. The parameterization of Koch-Larrouy *et al.* (2007) is adapted from that of St Laurent *et al.* (2002) with two important differences. The first difference is the assumption that all the energy added to the internal wave field by the tides within the marginal sea of interest is dissipated within that sea. The second difference is a shift in the vertical distribution of energy dissipation from maximum near the bottom of the water column to the thermocline with a dependence on stratification. The St Laurent *et al.* (2002) parameterization was developed for abyssal mixing and assumes that the bulk of internal waves will break over rough topography, thus near the bottom, while Koch-Larrouy *et al.* (2007) assumes dissipation to be maximum in the thermocline for marginal seas. The modeled downstream water properties for Melet *et al.* (2011) are in reasonable but not full agreement with regional observed water mass climatologies. Specifically, the modeled downstream salinity is biased low by 0.1 psu over the 24.5 - 27.5 σ_θ range compared to the observed properties, such that the erosion of STMW is too strong in the model while the deeper mixing of AAIW is under-represented. However, there were relatively few in-situ observations available for comparison at the time of the study. A recent study by Melet *et al.* (2016) has shown that processes that influence water mass properties such as ocean heat uptake and thermocline thickness are highly sensitive to the vertical distribution of mixing when simulated by climate models.

Understanding the strength, vertical and horizontal structure of mixing and its sources in the Solomon Sea is of importance for quantifying its influence on water mass transformation and impact on equatorial circulation. As of yet, no direct observations of energy dissipation or mixing have been made in the Solomon Sea. Here we use conductivity, temperature, depth (CTD) and Lowered Acoustic Doppler Current Profiler (LADCP) data from two survey cruises and the global Argo network to infer the rate of dissipation of turbulent kinetic energy and diffusivity throughout the Solomon Sea. In section 2.3 we outline the data sets and methods used for this analysis. The results and a comparison of the different methods and data sets are given in section 2.4, with a discussion of the results in section 2.5 and final remarks in section 2.6.

2.3 Data and Methods

2.3.1 Cruise Data

Hydrographic surveys of the Solomon Sea were completed in July 4 - August 1, 2012 (the cruise Pandora on the R/V l'Atalante) and February 28 - March 31, 2014 (the cruise MoorSPICE on the R/V Thomas G. Thompson) (Figure 2.1a). The objectives of the cruises were to observe the strength and pathways of the currents in the Solomon Sea, characterize the water masses, and deploy and recover nine moorings in three outflow channels of the Solomon Sea. The experiment was designed for the shipboard surveys to sample different phases of the monsoonal wind forcing as the Southeast Asian monsoon modulates physical processes in the Solomon Sea over a range of spatial scales. Strong and persistent southeasterly winds were observed during Pandora, while MoorSPICE occurred during a neutral phase of the monsoon wind cycle when the winds were weak and sporadic. During Pandora 164 CTD casts were taken, all with simultaneous velocity profiles acquired either from shipboard or lowered ADCP. All MoorSPICE casts also acquired simultaneous CTD and LADCP profiles, and 29 of the 82 casts were at repeat locations with Pandora casts for direct comparison. Further details about these cruises and data processing can be found in Germineaud *et al.* (2016).

As we do not have direct observation of turbulence (microstructure observations) or mixing (dye release experiments) we must use indirect methods to tease out the patterns of mixing. The turbulent dissipation rate (ϵ) was estimated from the cruise data sets using two distinct methods.

2.3.2 The Thorpe Scale Method

The first method estimates ϵ from a length scale of temperature and density overturns, known as the Thorpe scale (L_T), following the methods of Thorpe (1977) and Dillon (1982). This method takes advantage of an empirical relationship between L_T and the Ozmidov scale, $L_O = 0.8L_T$, and the Ozmidov relation, $L_O = \sqrt{\frac{\epsilon}{N^3}}$ where N is the buoyancy frequency, to estimate the expected dissipation rate of an observed overturn. Outside of the overturn regions L_T is zero and thus ϵ by way of the Ozmidov relation is also zero. Galbraith & Kelley (1996) provide a thorough description of the method and its caveats.

Our analysis uses both temperature and potential density profiles from shipboard CTD casts at 0.25 m and 1 m vertical resolution, respectively. The vertical resolution of each quantity is determined by the sensor's effective temporal resolution due to spectral noise (4 Hz for temperature and 1 Hz for conductivity) and the CTD fall rate (1 m/s). While density is the optimal quantity to observe overturns, the higher vertical resolution of temperature observations provide an opportunity to estimate L_T from overturns with smaller overturn heights (z_{OT}) that cannot be resolved using density observations. As some overturns in temperature may be stable in density, the Turner angle (θ_T) is calculated which quantifies the relative influence of temperature and salinity on the density gradient as degrees of rotation. Regions of cold, fresh water over warm, salty water that are statically stable have $-90^\circ < \theta_T < -45^\circ$ and are ignored when calculating Thorpe scales from temperature profiles in an effort to be conservative. Using the potential density and temperature observations, two profiles of ϵ are generated: the first simply consists of estimates made using overturns found in profiles of potential density, while the second is a composite made from the first estimate of ϵ and additionally incorporates ϵ from temperature overturns with smaller z_{OT} that cannot be resolved by potential density observations.

2.3.3 The Finescale Method

The second method of estimating ϵ follows the finescale parameterization described in Kunze *et al.* (2006) and Polzin *et al.* (2014). The method relies upon several key physical assumptions, primarily that the turbulent dissipation rate in the ocean is driven by the internal wave field and that energy cascades downscale via wave-wave interactions to turbulent length scales. The parameterization uses observations of LADCP shear and CTD strain to quantify the strength of the internal wave field and estimates ϵ by comparing the observed wave field to the theoretical Garrett-Munk (GM) internal wave field in wavenumber spectral space.

Two criteria are applied to remove segments of data in which the shear or strain are likely dominated by processes other than internal waves, and so violate the primary assumption of the method. The first criterion (C1) removes density and velocity observations within the mixed layer where surface and mixed layer processes dominate the shear and strain fields. The mixed layer depth is defined as the depth at which density is 0.03 kg m^{-3} greater than the density measured at 10 m (de Boyer Montégut *et al.*, 2004). The second criterion (C2) removes data from within the strong current cores of the NGCC/NGCU system. The parameterization is not suited for use in a strongly sheared boundary current where it is not possible to differentiate between the shear and strain due to the current versus that due to internal waves (Polzin *et al.*, 2014). All shipboard LADCP was used to construct a mean current core, centered around current maximums. The average profile of the current core has a velocity maximum $\sim$ 35 cm s^{-1} in the top 1000 m. C2 removes all data above sampled current core. C2 also removes data 100 m below the current core because, on average, the current velocity decreases by 50% 100 m below the local maximum within the NGCC/NGCU system. Although it is expected that the finescale method will perform poorly in regions with large mean shear due to currents, nonetheless Winkel *et al.* (2002) find that using the total shear in the finescale parameterization often is a better predictor of ϵ. Estimates of ϵ will be presented in section 2.4 with and without C2 applied, as the true dissipation likely lies between these two estimates. C1 and C2 were only applied when using the finescale method and not enforced when using the Thorpe scale method.

The finescale method applied to a sample cast from the Pandora cruise is shown in Figure 2.3 and serves as a visual outline of the method. Simultaneous profiles of velocity and density (Figure 2.3a) with typical vertical resolutions of 10 m and 1 m, respectively, are broken into 320 m long, half-overlapping segments. For each segment, we estimate isopycnal strain, $\xi_z = \frac{N^2 - N_{fit}^2}{\overline{N^2}}$, and buoyancy frequency normalized shear, $\frac{\mathbf{U_z}}{\overline{N}}$, where N_{fit} is a cubic fit of the buoyancy frequency, $\overline{N}$ is the segment-averaged buoyancy frequency, and $\mathbf{U_z} = (\frac{\partial u}{\partial z} + i\frac{\partial v}{\partial z})$ (Figure 2.3b). The spectra of $\frac{\mathbf{U_z}}{\overline{N}}$ and ξ_z are calculated in wavenumber space (k_z) for each segment (Figure 2.3c), and are corrected for high wavenumber attenuation due to signal processing and first differencing (Figure 2.3d, also see Appendix 2.A for full description). The corresponding GM spectrum is calculated for each segment (Figure 2.3c-d, black lines) and all spectra are integrated over appropriate wavenumber ranges. The appropriate wavenumber ranges are described in full in Appendix 2.A. The GM spectrum functions as a non-dimensional, standard unit that is used to quantify the strength of the observed internal wave field relative to the theoretical GM spectra.

The parameterization then uses the variance from the observed and GM strain spectra with additional adjustments for latitude, local stratification, and a regional ratio of shear-to-strain variance to estimate ϵ for each segment (Figure 2.3e). Estimates of ϵ using the Thorpe scale method are also shown as gray dots in Figure 2.3e for direct comparison. A more detailed description of the finescale method and the choices made in the analysis can be found in Appendix 2.A.

2.3.4 Argo Data

This study additionally utilized an Argo data set consisting of 733 profiles from 77 floats with Iridium communications systems from January 2013 to June 2016 that is within the study region of 2°S, 146°E to 12°S, 164°E (Figure 2.1b). The Argo program is an international effort that maintains over 3000 freely-drifting, profiling floats that measure the temperature and salinity of the ocean's upper 2000 m. Turbulent dissipation estimates are obtained from isopycnal strain using temperature, salinity and pressure measured by Argo floats and the mean observed ratio of shear-

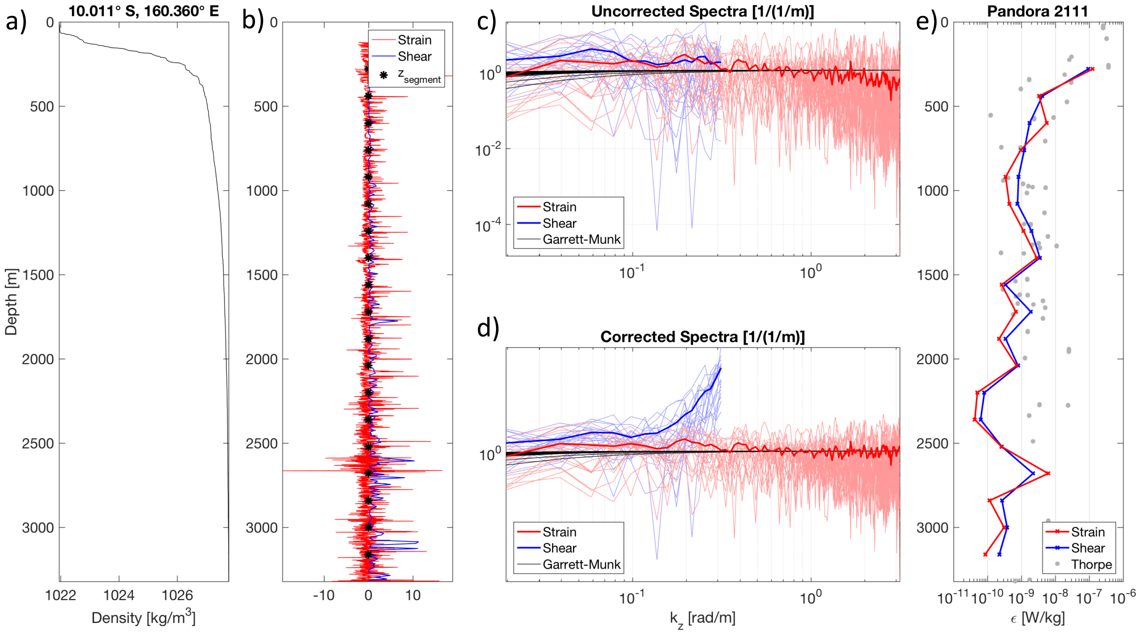

Figure 2.3: a) A density [kg m^{-3}] profile at 10.011° S, 160.360° E as a function of depth. b) The profile of LADCP- and CTD-derived normalized shear (blue line) and CTD-derived strain (red line) during the Pandora cruise (both quantities are unitless). Black stars mark the center point of 320 m segments for which the spectra was used to generate an estimate of dissipation. c) Uncorrected normalized shear spectra (blue) and strain spectra (red), where the thin lines are from individual segments and the thick lines show the cast mean. The range of GM spectra are in black. d) Normalized shear spectra (blue) and strain spectra (red) that have been corrected for high wavenumber attenuation. The line and color scheme is identical to that of panel c. e) Estimated dissipation [W kg^{-1}] as a function of depth [m] from the Thorpe scale method (gray) and the finescale shear (blue) and strain (red) parameterization.

to-strain variance from the shipboard data following the methods detailed in Whalen *et al.* (2012). The Argo profiles of ξ_z were broken into 150 m long, half-overlapping segments with a vertical resolution of 2 m. Shorter segment-lengths (150 m compared to 320 m) were utilized for Argo to maximize the number of ϵ estimates per profile. This efficiency is due to the smaller wavenumber range required to integrate strain spectra compared to the larger wavenumber range required for simultaneous shear and strain observations (See Appendix 2.A).

2.3.5 Comparative Analysis

To facilitate comparison between the different methods and data sets, mean profiles were created by averaging all the estimates of ϵ in 320 m bins from the surface to 2240 m. For the finescale method, mean profiles were generated from dissipation estimates that used strain spectra for more direct comparison with the Argo derived dissipation estimates. The maximum depth of 2240 m was chosen to include all the Argo observations, as the floats typically have a maximum diving depth of 2000 m. Error bars were constructed from the 90% bootstrap confidence level of the mean for each depth bin.

To determine spatial patterns of ϵ, the median finescale dissipation is computed from combined cruise and Argo data sets in $\frac{1}{2}^\circ$ latitude by $\frac{1}{2}^\circ$ longitude grid boxes over density ranges corresponding to the thermocline ($STMW, 23.3 < \sigma_\theta < 26.7$), intermediate ($AAIW, 26.7 < \sigma_\theta < 27.5$), and deep ($27.5 < \sigma_\theta$) layers. The isopycnals that delineate each layer approximately correspond to 85 m, 400 m, and 1270 m depth in the Solomon Sea. Each grid cell has at least 3 estimates. Supplementary data sets are utilized to investigate potential sources of spatial variability. Topographic roughness was computed as the variance of bathymetry over $\frac{1}{2}^\circ$ latitude by $\frac{1}{2}^\circ$ longitude grid boxes using bathymetry from ETOPO1 1 Arc-Minute Global Relief Model (Amante

& Eakins, 2009). This analysis also utilizes the energy input into the baroclinic tide from the barotropic tide from FES2004. FES2004 was produced by LEGOS and CLS Space Oceanography Division and distributed by AVISO, with support from CNES (http://www.aviso.altimetry.fr/).

2.4 Results

The mean profiles of ϵ for the combined July 2012 Pandora and March 2014 MoorSPICE cruises using the Thorpe scale method are enhanced in the top 320 m at $1.9 - 2.3 \times 10^{-7}$ [W kg^{-1}], decreasing with depth to $2.7 - 2.9 \times 10^{-9}$ [W kg^{-1}] at 2000 m (Figure 2.4a, red lines). While the mean profile of ϵ derived from the composite Thorpe scale estimates (dotted red line) contains 6.6 times as many overturns as the mean profile from the density Thorpe scale estimate (solid red line), the resulting slight enhancement of ϵ is not statistically significant. The mean profile of ϵ for the combined cruise data set using the finescale method with C1 and C2 applied is shown in Figure 2.4a (dotted black line) with a maximum ϵ of 4.1×10^{-8} [W kg^{-1}] in the upper 320 m decreasing to 2.0×10^{-9} [W kg^{-1}] below 2000 m depth. The mean profile of finescale ϵ without C2 applied (Figure 2.4a, dashed black line) primarily differs from the mean profile of finescale ϵ with C1 and C2 applied above 1000 m depth with a local max of 1.2×10^{-7} [W kg^{-1}]. The mean profile of ϵ from the Argo data set using the finescale method (Figure 2.4a, solid black line) has a vertical structure that is similar to the shipboard finescale profile below 320 m, but is biased low with a deep minimum of 2.2×10^{-10} [W kg^{-1}] and maximum in the top 320 m of 5.7×10^{-8} [W kg^{-1}]. Depth-mean ϵ from Argo strain within the Solomon Sea is elevated by a factor of 8 compared to ϵ from Argo strain in the Pacific along a similar latitudinal band (12° N to 12° S) (not shown, Whalen *et al.* (2012)). The mean profile of ϵ in the Solomon Sea from Argo is elevated by a factor 2-10 over the top 2000 m

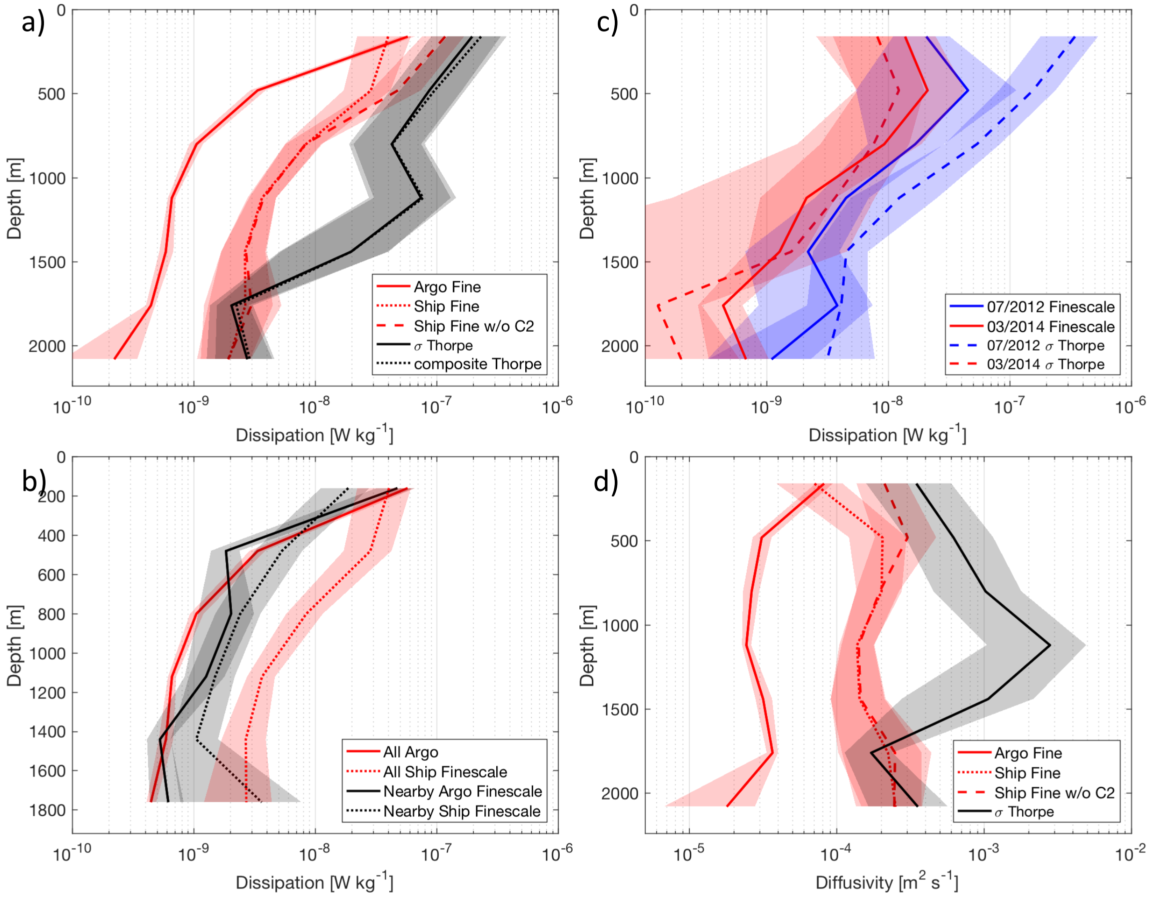

Figure 2.4: a) Mean dissipation profiles for Argo strain observations using the finescale method (solid black line) and the combined cruise data using strain observations with the finescale method (dotted black line), density (solid red line) and temperature (dotted red line) observations with the Thorpe scale method. b) Mean dissipation profiles from all available Argo (solid red line) and shipboard (dotted red line) finescale observations and from a subset of data using pairs of Argo (solid black line) and shipboard (dotted black line) casts that were withing 25 km of each other. c) Mean profiles of dissipation only from stations repeated during both the Pandora (blue) and MoorSPICE (red) cruises using the finescale parameterization (solid) and the Thorpe scale method with temperature (dashed). d) Profiles of mean diffusivity from the Argo strain observations using the finescale method (solid black line), the combined cruise data using strain observations with the finescale method (dotted black line), and the combined cruise density (solid red line) observations with the Thorpe scale method. Shading around all lines give the 90% bootstrap confidence intervals for each mean.

depth compared to that of the equatorial Pacific, though the open-ocean profile has very similar vertical structure with ϵ maximum near the surface and decreasing with depth.

The comparatively weak maximum in the cruise finescale profile compared to the Argo finescale profile is largely due to C2 described in section 2.3, that reduces the mean ϵ from the cruise finescale estimates in the top 320 m by a factor of 3, but does not significantly affect deeper means. The overall low bias of the Argo mean profile compared to the cruise data is due largely to sampling patterns of the two data sets; cruise data is concentrated around regions of rough topography within the NGCC/NGCU system (Figure 2.1a) while Argo data is more evenly dispersed throughout the region (Figure 2.1b). The bias due to spatial sampling accounts for 83% of the RMS difference between the mean profiles of ϵ below 320 m. The bias was determined using a subset of the data that only contains pairs of Argo and cruise casts within 25 km of each other (Figure 2.4b). The remaining fraction of the RMS difference is likely due to temporal variability of the sampling and dynamical processes.

The local maximum found near 1200 m in Thorpe scale ϵ (Figure 2.4a, red lines) is the largest discrepancy in profile structure between the Thorpe and finescale methods. This local maximum is the result of two stations where repeated casts resolved the presence and evolution of two relatively large overturns, with large z_{OT} ($\sim$ 150 m), weak N ($\approx$ 0.002 rad/s) and large L_T ($\approx$ 15 m) (Figure 2.5a & e). Both stations lie on the edges of the basin and within the strongly sheared boundary currents (Figure 2.1a, cyan and magenta stars). While the outer scales of the overturns at each stations are quite similar, the vertical structure of the density at each station is visually distinct, suggesting that different mechanisms may be responsible. A potential mechanism could be shear instability due to the NGCC/NGCU system.

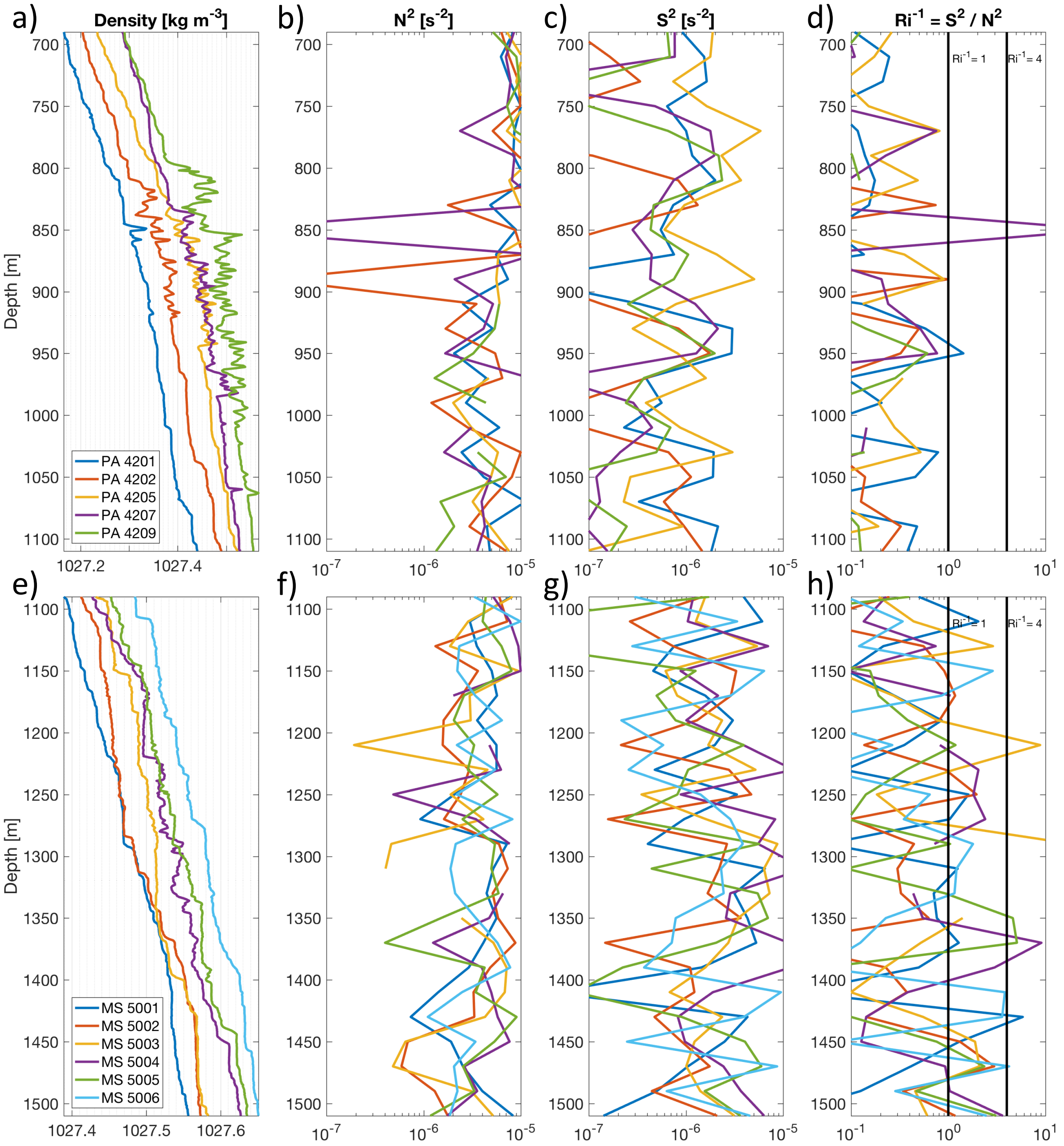

Figure 2.5: Density (a & e), N^2 (b & f), shear squared (S^2) (c & g), and inverse Richardson number (Ri^{-1}) (d & h) for the repeat casts from a-d) Pandora station 42 (5.1° S, 153.3° E) and e-h) MoorSPICE station 50 (11.5° S, 154.6° E). There is an a) 0.03 and e) 0.01 kg m^{-3} offset between successive density profiles for clearer visualization of the developing overturns.

To investigate, density and velocity are smoothed and sub-sampled to 20 m vertical resolution and used to calculated N^2, shear squared (S^2) and inverse Richardson number ($Ri^{-1} = \frac{S^2}{N^2}$). When $Ri^{-1} \geq 4$ the shear is sufficient to overturn stratification and is suggestive of shear instability. A critical Ri^{-1} is necessary for the generation of shear instabilities but alone is not a sufficient condition. Stratification is quite similar between the two stations with the overturn region in MoorSPICE having slightly lower values of N^2 compared to Pandora, though the overturns occur at different depths (Figure 2.5b & f). However S^2 is an order of magnitude larger at the MoorSPICE overturn compared to the Pandora station (Figure 2.5c & g), resulting in more instances where $Ri^{-1} \geq 4$ (Figure 2.5d & h). These results predict, but do not guarantee, that shear instabilities are driving the observed density overturns at the MoorSPICE station. The shear field present in the Pandora observations is insufficient at this scale to generate shear instabilities, though it may be sufficient at smaller, unresolved scales. The Pandora density overturns may be driven by a different mechanism.

The dissipation associated with these large overturns was 2-3 orders of magnitude larger than the dissipation estimated by the finescale method over the same depth ranges. These overturns thus skew the Thorpe mean dissipation for all shipboard data between 1000-1500 m depth. Removal of the casts in question from both the finescale and Thorpe mean profiles reduces the mean difference between the profiles by $\sim 30\%$ and the sub-surface maximum in the mean Thorpe profile disappears (not shown). Mater *et al.* (2015) found that L_T/L_O increases with increasing overturn size leading to overestimates of ϵ by the Thorpe scale method, however when profiles of ϵ from Thorpe and microstructure observations are depth-averaged over time Thorpe ϵ is biased high but within an order of magnitude compared to microstructure ϵ. Thus large and strong overturns may bias estimates of ϵ high when using the Thorpe method, nonetheless these overturns are contributing to the dissipation of energy in a way that the finescale method is not able to capture.

Temporally variable dynamics of the Solomon Sea, such as monsoonal winds, likely vary ϵ seasonally by generating near-inertial waves and modulating upper ocean dynamics. To explore this seasonal variability, the mean profiles of ϵ for each method and cruise are compared using the 21 profiles from repeated stations (Figure 2.4c). Limiting the data to only repeated locations should reduce the differences between the mean profiles that could be attributed to spatial variability, potentially highlighting the temporal variability of ϵ. The finescale depth-average of ϵ for the top 2000 m is elevated by a factor of 2.3 during the July 2012 cruise relative to the March 2014 cruise (Figure 2.4c, solid lines). The mean finescale profile for July is higher at all depths compared to March. Mean dissipation profiles from Argo observations averaged over the same months find a consistent though weaker relationship with mean July dissipation a factor of 1.5 larger than in March (not shown). Depth-averaged ϵ from density overturns using the Thorpe method also show July 2012 dissipation rates are elevated relative to March 2014 but with depth-averaged ϵ 16.0 times larger in July 2012 (Figure 2.4c, dashed lines). The mean Thorpe profile for July is higher above 1000 m and below 1500 m relative to the March observations. The composite Thorpe scale estimate for March 2014 is significantly larger in the top 320 m compared to the density estimate (not shown) and depth-averaged ϵ is 13.1 times larger in July 2012.

As the barotropic tide passes over rough topography, internal tides are generated and break, enhancing dissipation and providing another source of temporal variability at higher frequencies than seasonal variability. Fortnightly modulation of mixing near rough or abrupt topography due to the spring-neap cycle of the barotropic tide has been well resolved in process studies (St. Laurent *et al.*, 2001; Klymak *et al.*,

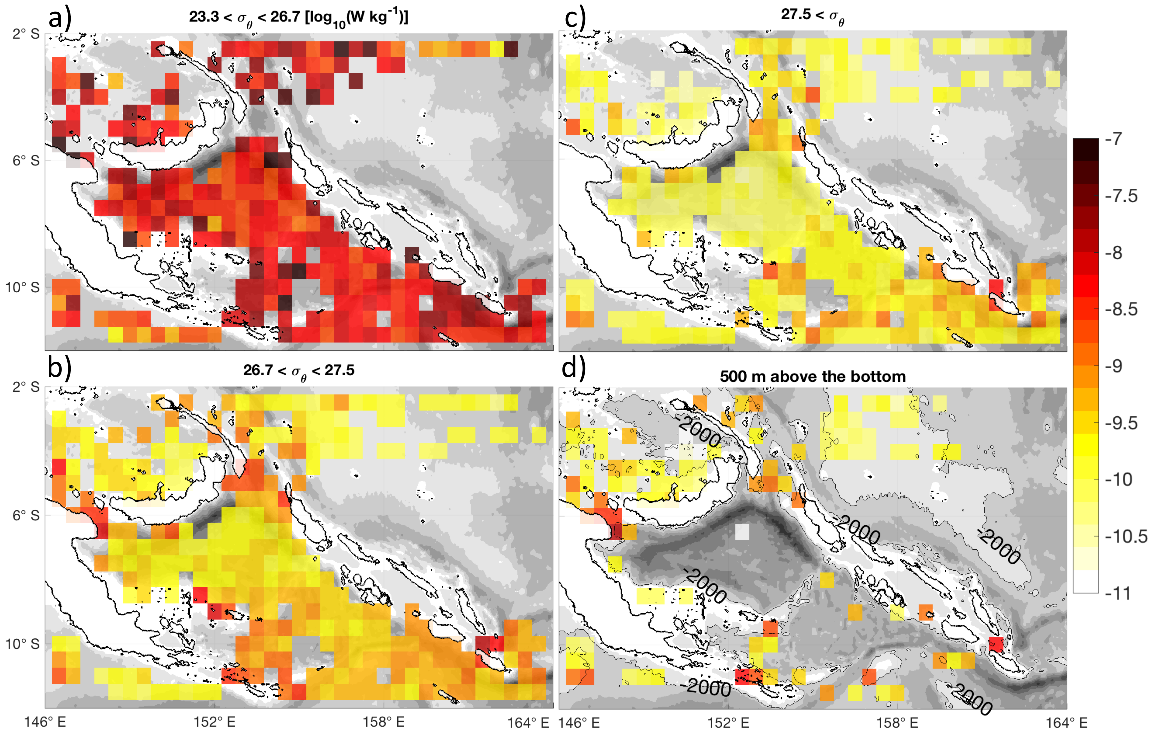

Figure 2.6: The log of median dissipation [W kg^{-1}] from combined cruise and Argo data sets using the finescale method in a) the thermocline which contains STMW ($23.3 < \sigma_\theta < 26.7$), b) the intermediate layer which contains AAIW ($26.7 < \sigma_\theta < 27.5$), c) the deep layer ($27.5 < \sigma_\theta$), and d) within 500 m above the bottom at $\frac{1}{2}^\circ \times \frac{1}{2}^\circ$ resolution. Bathymetry is contoured at 1000 m intervals and the coast is drawn in black. The 2000 m isobath is also contoured and labeled in black for d).

2006; Levine & Boyd, 2006; Klymak *et al.*, 2008). These process studies suggest that the fortnightly modulation of ϵ is confined in space to near generation sites, with ϵ relaxing to background levels hundreds of meters above the bottom and tens of kilometers away. The relationship between finescale ϵ from observations within 500 m of the bottom and the strength of the barotropic tide predicted by the TPXO model (Egbert & Erofeeva, 2002) is investigated. A positive but statistically insignificant relationship ($R^2 = 0.1$) is found between these quantities. While ϵ near rough topography is likely modulated at tidal frequencies, only one third of the finescale profiles are full depth with the majority of those observations over relatively smooth topography making such a signal difficult to detect.

Now we will focus on the two-dimensional patterns of ϵ over three isopycnal layers and within 500 m of the bottom. Spatially the clearest pattern is the decreasing magnitude of finescale ϵ with increasing density and thus depth (Figure 2.6). In the thermocline layer (Figure 2.6a), the strongest dissipation is concentrated at the edges of the Solomon Sea with the weakest dissipation south of New Britain in the interior. At intermediate isopycnals (Figure 2.6b), dissipation is enhanced around Vitiaz and Solomon Straits and on the western margin where topography is highly variable. Away from the margins, a north/south asymmetry in the magnitude and spatial variability of dissipation is visible in both the intermediate and deep isopycnal ranges (Figures 2.6b and 2.6c), likely related to the north/south asymmetry in topographic roughness. For these layers there is also a marked difference in the spatial variability of dissipation within the Solomon Sea, compared to the relative homogeneity of the dissipation in the equatorial band of observations outside of the Solomon Sea from 2°S, 155°E to 4°S, 164°E. Due to the deep nature of the Solomon Sea (bottom depths ¿ 2000 m in ¿ 50% of the sea), only one third of the total observations extend to the bottom and so can be utilized to investigate near-bottom patterns of ϵ (Figure 2.6d). In those profiles that do extend to the bottom, enhanced dissipation is observed over regions of abrupt or rough topography while lower ϵ is associated with smooth and flat topography.

2.5 Discussion

The Solomon Sea is a marginal sea where energetic currents and tides encounter abrupt and rough topography. Observations from two field campaigns and the Argo database were used to estimate ϵ throughout the region via the Thorpe scale method and finescale parametrization. The mean profile of ϵ in the Solomon Sea is maximum near the surface ($4.1 - 23 \times 10^{-8}$ [W kg^{-1}]) and decreases with depth ($2.2 - 29 \times 10^{-10}$ [W kg^{-1}]) (Figure 2.4a). Depth-mean ϵ in the Solomon Sea is elevated by a factor of 8 relative to the rest of the equatorial Pacific using Argo strain observations. Spatial patterns of ϵ vary up to two orders of magnitude over isopycnal layers that contain the STMW and AAIW within the Solomon Sea (Figure 2.6). Shipboard and Argo data sets suggest seasonal variability of ϵ with elevated dissipation coincident with strong monsoonal winds (Figure 2.4c), though the full seasonal cycle of dissipation remains unresolved by this data set.

2.5.1 Thorpe vs. Finescale Method

Because the Thorpe and finescale methods estimate ϵ using different assumptions, it is not entirely surprising that when the methods are applied to the same data set the results differ slightly. The Thorpe scale method relies entirely on the presence of density overturns within a water column, regardless of the source of the instability. Thus the estimate can quantify ϵ resulting from a suite of physical processes, including but not limited to breaking internal waves. The finescale method, on the other hand, assumes the observed shear and strain over vertical length scales of internal waves is solely due to internal waves and that the wave field will drive a particular rate of dissipation. Thus any shear and strain from other physical processes with similar vertical length scales may bias the estimated ϵ using the finescale method to higher values. While great care is taken to reduce this bias, particularly in the upper ocean where contamination from mesoscale and smaller scales is greatest, there is likely some residual contamination that is difficult to avoid. Even when well executed, the method only attempts to predict dissipation due to the energy in the internal wave field, which is not the only energy source supplying dissipation and mixing (shear instabilities within the boundary currents present one additional source).

Thus we might expect the methods to agree best in regions where internal waves are the dominant process supplying energy for dissipation, such as in the deep ocean. Indeed, the estimates of mean ϵ from the cruise data converge below 1500 m and fall within the 90% boot-strap confidence intervals (Figure 2.4a). Over the entire water column, Thorpe scale estimates of ϵ are on average a factor of 3 larger than finescale strain estimates. Similarly in the Drake Passage Thompson *et al.* (2007) found Thorpe scale estimates were consistently elevated by a factor of $2-3$ compared to finescale estimates from the same data set. These results indicate that the Solomon Sea internal wave field is an important source of energy for dissipation and mixing. However in the top 1500 m when Thorpe estimates exceed finescale estimates by more than a factor of 3, other processes may also contribute to energy dissipation.

2.5.2 Method Uncertainties

While the shipboard observations using the Thorpe and finescale methods suggest elevated dissipation in the surface and thermocline with weaker dissipation in the deeper layers, there remains uncertainty in the magnitude of these estimates relative to the 'true' ϵ. The most accurate observations of ϵ come from shear microstructure profilers, which resolve shear at dissipative length scales, enabling direct estimates of ϵ assuming isotropic turbulence (Oakey, 1982). Two regional studies in the Southern Ocean (Frants *et al.*, 2013; Waterman *et al.*, 2014) use simultaneous observations of microstructure shear and CTD density to compare microstructure derived ϵ with Thorpe and finescale estimates and so offer guidance as to expected differences.

Frants *et al.* (2013) compared different estimates of ϵ made in two energetically different locations: a smooth abyssal plain in the Southeastern Pacific and the highly energetic Drake Passage. Agreement between Thorpe and microstructure dissipation was best in the strongly dissipative Drake Passage, where Thorpe estimates were generally biased high but differed from microstructure by less than an order of magnitude. In the quiescent Southeastern Pacific, Thorpe estimates were consistently biased high by at least one order of magnitude in the top 600 m with a smaller but still statistically significant bias below. The low stratification of the Southern Ocean decreases the signal-to-noise ratio when quantifying overturns and contributes to the high bias of the Thorpe scale ϵ. Finescale and microstructure estimates generally agreed within a factor of 2-3 for both locations and captured regional patterns found in the microstructure observations better than Thorpe scale estimates.

Waterman *et al.* (2014) found that at depths of 1500 m above the bottom the ratio of shear microstructure ϵ to finescale strain ϵ fell within the factor of two uncertainty predicted for the finescale method by Gregg (1989) and Polzin *et al.* (1995). For a subset of locations, the finescale method systematically over-predicted ϵ within 1500 m of the sea floor. These locations were characterized by high Froude numbers, strong near-bottom velocities and elevated topographic roughness, suggesting the generation and presence of lee waves. It is not surprising then that the finescale parameterization failed to accurately predict ϵ at these locations given that the shear and strain fields are likely dominated by lee waves and wave-mean flow interactions as opposed to freely propagating internal waves for which the finescale parameterization is designed.

These studies suggest that the Thorpe method, particularly in regions of low stratification, gives high-biased estimates of ϵ. In regions of strong stratification, like the Solomon Sea, where the signal-to-noise ratio of density observations is large, accuracy of the Thorpe scale ϵ and agreement between Thorpe scale and microstructure ϵ are expected to improve. Koch-Larrouy *et al.* (2015) find good agreement between the Thorpe and microstructure methods in the Indonesian Seas using station-averaged profiles, where stratification is also strong. Finescale estimates qualitatively match regional patterns of microstructure derived ϵ and quantitatively agree within a factor of 2-3, except in regions where processes aside from internal waves contribute significantly to the observed shear and strain fields. The 'true' mean profile of dissipation from the cruise data likely lies somewhere in between the finescale and Thorpe method estimates, with maximum ϵ near the surface $O(10^{-7})$ [W kg^{-1}] and decreasing in magnitude to $O(10^{-9})$ [W kg^{-1}] by 2000 m depth.

Whalen *et al.* (2015) compares finescale strain estimates of ϵ using Argo profiles with microstructure observations at six dynamically diverse locations. In this study microstructure and Argo finescale observations were not taken simultaneously, but rather with measurements separated over a range of time scales. For 96% of the observations, mean microstructure and finescale estimates differ by a factor of 2-3, consistent with the findings of Frants *et al.* (2013) and Waterman *et al.* (2014). Thus we expect the regional patterns shown in Figure 2.6 to be representative of internal wave driven dissipation variability in the Solomon Sea. Furthermore we would expect mean microstructure observations to match mean finescale estimates within a factor of 3 for all Solomon Sea measurements outside of the NGCC/NGCU system.

2.5.3 Diffusivity

While the rate of dissipation of kinetic energy is an important quantity, particularly when investigating ocean energy budgets, a related and equally important quantity is diapycnal eddy diffusivity (κ). Practically, κ is estimated using the Osborn relation (Osborn, 1980), $\kappa = \gamma \frac{\epsilon}{N^2}$, which assumes that the dissipation of kinetic energy by turbulence results in diapycnal mixing with an empirically determined mixing efficiency (γ) of 0.2. The value of γ has been shown to vary over the life cycle of instabilities and the resulting turbulence. However 0.2 represents the overall efficiency well and is suitable for use in averaged observations where it is not possible to determine at what stage in the turbulence life cycle observations were made (Peltier

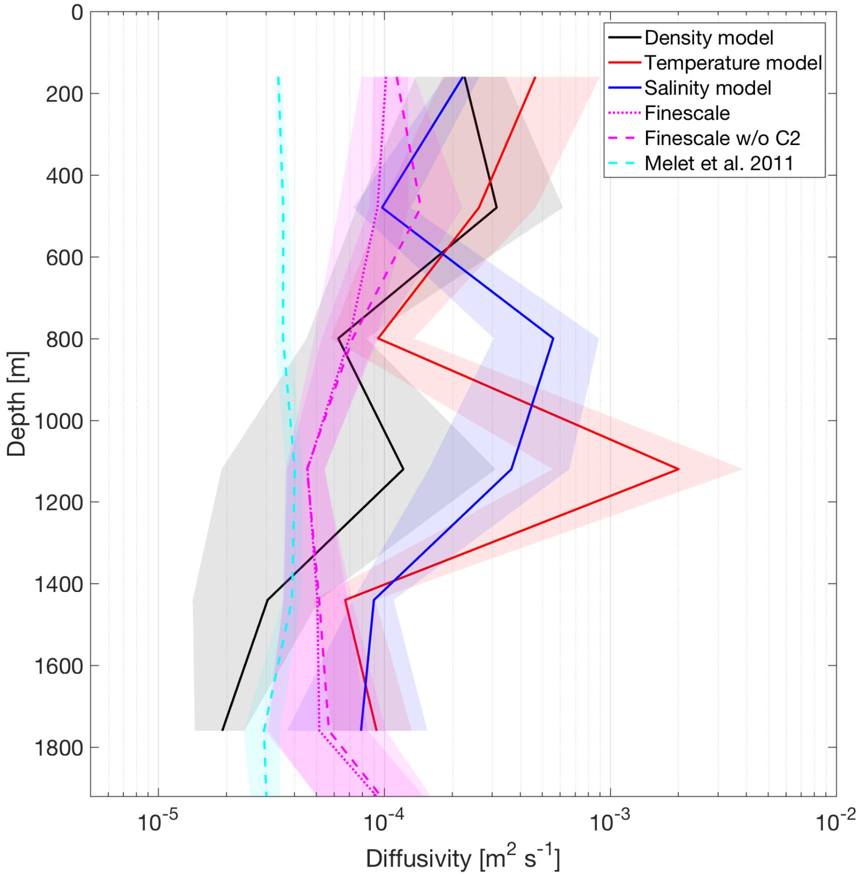

Figure 2.7: Profiles of bin-averaged κ [m^{2}s^{-1}] from the diffusive model using density (black line), temperature (red line), and salinity (blue line) as the tracer. The dotted magenta line shows the profile of bin-averaged observed diffusivity from ship and Argo observations within the water mass pathway between the southern entrance and Vitiaz Strait and the dashed magenta is the same without C2 applied. The dashed cyan line shows the profile for the tide-based parameterization of κ from Melet *et al.* (2011) sampled at the same locations as the finescale observations. The locations of the Argo and shipboard observations used to determine along-path mean κ are shown as magenta dots in Figure 2.1b. Shading around all profiles give the 90% bootstrap confidence intervals for each mean.

& Caulfield, 2003). The resulting mean profiles of κ, using N^2 averaged over the same depth ranges as mean ϵ, are given in Figure 2.4d. Bin-averaged N^2 for shipboard and Argo observations within the Solomon Sea are maximum at the surface and decrease by two orders of magnitude by 2000 m depth with a vertical structure similar to Argo ϵ (not shown). Because the vertical profile of Argo ϵ spans three orders of magnitude compared to the two orders that its mean profile of N^2 spans, Argo κ retains the vertical structure of enhanced mixing at the surface. The smaller span of magnitude for shipboard ϵ leads to local minima in κ near the surface and more uniform vertical structure with depth for finescale κ without C2. The local maximum for density Thorpe scale ϵ at 1200 m (Figure 2.4a, red line) becomes a pronounced subsurface maximum for κ due to the relatively weak stratification at that depth (Figure 2.4d, red line). The large variation of N^2 in the vertical makes the vertical structure of κ particularly sensitive to ϵ in the Solomon Sea.

In an effort to build confidence in the estimated magnitude of ϵ and thus κ, a simple model that approximates the diffusion of tracers is employed to achieve an independent estimate of κ for comparison with observational-based estimates. The diffusive model, $\frac{\partial}{\partial t} = \kappa \frac{\partial^2}{\partial z^2}$, is applied to the tracers temperature, salinity and density. This model ignores the complexity of the system, such as surface heat and buoyancy fluxes, and main purpose is for comparison with the magnitude and depth structure from the observed profiles of κ. Mean profiles of each tracer (10-2000 m depth, 2 m vertical resolution) are estimated from Argo profiles in the Solomon Sea water mass inflow region (13 to 11° S, 153 to 156° E) and outflow region north of Vitiaz Strait (7 to 4° S, 146 to 148° E) (Figure 2.2). Melet *et al.* (2011) find that the majority of transport through Vitiaz Strait originates from this narrow inflow region at the southern entrance to the Solomon Sea. The modeled water mass transit times between the two locations from Melet *et al.* (2011) (their Table 3) are used for the temporal derivative. Profiles of κ that are bin-averaged in depth and their corresponding 90% bootstrap confidence intervals from the diffusive model are shown in Figure 2.7. In addition a mean profile of κ derived from all finescale observations along the water mass pathway between the southern entrance and Vitiaz Strait is shown in Figure 2.7 with the locations of the corresponding observations marked by magenta dots in Figure 2.1b.

The profiles from the diffusive model are generally maximum near the surface at $2.2 - 4.7 \times 10^{-4}$ [$\mathrm{m^2s^{-1}}$] and decrease with depth to $1.9 - 9.2 \times 10^{-5}$ [$\mathrm{m^2s^{-1}}$]. Depth-means of κ from density give the lowest estimate below 600 m while the error bars of κ from density encompass the estimates from temperature and salinity above 600 m. Thus using density as our tracer gives a lower bound to the estimate of κ. Below 600 m depth, mean salinity and temperature-derived κ exceed density-derived κ. This suggests that isopycnal stirring, in addition to diapycnal mixing, may significantly contribute to water mass modification. Melet *et al.* (2011) finds that while $\approx 69 - 83\%$ of the observed water mass modification is diapycnal along this pathway for surface and thermocline waters, diapycnal mixing only accounts for 39% of modification along the intermediate isopycnals.

The mean κ from all finescale strain observations (ship and Argo) within the Vitiaz Strait water mass pathway has a similar magnitude compared to that predicted by the diffusive model but is nearly uniform with depth (Figure 2.7, dotted magenta line). Again when C2 is not applied there is a relative increase in the finescale mean profile above 1000 m depth (Figure 2.7, dashed magenta line). The tide-based parameterization of κ from the simulation by Melet *et al.* (2011) sampled at the locations of the finescale observations has a similar order of magnitude as κ from both the observations and the simple model, particularly below 1000 m depth (Figure 2.7, dashed cyan line). This mean profile only attempts to predict mixing resulting from internal tides and does not include mixing from the turbulent closure model also used in the original simulation. The parameterization additionally has an upper bound of 10^{-4} [$\mathrm{m}^2\mathrm{s}^{-1}$] potentially biasing the modeled κ low. Nonetheless, it is encouraging that the different estimates of κ have similar magnitudes at depth where internal waves likely dominate mixing.

2.5.4 Spatial patterns

The vertical structure of the mean Argo dissipation in the Solomon Sea is very similar to the mean profile of dissipation in the Indo-Pacific over the same latitudinal range, but depth-averages are factor of 2-10 larger in the Solomon Sea (not shown, Whalen *et al.* (2012)). We might expect a relatively large dissipation rate in the Solomon Sea compared to the rest of the equatorial Indo-Pacific due to differences in topography. The Solomon Sea has several topographic features that have been identified as sources of internal waves: Solomon Strait and the two undersea ridges in the Southern half of the basin (Figure 2.1a) (Simmons *et al.*, 2004). Additionally since the Solomon Sea is partially enclosed, internal waves may reflect off the steep walls of the basin, trapping the internal wave energy in the basin and creating a rich field of shear and strain compared to open-ocean conditions.

In the three isopycnal layers investigated here, ϵ spans at least two orders of magnitude making ϵ within the Solomon Sea highly variable along water mass pathways (Figure 2.6). Thus the pathway and residence time of water masses traveling through the Solomon Sea will determine how much water masses are modified. The patterns of dissipation along the intermediate (AAIW) and deep isopycnal layers are well correlated with tide power input and topographic roughness (Figure 2.8b,c), suggesting tidally generated and locally dissipated internal waves are of first order importance for the spatial patterns of mixing along those isopycnals. Patterns of near-bottom ϵ (Figure 2.6d) are consistent with mixing resulting from the tides and rough topography, though coverage is relatively sparse due to the deep bottom depths of the Solomon Sea. Dissipation in the thermocline (STMW) layer does not display such an obvious correlation to either tidal power input or topographic roughness which may be expected if mixing is not dominated by internal tides (Figure 2.8a),though internal waves generated by the barotropic tide are likely still important for mixing in the thermocline. Other processes that generate internal waves and drive mixing that are temporally and spatially variable likely construe these patterns in a mean sense. The mean fields of dissipation for all three isopycnal layers have no clear relationship with wind power input or eddy kinetic energy (not shown). Both wind power input and eddy kinetic energy have large seasonal variability in the Solomon Sea with spatial patterns that change dramatically over the seasonal cycle. Wind power input and eddy kinetic energy likely modulate the strength of mixing in the upper ocean but their effect on ϵ and the potential phase lag between ϵ and these processes requires a well resolved seasonal cycle of the patterns of ϵ in the Solomon Sea.

2.5.5 Seasonal changes

Mean Thorpe scale ϵ from duplicate shipboard stations suggest seasonal variability of dissipation with ϵ enhanced in July and decreased in March (Figure 2.4b, dashed lines). Shipboard and Argo finescale additionally find ϵ to be enhanced in July compared to March, though to a lesser degree. Temporal changes in ϵ are generally related to variability in internal wave generation (Alford, 2003*b*) and/or changes in large scale eddy kinetic energy, current shear, and stratification that can influence and interact with internal wave driven turbulence (Whalen *et al.*, 2012; Moum *et al.*, 2013).

Near-inertial waves are generated when atmospheric winds input energy into

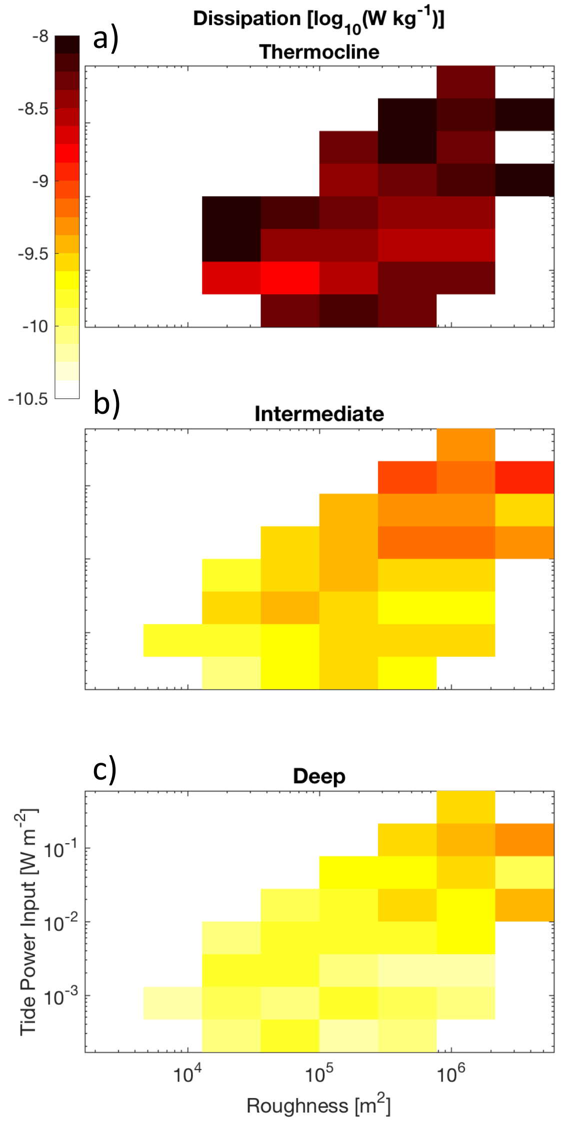

Figure 2.8: The log of median dissipation [W kg^{-1}] over the a) thermocline ($23.3 < \sigma_\theta < 26.7$), b) intermediate ($26.7 < \sigma_\theta < 27.5$), and c) deep ($27.5 < \sigma_\theta$) density layers as a function of topographic roughness [m^2] and tide power input [W m^{-2}]. The colorbar limits are the same for all panels.

the surface mixed layer causing oscillations at the base of the mixed layer at the local inertial frequency which propagate equatorward and are an important part of the internal wavefield. Temporal variability in wind power input is thus responsible for changes in near-inertial wave generation (Alford & Whitmont, 2007). The Solomon Sea monsoonal wind forcing is characterized by strong wind stress in July and weak wind stress in January and may drive a corresponding seasonal cycle in near inertial waves and associated turbulent mixing. A preliminary estimate of the mean annual cycle of power input into the near-inertial wavefield integrated over the study region is computed using the method and data described in Alford (2001,0); Simmons & Alford (2012). Using that data, power input in the present study region is enhanced in July compared to March by a factor of 1.8. The seasonal cycle of wind power input for the region is maximum in July to September and minimum in January to March, consistent with the local monsoonal wind forcing which dominates the seasonal variability of wind stress for the Solomon Sea (Tomczak & Godfrey, 2013). A more comprehensive analysis of the seasonal cycle of internal wave energy from mooring data in our study is now underway.

The monsoonal winds also drive a seasonal cycle in the wind stress curl that results in a seasonally variable eddy kinetic energy field at a three month lag (Hristova & Kessler, 2012; Gourdeau *et al.*, 2014; Hristova *et al.*, 2014; Djath *et al.*, 2014). Whalen *et al.* (2012) find that temporal and spatial variations in ϵ are positively correlated with eddy kinetic energy which they hypothesize has to do with internal wave-eddy interactions that enhance turbulence. Thus we might expect the Solomon Sea eddy kinetic energy to modulate ϵ seasonally as well. In addition satellite, mooring, and shipboard observations find that the NGCC/NGCU system has seasonal variability in strength, direction and structure (Murray *et al.*, 1995; Melet *et al.*, 2010*b*; Germineaud *et al.*, 2016), thus changing the large scale horizontal and vertical shear fields. This may result in seasonal variability of shear instabilities and/or wave-current interactions (Moum *et al.*, 2013). A final temporally variable mechanism that may be of interest is lee wave generation by the NGCC/NGCU system. The currents' shifting pathways, depth and strength will result in the NGCC/NGCU system interacting with shallow and rough topography, particularly in Vitiaz Strait where strong near bottom velocities have been observed (Murray *et al.*, 1995), influencing lee wave generation and strength.

2.6 Final Remarks

Correctly representing the vertical structure, spatial patterns and temporal variability of mixing in the Solomon Sea is key for accurately modeling water mass modification and regional climate (Melet *et al.*, 2016). Koch-Larrouy *et al.* (2010) and Kida & Wijffels (2012) demonstrate that accurately representing tidally driven mixing is important for modeled sea surface temperature, rain and wind in the marginal Indonesian Seas that then directly affect tropical climate via ocean-atmosphere interactions. In the Solomon Sea it appears that tides and topographic roughness are, as expected, appropriate quantities to base a parameterization of mixing upon for deep and intermediate layers. In the thermocline however such quantities are likely insufficient. Temporally and spatially variable parameterizations are likely required to accurately predict thermocline water transformation. Mooring observations and long term Argo observation may help clarify the seasonal cycle and phasing of thermocline mixing relative to local atmospheric forcing, which is the subject of on-going work. Comparing the total parameterized κ from turbulent closure models and internal tide estimates with observed κ remains an open question for understanding and correctly parameterizing upper ocean mixing in the Solomon Sea.

While great strides have been made to understand transport pathways and low frequency variability of mesoscale processes in the Solomon Sea, the region likely contains a host of unresolved small scale processes (beyond freely propagating internal waves) that influence mixing. Vitiaz Strait and St. Georges Channel are both narrow channels with sills at $\sim$ 1000 m depth and strong velocities (¿ 1 ms^{-1}) at the core. With the addition of the barotropic tide, these straits potentially generate hydraulic jumps and/or lee waves, both of which can result in deep turbulent mixing. Numerical and/or observational process studies could investigate the presence and strength of these processes in the Solomon Sea. Mixing in these straits could be important because it occurs within the largest water mass pathways with direct connections to the EUC and the equatorial Indo-Pacific.

Since dissipation varies by up to two orders of magnitude within isopycnal layers, it remains unclear whether strong mixing with short residence times or weaker mixing with longer residence times are more important for water mass modification in the Solomon Sea. Regions of intense mixing (channels, along the southwest boundary, see Figure 2.6) are co-located with strong current velocities implying that while the water masses transported along those pathways undergo vigorous mixing compared to slower pathways in the interior, the water mass is exposed to these turbulent processes for a relatively brief amount of time. Quantifying the relative influence on water mass modification of these different cases (weak mixing with long residence times vs. strong mixing with short residence times) remains an important question for understanding and accurately modeling ocean circulation.

2.A Finescale Parameterization

The finescale parameterization is based on two physical quantities, isopycnal strain, ξ_z, and buoyancy frequency normalized shear, $\frac{\mathbf{U}_z}{\hat{N}}$, where $\mathbf{U}_z = (\frac{\partial u}{\partial z} + i\frac{\partial v}{\partial z})$. The Brunt-Vaisala frequency N [s^{-1}] is calculated using `sw_bfrq`, a routine in the CSIRO

SEAWATER library for MATLAB (Morgan, 1994) and $\hat{N}$ is N smoothed over a window equal to the segment length of the Fourier transform used in subsequent steps and subsampled to vertical resolution of $\mathbf{U}_z$.

Vertical shear and smoothed buoyancy frequency are broken into 320 m, half over-lapping segments starting from the bottom of the cast, with each segment containing $M_{uz} = \frac{320m}{\Delta z_{uz}}$ points, where Δz_{uz} is the vertical resolution of the shear (typically 10 m). The unsmoothed profiles of N^2 at 1 m vertical resolution are divided into 320 m long segments that exactly overlap the segments of $\frac{\mathbf{U}_z}{\hat{N}}$. To calculate isopycnal strain,

$$\xi_z = \frac{N^2 - N^2_{fit}}{\overline{N^2}}, \tag{2.1}$$

the difference is found between the unsmoothed stratification and the cubic fit of N^2, N^2_{fit}, and the quantity is normalized by the segment-averaged stratification, $\overline{N^2}$. Potential errors arise from choosing to use a cubic fit of N^2 rather than the more accurate but computationally expensive adiabatic leveling, with errors being largest in the upper ocean where stratification changes the most rapidly. To quantify the potential error associated with this choice, all 320 m segments from the top 500 m of the water column of N^2 observations and their corresponding N^2_{fit} were used to generate mean profiles of N^2 and N^2_{fit} to determine how well the fits are able to replicate the observed mean field. For these mean profiles, the N^2_{fit} is found to on average overestimate N^2 by only 0.4%. These segments are $M_{\xi_z} = \frac{320m}{\Delta z_{\xi_z}}$ points long.

The parameterization relies on relating the variance of the observed shear and strain fields to that of the theoretical Garrett-Munk (GM) wave field, which has a well-defined wavenumber spectrum that is a function of local stratification and Coriolis.

Thus, the Fourier transform of each segment of $\frac{\mathbf{U}_z}{\hat{N}}$ and ξ_z,

$$\Phi_{uz}(k_z) = \mathcal{F}\left(\frac{\mathbf{U}_z}{\hat{N}} * W_{uz}(k_z)\right), \tag{2.2}$$

$$\Phi_{\xi z}(k_z) = \mathcal{F}\left(\xi_z * W_{\xi z}(k_z)\right), \tag{2.3}$$

which is a function of vertical wavenumber, k_z, is taken after removing a linear fit from each segment and then convolving the physical quantity with a variance preserving window, $W(k_z) = w(k_z)/\sqrt{\frac{\sum w(k_z)^2}{M}}$, where $w(k_z)$ is an M_{uz} or $M_{\xi z}$-point Hanning window, respectively.

The spectra

$$S(k_z) = \frac{\Delta z_{uz}}{2\pi M} 2[\Phi_r^2(k_z) + \Phi_i^2(k_z)]S_{correc}(k_z) \tag{2.4}$$

is formed from the real and imaginary Fourier coefficients, where $\Phi(k_z) = \Phi_r(k_z) + i\Phi_i(k_z)$, normalized by $\frac{\Delta z_{uz}}{2\pi M}$ so that Parseval's theorem is satisfied and corrected for loss of variance due to data processing with $S_{correc}(k_z)$.

The correction term for shear spectra, $S_{uzcorrec}(k_z)$, contains terms that account for variance lost to (c1) range averaging, (c2) finite differencing, (c3) interpolation, and (c4) instrument titling, where $S_{uzcorrec}(k_z) = S_{c1}S_{c2}S_{c3}S_{c4}$. These terms are defined as:

$$S_{c1} = \operatorname{sinc}(\frac{k_z \Delta z_t}{2\pi})^{-2} \operatorname{sinc}(\frac{k_z \Delta z_r}{2\pi})^{-2} \tag{2.5}$$

$$S_{c2} = \operatorname{sinc}(\frac{k_z \Delta z}{2\pi})^{-2} \tag{2.6}$$

$$S_{c3} = \operatorname{sinc}(\frac{k_z \Delta z_r}{2\pi})^{-4} \operatorname{sinc}(\frac{k_z \Delta z}{2\pi})^{-2} \tag{2.7}$$

$$S_{c4} = \operatorname{sinc}(\frac{k_z \bar{d}}{2\pi})^{-2} \tag{2.8}$$

with Δz_t the LADCP transmitted vertical pulse length, Δz_r the LADCP receiver processing bin length, Δz the resolution of the data, and $\bar{d} = 9$ m, determined empirically by Polzin *et al.* (2002). The correction term for strain spectra only needs to account for the loss of variance due to first differencing, $S_{\xi z correc}(k_z) = \text{sinc}(\frac{k_z \Delta z_{\xi_z}}{2\pi})^{-2}$.

The spectral variance, $\langle S \rangle$, is quantified by integrating the spectra over an appropriate vertical wavenumber range. For the shear spectra, the minimum wavenumber, k_{min}, corresponds to the largest resolved wavelength which is equal to the segment length, while the maximum wavenumber corresponds to the smallest wavelength that is distinctive from instrument noise ($\lambda_z = 50$ m) (Polzin *et al.*, 2002). If necessary, k_{max} is adjusted when the spectra is saturated such that $\langle S_{uz} \rangle \leq 0.67$. For strain spectra, k_{min} is set to limit contamination due to stratification with an equivalent wavelength of 150 m and k_{max} has a wavelength of 10 m to avoid instrument noise and is adjusted such that $\langle S_{\xi_z} \rangle \leq 0.22$ (Kunze *et al.*, 2006).

The GM spectrum takes the form,

$$S_{GM} = r_{GM} \frac{\pi}{2} E_0 b j_* \frac{k_z^2}{(k_z + k_z^*)^2}, \tag{2.9}$$

where $r_{GM} = 3$ for the GM shear spectrum and $r_{GM} = 1$ for the strain spectrum, $k_z^* = \pi j_* \bar{N} / b N_0$, b = 1300 m, $j_* = 3$, $E_0 = 6.3 \times 10^{-5}$, $N_0 = 5.24 \times 10^{-3}$ rad s^{-1}, and $\bar{N}$ is the segment-averaged buoyancy frequency. For every segment of shear and strain a corresponding GM spectrum is calculated and integrated over the same wavenumber ranged used for integrating the observed spectra.

The observed and GM variances are used to estimate the ratio of shear to strain variance in the segment,

$$R_\omega = \frac{3 \langle S_{uz} \rangle \langle S_{\xi z GM} \rangle}{\langle S_{\xi z} \rangle \langle S_{uz GM} \rangle}. \tag{2.10}$$

The ratio is also a measure of the aspect ratio of the observed internal wave field. In the the Solomon Sea, we find a mean $R_\omega = 4.2$.

The parameterization uses $\langle S \rangle$ and $\langle S_{GM} \rangle$ from either shear or strain to estimate the turbulent dissipation rate,

$$\epsilon = \epsilon_0 \frac{\bar{N}^2}{N_0^2} h(R_\omega) j(\bar{N}, f) \frac{\langle S \rangle^2}{\langle S_{GM} \rangle^2}, \tag{2.11}$$

with $\epsilon_0 = 6.73 \times 10^{-10}$. Dissipation is adjusted for the local buoyancy frequency $\bar{N}$ and rotation, f, by

$$j(\bar{N}, f) = \frac{f \operatorname{arccosh}(\frac{\bar{N}}{f})}{f_{30} \operatorname{arccosh}(\frac{N_0}{f_{30}})}, \tag{2.12}$$

with $f_{30} = f(30^\circ)$. An additional correction, $h(R_\omega)$, is applied and its form depends on whether the shear or stain variance is used. When using $\langle S_{uZ} \rangle$ to estimate ϵ,

$$h(R_\omega) = \frac{3(R_\omega + 1)}{2\sqrt{2R_\omega(R_\omega - 1)}}, \tag{2.13}$$

and when $\langle S_{\xi z} \rangle$ is used,

$$h(R_\omega) = \frac{R_\omega(R_\omega + 1)}{6\sqrt{2(R_\omega - 1)}}. \tag{2.14}$$

Our analysis uses $\langle S_{uz} \rangle$ and the mean Solomon Sea R_ω to calculate ϵ.

Acknowledgements

The Pandora and MoorSPICE cruises are contributions to the CLIVAR/SPICE and GEOTRACES International programs. The Pandora cruise has been co-funded by ANR (project ANR-09-BLAN-0233-01), INSU/LEFE, IRD, LEGOS, and NSF Grant OCE1029487. The MoorSPICE cruise has been co-funded by NSF Grant OCE1029487, ANR-09-BLAN-0233-01, and INSU/LEFE project Solwara. Pandora and MoorSPICE data can be found at http://www.obs-vlfr.fr/proof/cruises.php. Moor-

SPICE data can also be found through Cruise DOI:10.7284/903044. We are grateful to the crews of the R/V l'Atalante and R/V Thomas G. Thompson. We are also grateful to the engineers and scientists who carefully sampled, recorded, and treated the data. This subset of the Argo database was made freely available by the Coriolis project and programs that contribute to it (http://www.coriolis.eu.org). This publication benefited from the insightful and constructive comments of Robin Robertson and an anonymous reviewer.

Chapter Two, in full, is a reprint as it appears in the Journal of Geophysical Research: Oceans, 2017. Alberty, M. S., Sprintall, J., MacKinnon, J., Ganachaud, A., Cravatte, S., Eldin, G., Germineaud, C. and Melet, A. (2017) Spatial patterns of mixing in the Solomon Sea. *J. Geophys. Res. Oceans*, 122, doi:10.1002/2016JC012666. ©American Geophysical Union. Used with permission. The dissertation author was the primary investigator and author of this paper.

Chapter 3

Moored Observations of Transport in the Solomon Sea

3.1 Abstract

The Solomon Sea is a marginal sea in the western Pacific warm pool that contains the South Pacific low latitude western boundary currents (LLWBCs). These LLWBCs chiefly exit the Solomon Sea through three channels (Vitiaz Strait, St. Georges Channel and Solomon Strait) and serve as the primary source water for the Equatorial Undercurrent (EUC). Simulations have shown that transport partitioning between the straits determines the water mass structure of the EUC, but the relative contributions of transport through each strait have not been observed before. As part of the Southwest Pacific Ocean Circulation and Climate Experiment (SPICE), an array of moorings was deployed simultaneously in the three outflow channels of the Solomon Sea from July 2012 until March 2014 to resolve transport and water properties in each strait. Above deep isopycnals ($\sigma_0 \leq 27.5$), Vitiaz and Solomon Straits account for 54% and 36% of the mean transport, respectively with the remaining 10% exiting through St. George's Channel. The strongest subinertial transport variability

is observed in Solomon Strait and dominates total transport variability. A significant fraction of this variability is at intraseasonal timescales. Finally, a previously unobserved deep current at 1500 m depth is found to enter the Solomon Sea through Solomon Strait, with a deployment mean transport of 4.6 Sv (Sv $\equiv 10^6$ m^3 s^{-1}).

3.2 Introduction

The Solomon Sea contains the low latitude western boundary current (LLWBC) system of the South Pacific, which serves to connect the Equatorial Pacific and South Pacific subtropical circulations (Tsuchiya, 1968; Tsuchiya *et al.*, 1989; Fine *et al.*, 1994; McCreary & Lu, 1994; Johnson & McPhaden, 1999; Grenier *et al.*, 2011,0). The topography of the Solomon Sea restricts the LLWBC to transit through three relatively deep channels: Vitiaz Strait, St George's Channel and Solomon Strait (Figure 3.1). The Solomon Sea LLWBC system supplies approximately two thirds of the Equatorial Undercurrent (EUC) transport that reaches the Central Pacific (Grenier *et al.*, 2011). Modeling studies (Grenier *et al.*, 2011; Qin *et al.*, 2016) show that the waters exiting equatorward through the three straits have distinct pathways to the EUC. Different transit times and mixing are associated with each pathway and influence the upper/lower and northern/southern hemisphere structure of EUC water mass properties.

The relatively cold, nutrient-rich waters of the EUC upwell in the eastern Pacific, supporting globally important primary production with elevated iron concentrations (Pennington *et al.*, 2006; Ryan *et al.*, 2006; Qin *et al.*, 2016). Sources of iron have been identified along the LLWBC pathways that pass through Vitiaz Strait and Solomon Strait and as iron has been suggested to be the limiting nutrient in equatorial Pacific primary productivity, the Solomon Sea has been identified as a region of interest (Mackey *et al.*, 2002; Slemons *et al.*, 2010; Radic *et al.*, 2011; Slemons *et al.*, 2012;

Labatut *et al.*, 2014; Qin *et al.*, 2016). Pathways with short transit times from the Solomon Sea to regions of upwelling in the eastern Pacific, such as through Solomon Strait, are more efficient at transporting iron and driving primary productivity (Qin *et al.*, 2016), but until now, the relative contributions of the total volume transport through each strait have not been simultaneously observed. Direct observations of iron transport have still not been made. However, quantifying the partitioning of volume transport between straits is key for understanding the influence of the different water mass pathways on equatorial primary productivity.

The Solomon Sea is also an important pathway for Antarctic Intermediate Water (AAIW) from the South to North Pacific Ocean (Lindstrom *et al.*, 1990; Tsuchiya, 1991; Qu & Lindstrom, 2002,0). AAIW that transits the Solomon Sea supplies both the North Equatorial Countercurrent (Reid Jr, 1965; Tsuchiya, 1991) and the Mindanao Undercurrent (Qu *et al.*, 1998; Hu *et al.*, 1991; Fine *et al.*, 1994). The LLWBC system additionally delivers South Pacific lower thermocline and deep waters, including AAIW, to the Indian Ocean via the Indonesian Through Flow (Talley & Sprintall, 2005). Two synoptic observations suggest that AAIW transport through St. George's Channel and Solomon Strait combined is comparable to that through Vitiaz Strait but temporal variability is significant over the two seasons leaving the importance of St. George's and Solomon Strait in AAIW transport an open question (Germineaud *et al.*, 2016).

The Climate and Ocean: Variability, Predictability and Change (CLIVAR) Southwest Pacific Ocean Circulation and Climate Experiment (SPICE) international program was designed in part to address the gap in our knowledge of Solomon Sea circulation through numerical modeling and in-situ observations (comprehensive reviews of the project and the ongoing activities are detailed in Ganachaud *et al.* (2014) and specifically for the Solomon Sea in Ganachaud *et al.* (2017)). As part of SPICE, a co-funded, French-US experiment for an 18-month mooring campaign was designed to quantify the total and partition of transport that passes through Vitiaz Strait, St. George's Channel, and Solomon Strait. The study is unprecedented in terms of the vertical resolution and temporal duration of velocity observations made simultaneously in each channel. Additionally, temperature and salinity sensors were deployed to investigate the water mass variability in the thermocline, intermediate and deep layers.

Here we present the first simultaneous observations of transport from all three exit passages of the Solomon Sea acquired under the SPICE program. The contribution of each exit channel in the mean and the temporal variability are quantified over the deployment period. Section 3.3 provides background about the mean and variable current structure and associated water mass characteristics of the Solomon Sea. Section 3.4 details the moored SPICE observations and the procedure for converting the individual observations into a gridded, cross-channel dataset. The mean and time-varying transport and partitioning between channels for each layer is detailed in Section 3.5. Section 3.6 describes the mean and variability of the observed temperature and salinity signatures over the thermocline and intermediate water masses. A summary of the results and investigation into the relationships between layer transport and potential forcing mechanisms is given in Section 3.7. The paper concludes with final remarks in Section 3.8.

3.3 Solomon Sea Currents and Water Masses

3.3.1 Solomon Sea Geography

The Solomon Sea is bordered by the main island of Papua New Guinea to the West, the islands of New Britain and New Ireland to the North and the Solomon

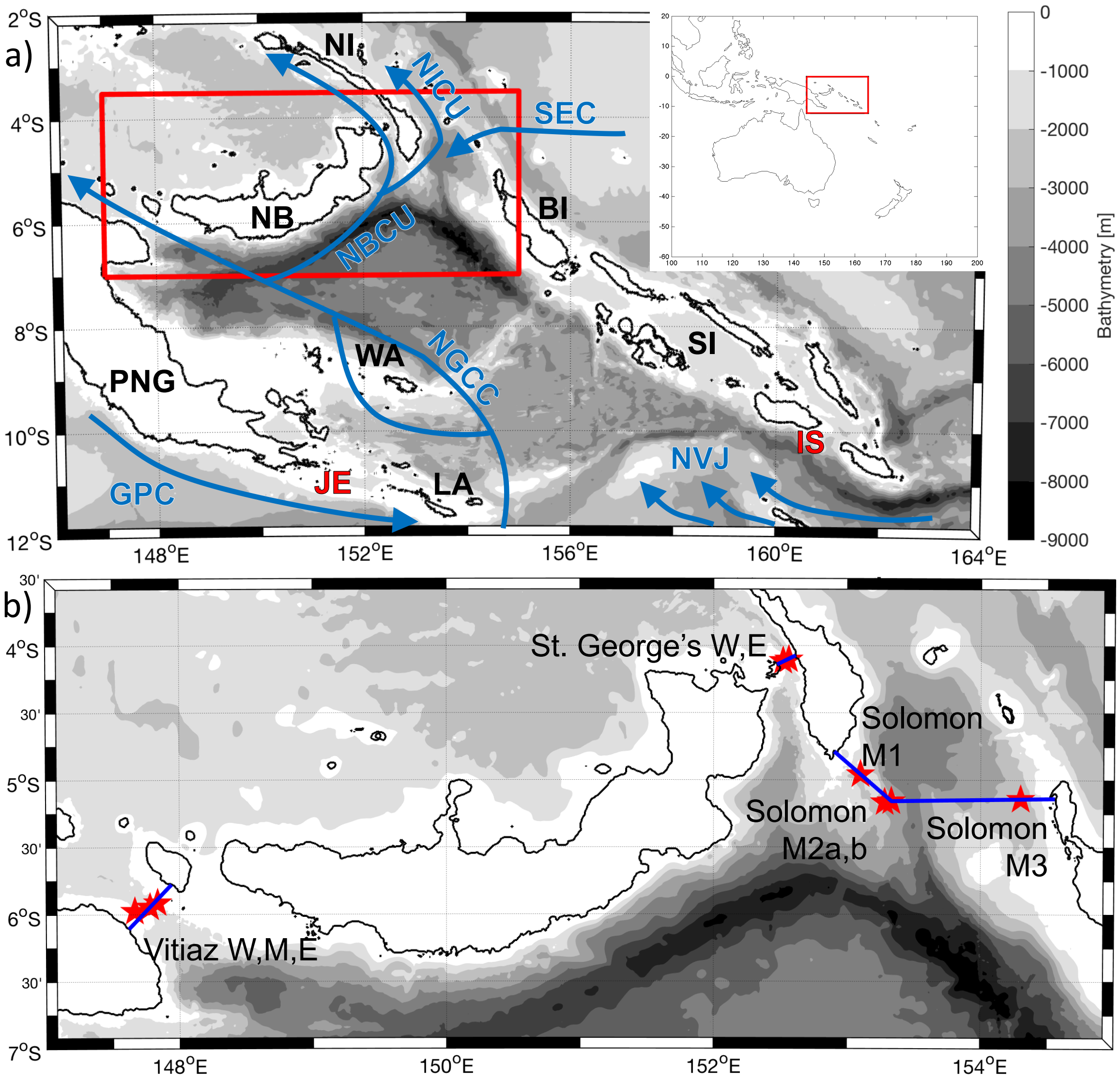

Figure 3.1: (a) Solomon Sea bathymetry and schematic of the major currents within the basin: Gulf of Papua Current (GPC), New Guinea Coastal Current system (NGCC), New Britain Coastal Undercurrent (NBCU), New Ireland Coastal Undercurrent (NICU), North Vanuatu Jet (NVJ), and South Equatorial Current (SEC). The main island of Papua New Guinea (PNG), New Britain (NB), New Ireland (NI), Woodlark Archipelago (WA), Louisiade Archipelago (LA), Bougainville Island (BI), and the Solomon Islands (SI) are noted, as are Jomard Entrance (JE) and Indispensable Strait (IS). The regional location of the Solomon Sea within the Southwest Pacific is shown in the inset map. (b) The locations and names of the SPICE moorings (red stars and text) and the cross-strait transects used to calculate volumetric transport through each channel (blue lines). The map's location within the Solomon Sea is noted by the red box in (a).

Islands chain to the East (Figure 3.1a). The southern border is open to transport from the Coral Sea while flow through the northern border is restricted to Vitiaz Strait (37 km wide at 250 m depth, 1070 m sill depth), St George's Channel (15 km wide at 250 m depth, 1400 m sill depth) and Solomon Strait (185 km wide at 250 m depth, 2525 m sill depth). There are several narrow and shallow gaps between the Solomon Islands along the eastern side of the Solomon Sea, potentially where surface layer transport is exchanged. A single deep channel, Indispensable Strait (50 km wide, 1400 m sill depth), is the only potential location along the eastern boundary where thermocline and deeper waters can be transported into the Solomon Sea. Limited observations suggest the contribution is relatively small compared to inflow through the southern opening (2-3 Sv, $\sim$ 10% of mean transport into Solomon Sea) (Gasparin *et al.*, 2012).

3.3.2 Mean Surface and Thermocline Circulation

From the ocean surface to the base of the thermocline ($\sigma_0 = 26.7$, 350-420 m depth), mean circulation is supplied to the Solomon Sea by the Gulf of Papua Current (GPC, SPICE Community (2012)) from the southwest, the North Vanuatu Jet (NVJ) from the southeast, and the South Equatorial Current (SEC) from the northeast through Solomon Strait (Fine *et al.*, 1994; Hristova & Kessler, 2012; Kessler & Cravatte, 2013) (Figure 3.1a). The GPC enters the Solomon Sea after retroflecting around the Louisiade Archipelago, becoming the New Guinea Coastal Current system (NGCC) (Lindstrom *et al.*, 1987; Sokolov & Rintoul, 2000; Gasparin *et al.*, 2012).

In the Solomon Sea, the NGCC flows equatorward with a local velocity maximum between 200 and 400 m but also extends deep into the water column with velocities $\geq$ 10 cm/s at 700 m depth (Lindstrom *et al.*, 1987; Sokolov & Rintoul, 2000; Davis *et al.*, 2012; Gasparin *et al.*, 2012; Germineaud *et al.*, 2016). As the NGCC approaches Woodlark Archipelago, surface water flows northwestward through the archipelago while thermocline NGCC passes to the east of Woodlark Archipelago (Melet *et al.*, 2010*a*; Cravatte *et al.*, 2011; Melet *et al.*, 2011; Hristova & Kessler, 2012; Germineaud *et al.*, 2016). North of Woodlark, the NGCC re-merges before bifurcating again south of New Britain with one branch flowing northwest and passing through Vitiaz Strait while the remainder flows northeastward along the coast of New Britian (Cravatte *et al.*, 2011). Murray *et al.* (1995) used moored velocity observations to estimate a deployment-mean, full-depth transport through Vitiaz Strait of 15.8 Sv (Sv $\equiv 10^6$ m^3 s^{-1}) and found minimum transport in March 1992 and enhanced transport in August 1992. Additional transport observations at Vitiaz Strait by Butt & Lindstrom (1994) and Cravatte *et al.* (2011) along with other transport observations from the Solomon Sea are summarized in Table 3.1.

The portion of the current that travels eastward from the bifurcation point is referred to as the New Britain Coastal Undercurrent (NBCU, Figure 3.1a). The NBCU was first described in simulations by Melet *et al.* (2010*a*) but was hinted at in observations by Fine *et al.* (1994). The NBCU remains close to the coast of New Britain with a subsurface velocity maximum $\geq$ 40 cm/s between 200-400 m depth and extends to at least 1000 m with velocities $\geq$ 10 cm/s (Cravatte *et al.*, 2011; Germineaud *et al.*, 2016). The NBCU bifurcates south of New Ireland and a portion of the flow exits the Solomon Sea through St. George's Channel while the majority of NBCU transport exits through Solomon Strait. The fraction of the NBCU that exits through Solomon Strait flows northward along the coast of New Ireland as the New Ireland Coastal Undercurrent (NICU) (Cravatte *et al.*, 2011). Mean transport exiting St. George's Channel is observed to be relatively small (1-3 Sv above 300 m) (Butt & Lindstrom, 1994; Cravatte *et al.*, 2011), with modeled transport by Melet *et al.* (2011) suggesting a similarly small mean full-depth transport (2.5 Sv). Synoptic observations by Germineaud *et al.* (2016) find larger transports (4-8 Sv) and suggest significant temporal variability. However, no sustained observations have been made in St. George's Channel and temporal variability of transport has not been resolved.

The North Vanuatu Jet (NVJ) and South Equatorial Current (SEC) are the remaining sources of flow into the Solomon Sea (Figure 3.1a). The NVJ enters the Solomon Sea more broadly across the southern entrance compared to the GPC and merges with the NGCC southeast of Woodlark Archipelago (Melet *et al.*, 2010*a*; Cravatte *et al.*, 2011; Hristova & Kessler, 2012; Gasparin *et al.*, 2012; Davis *et al.*, 2012; Germineaud *et al.*, 2016). The NVJ is relatively shallow, extending down to $\sim$ 500 m depth compared to the GPC which is coherently observed down to 1000 m depth. The SEC, which is relatively shallow ($\sim$ 200 m deep) but extends into the upper thermocline, enters the Solomon Sea through Solomon Strait and travels westward toward Vitiaz Strait, joining the NGCC south of New Britain (Hristova & Kessler, 2012; Cravatte *et al.*, 2011; Germineaud *et al.*, 2016). Additional SEC surface transport is thought to enter the Solomon Sea through the shallow gaps in the Solomon Islands (Hristova & Kessler, 2012). Total transport through Solomon Strait thus depends on the balance between the outflowing NBCU and inflowing SEC. Cravatte *et al.* (2011) estimate a Solomon Strait mean transport of 4.4 Sv out of the Solomon Sea for 20-300 m depth, though estimates by Germineaud *et al.* (2016) suggest NBCU and SEC variability at seasonal timescales is significant with transports of 11 Sv in July/August 2012 and -2 Sv in March 2014 over the top 1000 m depth (Table 3.1). While previous observations have expanded our understanding of the mean current pathways in the Solomon Sea these results are limited because they either don't consider all three straits (Butt & Lindstrom, 1994; Murray *et al.*, 1995), are synoptic estimates (Germineaud *et al.*, 2016), or are limited in vertical extent (Cravatte *et al.*, 2011).

3.3.3 Surface and Thermocline Water Masses

Surface waters ($\sigma_0 \leq 23.3$, ~ 100 m depth) are generally warm and fresh, modified by evaporation and precipitation on seasonal and interannual timescales with maximum precipitation inside the Solomon Sea from May-October (Delcroix *et al.*, 2014). Within the thermocline ($23.3 < \sigma_0 \leq 26.7$, $\sim 100 - 400$ m depth) the NGCC system carries two water masses of South Pacific origin: South Pacific Tropical Water (SPTW) and Subtropical Mode Water (STMW) (Kessler & Cravatte, 2013). SPTW originates from the high-salinity, high-evaporation subduction zone around 20°S, 120°W and is identified by a subsurface salinity maximum (Figure 3.2) while STMW is a denser but less saline water subducted in the north Tasman Sea and north of New Zealand (Tsuchiya, 1981; Tsuchiya *et al.*, 1989; Kessler & Cravatte, 2013; Germineaud *et al.*, 2016). The NVJ transports saltier and less modified SPTW compared to SPTW found in the NGCC, as NGCC SPTW takes a more indirect path from the source region and undergoes comparably more modification before entering the Solomon Sea (Figure 3.2).

3.3.4 Surface and Thermocline Current Variability

The seasonal cycle of the surface circulation in the Solomon Sea is driven by monsoonal wind forcing and the annual migration of the South Pacific convergence zone (SPCZ) (Hristova & Kessler, 2012). During the strong southeasterly trade season (June-November) the NGCC is strengthened due to enhanced NVJ surface transport. During the weak northwesterly trade season (December-May), westward SEC surface transport through Solomon Strait increases and southward transport along the eastern side of the Solomon Sea is enhanced such that surface layer NGCC is slightly reduced. Interannual variability of surface transport in the Solomon Sea is dominated by the draining and recharging of the western Pacific warm pool in response to the El Niño-

Southern Oscillation (ENSO) (Melet *et al.*, 2010*b*; Davis *et al.*, 2012; Hristova & Kessler, 2012).

Equatorward New Guinea Coastal Undercurrent (NGCU) thermocline transports are maximum in August-October when NVJ transport into the Solomon Sea is enhanced due to the annual spin up of the southwestern Pacific subtropical gyre (Kessler & Gourdeau, 2007; Melet *et al.*, 2010*a*). At the same time, the gyre spin up reduces GPC transport into the Solomon Sea. While the GPC is the primary source for the thermocline NGCU, NVJ transport variability determines the seasonal variability of the NGCU thermocline transports. SEC thermocline transport also varies on seasonal timescales due to the annual propagation of off-equatorial Rossby waves (Melet *et al.*, 2010*a*,0). SEC thermocline transport into the Solomon Sea is typically maximum in February-April, when NVJ transports are minimum, leading to a weakening of both the NGCU and NBCU during those months (Melet *et al.*, 2010*a*,0).

Altimetric observations by Melet *et al.* (2010*b*) suggest that transport through Vitiaz Strait is seasonally enhanced in July-September, leading the NGCU seasonal maximum by 1-2 months, which is consistent with modeled transports (Melet *et al.*, 2010*a*). Modeled Vitiaz Strait transport variability is small compared to NGCU and NBCU seasonal variability with the suggestion that most of the NGCU transport variability is balanced by the NBCU (Melet *et al.*, 2010*a*). It should be noted that modeled Solomon Sea circulation is sensitive to the width of Vitiaz Strait in the simulation; increasing the channel width from 42 to 67 km leads to a $\sim 50\%$ increase in Vitiaz Strait transport, drawing off flow that would otherwise have exited through Solomon Strait. Modeled thermocline transport through St. George's Channel is maximum in June-August, leading Vitiaz Strait by one month (Melet *et al.*, 2010*a*). Simulated NBCU transport out of Solomon Strait is strongest in August-November, when SEC transport into the Solomon Sea is at it's seasonal minimum. These results are consistent with the limited observations of Cravatte *et al.* (2011).

Interannual thermocline transport variability in the Solomon Sea is dominated by a response to ENSO forcing (Melet *et al.*, 2010*b*; Davis *et al.*, 2012; Melet *et al.*, 2013). Using altimetry, Melet *et al.* (2010*b*) observed that interannual sea level anomalies within the Solomon Sea are representative of the basin-scale first ENSO mode and that Solomon Sea LLBWC transport anomalies counterbalances changes in the warm water volume of the western Pacific Ocean. The in-situ observations of Davis *et al.* (2012) confirm enhanced equatorward transport during El Niño periods and reduced transport during La Niña, and identify that the majority of this transport variability occurs in the top 250 m in the Solomon Sea interior. Simulations indicate that the circulation response is not symmetric between El Niño and La Niña phases (Melet *et al.*, 2013). During El Niño periods, thermocline transport anomalies are communicated through Solomon Strait rather than Vitiaz Strait due to bathymetric controls while La Niña thermocline anomalies are comparable in the two channels. Simulation by Qin *et al.* (2015) find that the relative contribution of Solomon Strait to EUC transport at 170°W increases during El Niño events and decreases during La Niña events, though the variability of the relative contribution to EUC transport is just as large during neutral ENSO phases as during El Niño/La Niña events. Transport variability and partitioning on ENSO timescales has not been directly observed in any of the Solomon Sea straits at this time.

3.3.5 Mean Intermediate Circulation and Water Masses

Along intermediate isopycnals ($26.7 < \sigma_0 \leq 27.5$, $\sim 400 - 1300$ m depth), water is transported by the NGCU system into the Solomon Sea in a narrow, strong current along the coast of Papua New Guinea (Tsuchiya, 1991; Qu & Lindstrom, 2002;

Melet *et al.*, 2011; Gasparin *et al.*, 2012; Germineaud *et al.*, 2016). Outside of the boundary current region, transport through the southern opening of the Solomon Sea is observed to be weak and variable between synoptic observations (Gasparin *et al.*, 2012; Germineaud *et al.*, 2016). The NGCU system carries two distinct intermediate water masses: Subantarctic Mode Water (SAMW) and Antarctic Intermediate Water (AAIW). SAMW is formed by wintertime deep convection in the Southern Ocean and is characterized by high oxygen, which is important for ventilating the lower thermocline (McCartney, 1977; Sokolov & Rintoul, 2000; Germineaud *et al.*, 2016). AAIW, which is denser and lies below SAMW, is formed in the Antarctic convergence zone and is characterized by a local salinity minimum (Reid Jr, 1965; Reid, 1997; Talley, 1999). Both intermediate water masses are characterized by high oxygen (159-184 μmol/kg), low silca (5-34 μmol/L), and low nitrate (13-30 μmol/L) concentrations (Germineaud *et al.*, 2016).

Hydrographic observations indicate that the NGCU transports intermediate waters equatorward through Vitiaz Strait, supplying the North Pacific with intermediate waters up to 15°N (Tsuchiya, 1981; Qu & Lindstrom, 2004; Germineaud *et al.*, 2016). Simulations by Melet *et al.* (2011) suggest that half of Solomon Sea intermediate water mass transport passes through Vitiaz Strait and that nearly all of Vitiaz Strait intermediate water transport comes from the southern opening of the Solomon Sea via the NGCU. The model also indicates that less than 10% of the mean intermediate transport passes through St. George's Channel and approximately 40% exits through Solomon Strait. Hydrographic surveys find that the magnitude of intermediate water mass transport through St. George's Channel and Solomon Strait combined is comparable to that through Vitiaz Strait, however there is a significant difference in transport magnitude observed between the two time periods (Germineaud *et al.*, 2016).

Recent work by Germineaud *et al.* (2016) also demonstrates that the high oxygen and low nutrient signatures of SAMW and AAIW are transported by the NBCU to St. George's Channel and the western boundary of Solomon Strait. Equatorial Pacific Intermediate Water (EqPIW), characterized by low oxygen and high nutrients, was also observed north and east of Solomon Strait outside of the Solomon Sea during both the July-August 2012 and March 2014 cruises. In July-August 2012, EqPIW characteristics are observed across the Eastern side of Solomon Strait along isopycnals generally associated with SAMW ($26 < \sigma_0 \leq 26.9$) and inflow is observed over the same isopycnals from shipboard velocity observations suggesting a temporally variable source of intermediate water into the Solomon Sea through Solomon Strait. Simulations of mean intermediate transport by Melet *et al.* (2011) indicate that one third of intermediate water is transported via the NBCU through Solomon Strait while the majority is due to recirculation of intermediate waters that entered through the Eastern side of Solomon Strait before circulating within the Solomon Sea and passing through Solomon Strait again.

3.3.6 Intermediate Current Variability

Observations by Murray *et al.* (1995) were the first to demonstrate variability of the NGCU down to 800 m depth within Vitiaz Strait, with decreased intermediate transports in March 1992 and enhanced intermediate transports in August 1992. Seasonal variability at intermediate depths (700-800 m) of the NGCU system equatorward of Vitiaz Strait (2.5°S, 142°E) has also been observed by Kawabe *et al.* (2008) with strong, northwestward velocities of 14 cm/s in May-July and weak and even reserving current velocities in November-February. Interannual variability of the NGCU at intermediate depths was also observed by Kawabe *et al.* (2008) which they suggest was related to the 1988-99 La Niña. Intermediate transport estimates

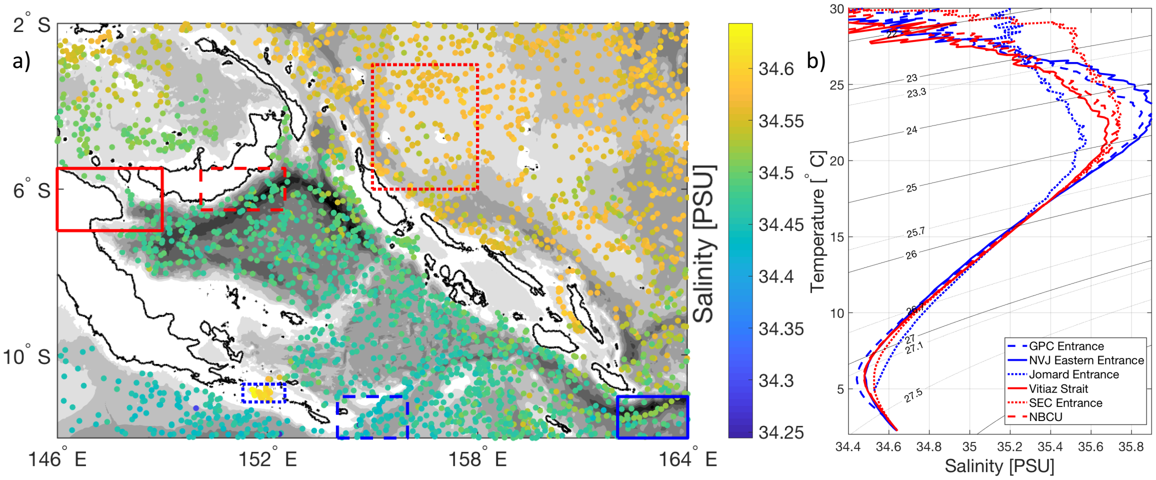

Figure 3.2: a) Map of the Solomon Sea identifying geographic regions of interest for Temperature-Salinity (T-S) relationships: the GPC entrance region (dashed blue line), NVJ Eastern entrance region (solid blue line), Jomard Entrance (dotted blue line), Vitiaz Strait outflow (solid red line), NBCU region (dashed red line), and SEC entrance region (dotted red line). Colored dots show the salinity observed by individual Argo profiles along the $\sigma_0 = 27.1$ isopycnal. b) Mean T-S relationships from Argo profiles averaged along isopycnal surfaces within each geographic region of interest (line style of each T-S profile matches line style of the corresponding box in a)).

by Germineaud *et al.* (2016) from July/August 2012 are a factor of 2 larger than those observed in March 2014 through the southern opening, Vitiaz Strait, and the combination of St. George's Channel and Solomon Strait, further indicating important temporal variability of intermediate transports in the Solomon Sea. While water properties and synoptic surveys have illuminated the pathways of intermediate water masses through the Solomon Sea, the full depth (400-1300 m) intermediate total transport, partitioning, and temporal variability has not previously been observed.

3.4 The SPICE Mooring Dataset

3.4.1 Mooring Deployment, Recovery, and Resulting Dataset

Nine subsurface moorings were deployed during the Pandora Cruise from 4 July to 1 August 2012 on the *R/V l'Atalante* and recovered during the MoorSPICE

Table 3.1: Comparison of previously reported mean Solomon Sea observed transport [Sv] and mean transport from the mooring observations made during the SPICE field program (July 2012 - March 2014) calculated over the same depth ranges as the referenced observation. Positive values indicate equatorward transport out of the Solomon Sea. The associated uncertainties given for SPICE estimates reflect the uncertainty associated with the various interpolation and extrapolation schemes. See references for uncertainties associated with previously published values.

Reference	Time Period	Reference's Transport [Sv]	SPICE Transport [Sv]	Depth Range [m]
Vitiaz Strait				
Butt & Lindstrom (1994)	May 1988	6.1 ± 0.3	6.6 ± 1.8	40-320 m
Murray *et al.* (1995)	1992-1993	14.9-19.0	12.4 ± 3.3	0 m-bottom
Cravatte *et al.* (2011)	1985-2007	7-8	6.5 ± 1.8	20-300 m
Germineaud *et al.* (2016)	Jul/Aug 2012	19.4 ± 0.4	18.7 ± 5.0^a	0-1000 m
	Mar 2014	10.9 ± 0.4	5.3 ± 1.5^a	0-1000 m
St. George's Channel				
Butt & Lindstrom (1994)	May 1988	3.1 ± 0.2	1.6 ± 0.2	40-300 m
Cravatte *et al.* (2011)	1985-2007	1-2	1.6 ± 0.3	20-300 m
Solomon Strait				
Cravatte *et al.* (2011)	1985-2007	4-5	4.5 ± 0.5	20-300 m
St. George's Channel & Solomon Strait				
Germineaud *et al.* (2016)	Jul/Aug 2012	18.8 ± 2.3	24.6 ± 2.1^a	0-1000 m
	Mar 2014	2.2 ± 2.3	11.7 ± 0.9^a	0-1000 m
Total Solomon Sea Transport				
Sokolov & Rintoul (2000)	Jun/Jul 1993	26^b	18.2 ± 3.6	0 m-bottom
Davis *et al.* (2012)	2007-2010	15-20	23.9 ± 3.3	0-700 m
Gasparin *et al.* (2012)	Aug 2007	29 ± 5	23.7 ± 3.5	0-1300 m
Zilberman *et al.* (2013)	2004-2011	18.7 ± 1.4	25.0 ± 3.5	0-1000 m
Germineaud *et al.* (2016)	Jul/Aug 2012	36.2 ± 2.6	43.2 ± 5.4^a	0-1000 m
	Mar 2014	10.7 ± 2.6	11.5 ± 1.6^a	0-1000 m

[a] Estimates only use mooring observations that are concurrent with reference time period.

[b] Only accounts for transport associated with the NGCC system.

Cruise from 28 February to 31 March 2014 on the *R/V Thomas G. Thompson* (Figure 3.1b). The location, depth, and deployment period for each mooring is given in Table 3.2, in addition to the sill depth and channel width at 250 m depth for each channel. Locations and bottom depths are based on triangulation of the acoustic releases after the deployment during the Pandora cruise and were confirmed prior to recovery during MoorSPICE.

Multiple moorings were deployed in each channel to resolve the vertical and cross-strait temperature, salinity and velocity structure and also for redundancy to ensure the likelihood of success of the experiment in the event of mooring failures. Moorings were typically equipped with an upward- and downward-looking Acoustic Doppler Current Profiler (ADCP) to resolve velocity in the upper part of the water column with additional single point current meters installed deeper along the line (Figures 3.3, 3.4, & 3.5, black dots indicate mean location of observations). This vertical resolution of sustained velocity observations is unprecedented for the Solomon Sea. Sensors measuring temperature, conductivity (which allows the estimation of salinity), and pressures were also deployed along the length of each mooring. The mooring pair in the center of Solomon Strait was the single exception, as M2a was the primary mooring with an upward looking ADCP and temperature, conductivity, and pressure sensors along the line and M2b was a redundant mooring measuring velocity and temperature from 50-1700 m depth. All sensors were programed to resolve the tides with sampling rates varying from every minute for some temperature sensors to every 2 hours for the deep current meters. A detailed description of the instrument settings and configuration along each mooring is given in Alberty *et al.* (2017).

Three moorings (Vitiaz West, Middle and East) were deployed across Vitiaz Strait with Vitiaz Middle deployed near the strait's sill in 1130 m of water (Figure 3.1b). Two moorings (St. George's East and West) were deployed in St. George's

Channel near the channel's sill. Four moorings (Solomon M1, M2a, M2b and M3) were deployed across Solomon Strait with M1 deployed near the coast of New Ireland, M2a/M2b near the previously observed core of the NICU (Cravatte *et al.*, 2011), and M3 near Bougainville Island. The mooring configuration at Solomon Strait was designed to both directly observe the velocity and estimate geostrophic transport using the observed temperature, salinity, and pressure from all three moorings.

Over the deployment period, the five moorings deployed in highly dynamic Vitiaz Strait and St. George's Channel sustained structural damage to varying degrees. While the cause of damage for each mooring is ultimately unknown, all five moorings displayed evidence of intense vibrations due to strong mean and tidal currents. Vitiaz Strait is also a highly trafficked channel due to both shipping and fishing. Both floats housing the upward and downward ADCPs for Vitiaz West and East were lost, leaving only the deep, single-point current meters for those moorings. Vitiaz Middle sustained the loss of it's topmost float reducing the vertical coverage of temperature and salinity but leaving ADCP velocity coverage unaffected. In St. George's Channel both moorings sustained the loss of the topmost floats but retained their upward- and downward-looking ADCPs, thus only reducing vertical coverage of temperature and salinity. All nine moorings were also subjected to significant blow-over due to tidal and low-frequency currents.

At Solomon M2a, three Conductivity-Temperature-Depth (CTD) sensors at 300, 550, and 1700 m failed at different times during the deployment period. The record for the deepest sensor at 1700 m was estimated from temperature observations at 1700 m on Solomon M2b, using the tight relationship between temperature and salinity for this depth. A detailed description of this estimation procedure is given in Appendix 3.A.1. The CTDs at 300 and 550 m failed in October and April 2013, respectively, degrading the quality of the geostrophic transport estimate after April

2013. Nonetheless, the geostrophic transport estimate from the time period before the CTD failure is used to verify transport estimated by interpolating the in-situ velocity across Solomon Strait. A description of the geostrophic transport estimate and comparison with transport estimated from the direct observations of velocity is also given in Appendix 3.A.2 & 3.A.3.

After recovery, all data is quality controlled to treat for sensor drift, clock drift, and spurious values. Velocity observations are corrected for compass errors, converted from magnetic to earth coordinates taking magnetic declination into account, and unrealistic spikes and low quality ADCP velocity observations are removed. The full procedure is described in detail in Alberty *et al.* (2017). Quality controlled data for each mooring was then filtered and interpolated onto a common, hourly time base.

Gridded 30 arc-second bathymetry and source identification datasets from both the General Bathymetric Charts of the Ocean (GEBCO) 2014 and Smith & Sandwell (1997) version 11 were investigated to determine the cross sectional bathymetry and along-channel direction for the three straits. The along strait direction for Vitiaz Strait (310°) is determined from a linear regression of the channel bathymetry near the mooring. The cross-section for Vitiaz Strait is defined to be a line normal to the along strait direction and passing through the location of Vitiaz Middle mooring (Figure 3.1b). The along strait direction for St. George's Channel (334°) is defined as the direction normal to the cross-section that passes through both St. George's West and East moorings. The along strait directions for the moorings in Solomon Strait are defined to be the directions normal to the transects between adjacent moorings; 41° for the cross-section connecting M1 and M2 (Solomon Strait West) and 0° for M2 and M3 (Solomon Strait East). Cross sectional bathymetry was interpolated onto each transect at 1 km resolution for Vitiaz and Solomon Straits and at 0.5 km for the narrower St. George's Channel. The bathymetric product used for each channel de-

Table 3.2: Mooring deployment information including the sill depth for each strait, the width of each strait at 250 m depth, and each mooring's location, depth, and deployment period based on the dates of the individual moorings' deployment and recovery in UTC.

Strait	Mooring	Location	Depth [m]	Deployment Period
Vitiaz Strait	West	147°39.96'E 5°58.69'S	980	28/7/2012 - 14/3/2014
Sill: 1070 m, Width: 37km	Middle	147°46.68'E 5°56.64'S	1130	28/7/2012 - 15/3/2014
	East	147°50.05'E 5°54.96'S	900	28/7/2012 - 13/3/2014
St. George's Channel	West	152°31.12'E 4°06.82'S	1243	20/7/2012 - 7/3/2014
Sill: 1400 m, Width: 15km	East	152°33.86'E 4°06.17'S	1433	20/7/2012 - 8/3/2014
Solomon Strait	M1 (West)	153°06.02'E 4°57.48'S	2050	21/7/2012 - 6/3/2014
Sill: 2525 m, Width: 185km	M2a (Middle)	153°16.86'E 5°09.85'S	2559	16/7/2012 - 6/3/2014
	M2b (Middle)	153°19.94'E 5°09.45'S	2710	15/7/2012 - 6/3/2014
	M3 (East)	154°17.98'E 5°08.28'S	2627	18/7/2012 - 4/3/2014

pended on which product had a greater number of grid points based on in-situ depth soundings along the mooring cross-section. GEBCO 2014 bathymetry was used for Vitiaz Strait and St. George's Channel while Smith & Sandwell (1997) version 11 was used for Solomon Strait. Earth coordinate velocities (u, v) are rotated onto the local along strait direction to calculate along strait velocities (ASV). Positive ASV indicates flow that is exiting the Solomon Sea while negative values indicate flow entering.

3.4.2 Vertical Interpolation and Extrapolation

Direct velocity observations are linearly interpolated onto a regular, vertical grid with 20 m spacing starting at 10 m depth. The strong and persistent currents imparted significant drag on the moorings, causing them to blow over and the top of the water column was often not resolved by the individual moorings. In Vitiaz Strait and St. George's Channel, on average the top 55 m and 100 m of the water column, respectively, were beyond the range of the upward looking ADCPs due to this persistent draw down (Figure 3.4, black dots). Mooring draw down was strongest during May-July in Vitiaz Strait and during April-July in St. George's Channel. Near surface coverage of directly observed velocities varied across Solomon Strait with, on average, the top 70 m unresolved at Solomon M1 near the NICU core but only the top 25 and 5 m unresolved at Solomon moorings M2 and M3 where the flow was weaker (Figure 3.3a-c, black dots). Mooring draw down was strongest in September-December for Solomon M1.

Three models were tested to estimate the unresolved near-surface velocities at each time step:

1. **Slab to Surface:** The value of the shallowest observed velocity is assigned to all unresolved depths above that observation (Figure 3.3a and Figure 3.4a & c).

2. **Constant Shear:** Velocities are linearly extrapolated to the surface using the shallowest observed shear and velocity (Figure 3.3b and Figure 3.4b & d).

3. **Satellite Inferred:** The in-situ velocity profile is assumed to be the sum of the geostrophic velocity (u_g, v_g) and the surface Ekman velocity,

$$u = u_g + \frac{\sqrt{2}}{fd} e^{z/d} [\widetilde{\tau}^x \cos(z/d - \pi/4) - \widetilde{\tau}^y \sin(z/d - \pi/4)] \tag{3.1}$$

$$v = v_g + \frac{\sqrt{2}}{fd} e^{z/d} [\widetilde{\tau}^x \sin(z/d - \pi/4) + \widetilde{\tau}^y \cos(z/d - \pi/4)]. \tag{3.2}$$

   The surface Ekman portion of the velocity is estimated at the mooring location where f is the local Coriolis frequency and $d \equiv \sqrt{2A/|f|}$ is the surface Ekman layer thickness which depends on the turbulent viscosity in the surface layer, A. The turbulent viscosity was estimated using the empirical relationship derived by Santiago-Mandujano & Firing (1990) and is a function of wind speed. The Cross-Calibrated Multi-Platform (CCMP) surface vector winds (6-hour and 1/4° resolution, Atlas *et al.* (2011); Wentz *et al.* (2015)) were interpolated onto the mooring's time and location and used to estimate A and the kinematic wind stress, $\widetilde{\tau} \equiv \tau/\rho_0$, where the reference density, $\rho_0 = 1019$ kg/m^3, was estimated using the mean surface density from shipboard CTD profiles (Germineaud *et al.*, 2016; Ganachaud *et al.*, 2017).

The estimated surface Ekman velocities are removed from the directly observed velocity profile. Absolute geostrophic surface velocities estimated from the SSALTO/DUACS Delayed-Time Level-4 sea surface height product (daily and $1/4°$ resolution) are interpolated onto the mooring's time and location. A linear interpolation is then applied from the mooring's shallowest velocity observation to the interpolated absolute geostrophic surface velocity. The estimated surface Ekman profile is then added back to the geostrophic profile (Figure 3.3c).

The surface models were chosen to reflect the variety of near surface velocity structure resolved in prior synoptic observations or to take advantage of concurrent satellite observations. As the Slab to Surface and Constant Shear models do not require independent observations, these methods are applied to all moored velocity records. The Satellite Inferred surface model is only applicable where satellite-based surface products accurately capture both surface winds and sea level variability. Thus the satellite inferred method in only applied to moorings in Solomon Strait where the strait is wide and moorings are located 30 km or farther from the coast to limit the effect of coastal contamination of the altimeter observations. Nonetheless, unquantified uncertainties likely still are contained in the satellite-based surface geostrophic velocities.

Vertical gaps in velocity observations are also present between the deepest observation and the channel bottom or sill depth. Near bottom coverage is best in Vitiaz Strait where the deepest velocity observations are on average within 20 m of the sill depth. In St. George's Channel, on average, 450 m of the water column above the sill depth was not resolved. The deepest velocity observations in Solomon Strait were at a mean depth of 1700 m for all three moorings, 825 m above the sill depth.

Two simple models are tested to estimate the unresolved velocities between the deepest observation and the bottom or sill depth:

1. **Slab to Bottom:** The value of the deepest observed velocity is assigned to all unresolved depths below that observation above the bottom or sill depth, whichever is shallowest.

2. **Linear to Bottom:** Velocities are linearly interpolated from the deepest observation to zero velocity at the bottom or sill depth, whichever is shallowest.

For either bottom model, the velocity in the grid space nearest the bottom or at the sill depth is always set to zero, assuming a no slip boundary. The combination of these models resulted in multiple gridded datasets for each mooring.

Velocities with inertial and super-inertial frequencies (periods $<$ 7 days) are responsible for $16 - 53\%$ of the observed velocity variance at the different moorings. Variance at tidal harmonics, in particular, account for one third to one half of the observed super-inertial variance. Variability at these frequencies is generally the result of the barotropic tide and internal wave field. While a significant portion of kinetic energy at each mooring is contained in the inertial and super-inertial frequencies, the processes responsible for these velocity variations are beyond the scope of this paper. Thus for our purposes of estimating large-scale transports, all mooring ASV time series are low-pass filtered to only contain the sub-inertial frequencies (periods longer than 7 days).

3.4.3 Cross-Passage Interpolation and Extrapolation Schemes

Lateral interpolation of ASV between moorings and extrapolation of ASV to the sidewalls was carried out using three schemes:

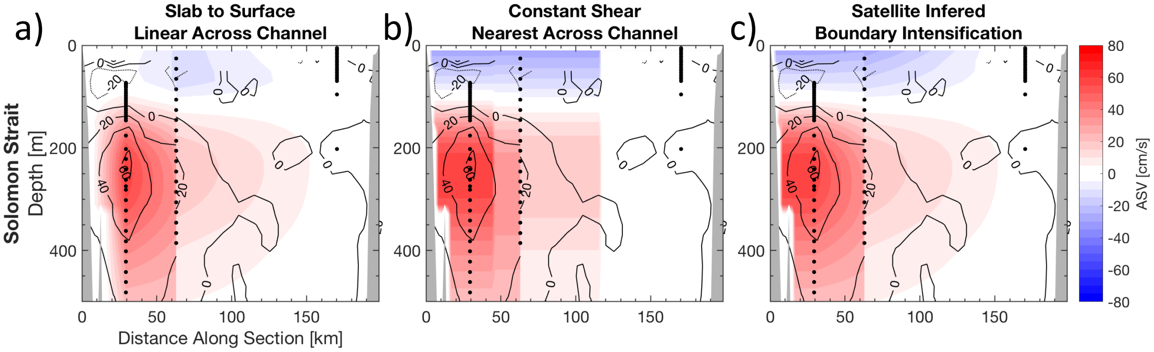

Figure 3.3: Example mean ASV [cm/s] cross sections from mooring observations using the (a) Slab to Surface and Linear Across Channel, (b) Constant Shear and Nearest Across Channel, or (c) Satellite Inferred and Boundary Intensification extrapolation models for the top 500 m of Solomon Strait. Mean shipboard ADCP ASV sections are contoured at 20 cm/s intervals in black on all panels (solid lines are positive, dotted are negative). The deployment-mean locations of all moored ADCP bins and single point current meters are indicated with black dots. Note the discontinuity across Solomon Strait is due to the discontinuous transect line used for the channel (Figure 3.1b).

1. **Linear Across Chanel:** ASV is linearly interpolated between moorings and to zero at the sidewalls for each depth (Figure 3.3a).

2. **Nearest Across Channel:** ASV is uniformly assigned across each depth in the channel by the nearest mooring observation (Figure 3.3b and Figure 3.4a & c).

3. **Boundary Intensification:** In Solomon Strait and Vitiaz Strait, the observed ASV at the westernmost mooring is assigned across each depth from that mooring to the western boundary (Figure 3.3c and Figure 3.4b). In St. George's Channel, the observed ASV at the easternmost mooring is assigned across each depth from that mooring to the eastern boundary (Figure 3.4d). ASV is linearly interpolated between moorings and to zero for the remaining sidewalls.

The cross-channel interpolation schemes were chosen to approximate the different cross-channel velocity sections resolved in prior synoptic observations. For

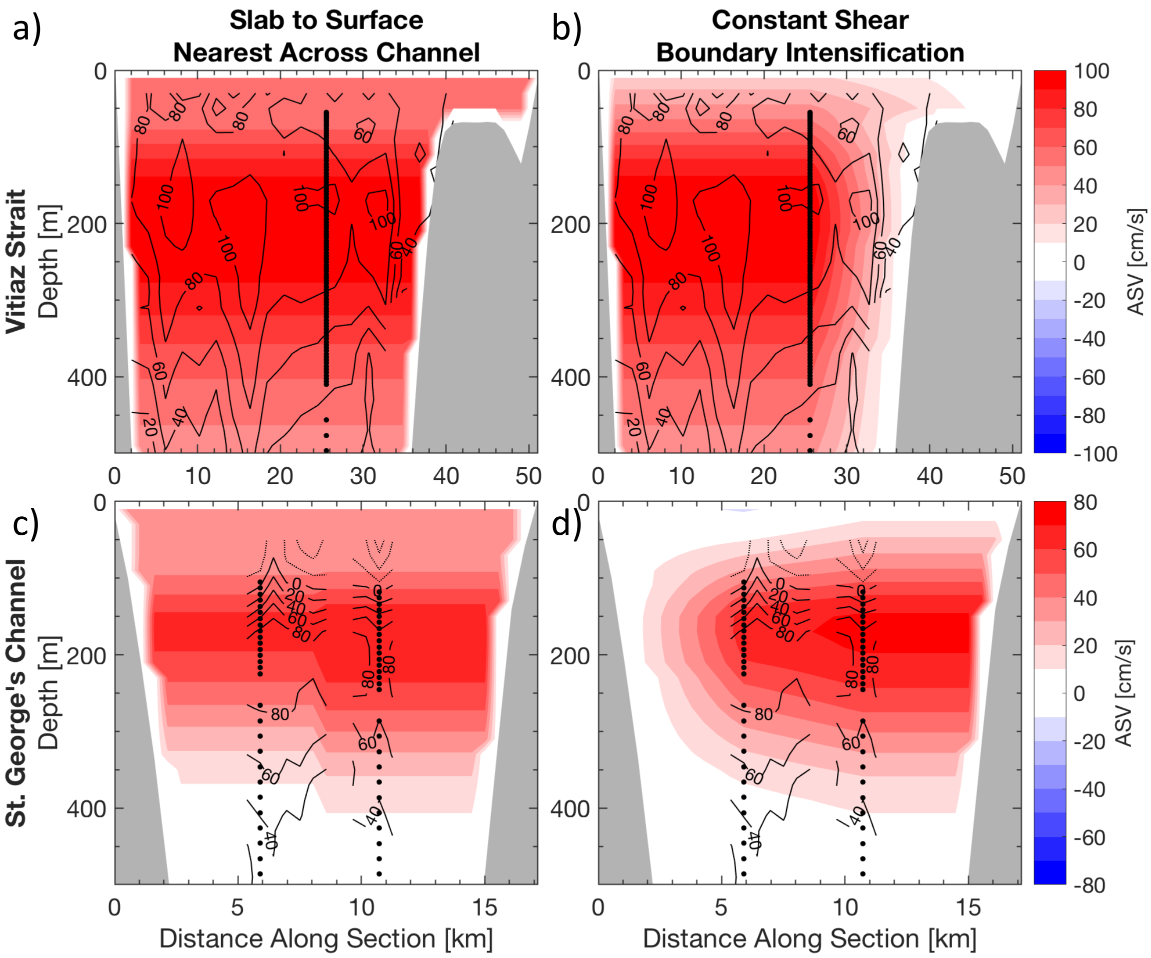

Figure 3.4: Example mean ASV [cm/s] cross sections from mooring observations using the (left) Slab to Surface and Nearest Across Channel, (right) Constant Shear and Boundary Intensification extrapolation models for the top 500 m of (a-b) Vitiaz Strait and (c-d) St. George's Channel. Mean shipboard ADCP ASV sections are contoured at 20 cm/s intervals in black on all panels (solid lines are positive, dotted are negative). The deployment-mean locations of all moored ADCP bins are indicated with black dots.

Table 3.3: Summary of deployment mean transport ± the error due to interpolations choices (and mean standard deviation) [Sv] in Vitiaz Strait, St. George's Channel, Solomon Strait, and the sum of all three channels.

Vertical Bounds	Vitiaz Strait	St. George's Channel	Solomon Strait	Total
$\sigma_0 < 26.7$	8.3 ± 2.3 (2.2)	1.8 ± 0.3 (1.3)	6.4 ± 0.7 (4.9)	16.6 ± 2.4 (5.6)
$26.7 \leq \sigma_0 < 27.5$	4.0 ± 1.1 (2.1)	0.4 ± 0.0 (1.8)	1.8 ± 0.2 (5.3)	6.2 ± 1.1 (6.0)
$27.5 \leq \sigma_0$	n/a	n/a	-4.6 ± 1.0 (5.5)	-4.6 ± 1.0 (5.5)

all models, ASV in the bins nearest the sidewall boundary are set to zero, assuming a no-slip boundary condition. The lateral griding is done with 1 km spacing for Vitiaz Strait and Solomon Strait and with 0.5 km spacing for the narrower St. George's Channel. Due to the mooring configuration across Solomon Strait, ASV is laterally interpolated over two cross-sections: Solomon Strait West from New Ireland to Solomon M2 and Solomon Strait East from Solomon M2 to Bougainville Island (Figure 3.1b).

3.4.4 Transport and Sensitivity

Transport [Sv] is estimated by integrating the gridded cross section of ASV over the cross-channel area. To investigate the vertical distribution of transport, the gridded cross-sections of ASV are integrated across the cross-sectional width at each depth and reported as transport per unit depth [Sv/km]. For all transport estimates, positive values indicate transport that is out of the Solomon Sea through the strait and negative values indicate transport into the Solomon Sea.

Due to the different interpolation and extrapolation choices, multiple transport time series were generated for each channel: 12 each for Vitiaz Strait and St. George's Channel and 18 for Solomon Strait. Mean transports are given as the average of the array of mean transports from the permutations of the different models. The transport error is the standard deviation of the mean due to the range of transport estimates from the different models. A summary of the deployment mean transport, error, and mean standard deviation for all three channels over different vertical limits is given in Table 3.3. The sensitivity of total transport to each interpolation choice is given as the average percent change in deployment-mean transport as a result of using choice A rather than choice B. Percent change is calculated for pairs of time series where all extrapolation choices are identical except for the choice of interest. The percent change from all the pairs are averaged to give the sensitivity of transport in each channel to the different extrapolation choices. Table 3.4 summarizes the transport sensitivity due to all the interpolation and extrapolation choices for this experiment.

An in-depth discussion comparing the different interpolation and extrapolation schemes with prior observations and investigating the sensitivity of transport estimates is given in Appendix 3.A.4 & 3.A.5. The following is a summary of that discussion. For Vitiaz Strait and St. George's Channel, transport estimates are sensitive to the cross-channel extrapolation model and relatively insensitive to vertical extrapolation choices (Table 3.4). In Vitiaz Strait, the Slab to Surface and Linear to Bottom schemes reproduce observed ASV patterns, while the Linear to Surface and Linear to Bottom provide reasonable estimates in St. George's Channel (Figure 3.4). Mean shipboard ADCP sections and prior observations indicate that the Boundary Intensification scheme is an appropriate choice for both channels.

Transport in Solomon Strait however is sensitive to nearly all interpolation choices and methods (Table 3.4). Independent observations indicate that the Constant Shear or Satellite Inferred surface models best approximate near surface ASV in Solomon Strait (Figure 3.3). The Satellite Inferred surface extrapolation is preferred as it is the most physically based model. While total transport in Solomon Strait is sensitive to the bottom scheme, there are no published observations of ASV below 1000 m in the channel. The Linear to Bottom scheme is chosen as it gives conservative estimates of deep transport through Solomon Strait. Prior observations and

Table 3.4: Total transport sensitivity due to different interpolation and extrapolation schemes represented as the average percent change in mean total transport when using the first scheme listed rather than the second.

Extrapolation Scheme	Vitiaz Strait	St. George's Channel	Solomon Strait
Constant Shear vs. Slab to Surface	-3.7%	-9.6%	-36.6%
Constant Shear vs. Satellite Inferred	n/a	n/a	-0.9%
Linear to Bottom vs. Slab to Bottom	0.0%	-0.6%	43.2%
Linear vs. Nearest Across Channel	-94.0%	-42.4%	-41.6%
Linear Across Channel vs. Boundary Intensification	-63.5%	-24.2%	-55.5%

simulations indicate that the Boundary Intensification scheme is the most representative choice for cross-channel interpolation in Solomon Strait (Figure 3.3). The above choices are used to visualize the mean and temporal variability of each channel's transport in the remaining figures of this paper.

Finally, flow in Solomon Strait is observed to have a Rossby number less than one and should be well approximated by geostrophy. However instrument failures in the latter half of the record degrade the quality of the geostrophic transport estimate, particularly in the thermocline. Transport estimated from in-situ velocity observations is in good agreement with the geostrophic estimate before instrument failure and is utilized to estimate transport through Solomon Strait for the remainder of this manuscript (Appendix 3.A.3).

3.5 Results: Transports and Partitioning

3.5.1 Mean Transport and Partitioning

During the SPICE mooring deployment (July 2012 to March 2014) over half (54.2%) of the total transport above the base of AAIW ($\sigma_0 = 27.5$, ~ 1400 m depth) exits the Solomon Sea through Vitiaz Strait. Vitiaz Strait has a mean transport of 12.4 ± 3.3 Sv and flow is relatively steady in time with an average standard deviation of 3.8 Sv. Deployment mean transport through Vitiaz Strait is slightly less than previous synoptic observations when integrated over the same vertical limits (Table 3.1, Butt & Lindstrom (1994); Germineaud *et al.* (2016)), though not significantly different when compared to historical means (Murray *et al.*, 1995; Cravatte *et al.*, 2011). Mean ASV is out of the Solomon Sea at all depths (Figure 3.6a, solid red line and Figure 3.5a). Assuming a Slab to Surface scheme, it increases from 50cm/s at the surface to 100 cm/s at 200m, then decreases to the sill, where it still flows at 8 cm/s. This is consistent with the findings of Cravatte *et al.* (2011), and with Murray *et al.* (1995), who also reported ASV of 10-20 cm/s below 800 m depth.

St. George's Channel supplies a smaller fraction of the total transport for $\sigma_0 < 27.5$ (9.6%) with a mean transport of 2.2 ± 0.3 Sv and an average standard deviation of 2.9 Sv. Mooring transport estimates are in agreement with previous mean transport estimates (Cravatte *et al.*, 2011) and prior synoptic observations fall within the observed temporal variability (Table 3.1, Butt & Lindstrom (1994)). Assuming Constant Shear to the surface, mean surface currents are estimated to be near zero above the eastern mooring and -12 cm/s over the western mooring (Figure 3.5b). Mean transport per unit depth in St. George's Channel has a subsurface maximum of 8 Sv/km at 170 m depth associated with the NBCU and a mean ASV of 73 cm/s at St. George's East (Figures 3.6a, dotted red line and & 3.5b). The deployment mean ASV decreases to less than 5 cm/s below 400 m depth resulting in mean transport per unit depth of less than 1 Sv/km from 400 m to the sill depth. On average, ASV's observed at St. George's East are 5 cm/s stronger than those observed at St. George's West. Mean ASV in the NBCU is 20 cm/s stronger in the mooring observations compared to the mean SADCP sections of Cravatte *et al.* (2011). No prior observations have resolved ASV below 400 m within St George's Channel.

The remaining 36.2% of transport above the $\sigma_0 = 27.5$ isopycnal exits through Solomon Strait (8.3 ± 0.9 Sv). Solomon Strait has the largest temporal variability with a standard deviation of 8.6 Sv. Previous estimates of transport in Solomon Strait are in good agreement with the directly observed ASV estimate (Table 3.1, Cravatte *et al.* (2011)). Using the Satellite Inferred surface model, transport in the top 100 m enters the Solomon Sea with 29.0 Sv/km of transport per unit depth at the surface (Figure 3.6a, blue lines). Both sides of Solomon Strait contribute nearly equally to the surface transport but surface velocities are stronger on the western side of Solomon Strait with mean ASV of -28 cm/s at the surface above Solomon M1 and -26 cm/s above Solomon M2 (Figure 3.5c). Surface ASV are weaker on the eastern side but the larger cross-section width results in comparable transport to the western side.

From 100-850 m depth, transport exits the Solomon Sea across Solomon Strait. Subsurface transport is maximum at 250 m depth for both the western and eastern sides with mean transports per unit depth of 28 Sv/km and 12 Sv/km, respectively (Figure 3.6a, blue lines). This subsurface maximum in transport is associated with the outflowing NICU which has a mean ASV of 58 cm/s on the western side of the strait at Solomon M1 (Figure 3.5c).

While the sill depth of both Vitiaz Strait (1070 m) and St. George's Channel (1400 m) are shallower than or nearly equal to the depth of the $\sigma_0 = 27.5$ isopycnal, Solomon Strait has a deeper sill depth of 2525 m. At Solomon Strait, a transport of -4.6 ± 1.0 Sv with a standard deviation of 5.5 Sv is observed *entering* the Solomon Sea between the $\sigma_0 = 27.5$ isopycnal and sill depth. A weak and broad inflow below 850 m is observed across all three moorings with the strongest mean ASV of 8 cm/s observed at Solomon M2. These are the first direct observations of this deep current.

The structure of mean ASV across Solomon Strait is in reasonable agreement with simulated circulation by Djath *et al.* (2014), including the persistent, deep inflow below 850 m depth. Simulations by Melet *et al.* (2010*a*) predict a weak thermocline level inflow at 200 m depth on the eastern side of Solomon Strait. Periodic inflows at thermocline depth are observed on the eastern boundary of Solomon Strait by mooring M3, as is indicated by the elevated standard deviation of ASV from the surface to 350 m depth. However, a mean inflow predicted by simulations at that location is not resolved or confirmed by these mooring observations (Figure 3.5c & d).

The mean total transport for all three exit straits combined from the surface to the base of AAIW, $\sigma_0 = 27.5$, is 22.8 ± 3.5 Sv equatorward, out of the Solomon Sea with an average standard deviation of 9.9 Sv due to temporal variability. The Solomon Sea mooring deployment-mean total transport is 2-4 Sv larger than previous estimates of mean transport from the inflow region by Davis *et al.* (2012) and Zilberman *et al.* (2013) when integrated over the same depth ranges (Table 3.1). However, the Argo network in the Solomon Sea was relatively sparse with during the study period of Zilberman *et al.* (2013) and did not resolve transport close to the western boundary. Zilberman *et al.* (2013) also observe interannual transport anomalies of ±4 Sv from 2004-2011 and Davis *et al.* (2012) note transport variability of ±15 Sv due to seasonal-interannual variability over a 3 year period.

On average, there is net transport of 11 Sv into the Solomon Sea above 50 m depth which is primarily supplied by surface transport through Solomon Strait and partially balanced by Vitiaz Strait surface transport (Figure 3.6a). From 50-950 m depth, total transport is equatorward and out of the Solomon Sea with maximum transport of 75 Sv/km depth around 220 m depth. While subsurface transport maxima from all three channels contribute to the total transport, Solomon Strait contributes the largest fraction of mean thermocline transport with a slightly smaller contribution by Vitiaz Strait. Below the thermocline to 950 m depth, Vitiaz Strait and Solomon Strait West carry nearly equal fractions of mean intermediate trans-

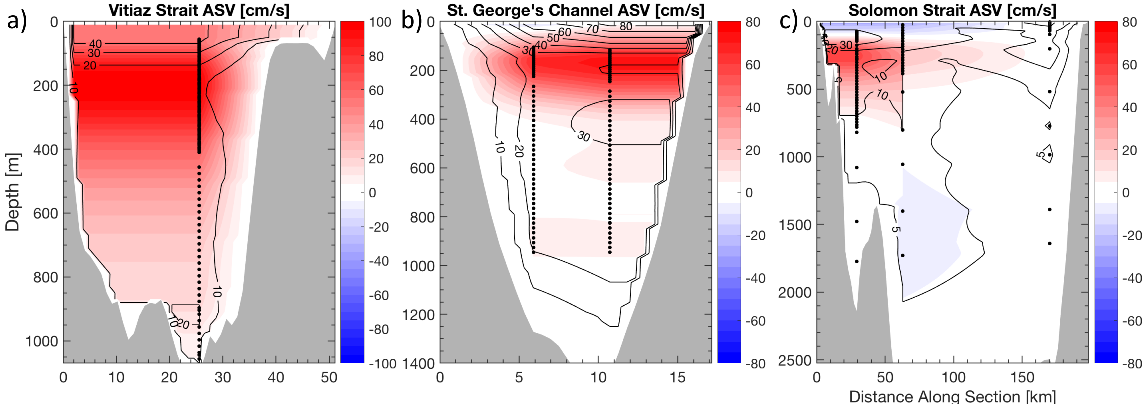

Figure 3.5: The mean (red-blue colormap) and standard deviation (black contours) of the ASV [cm/s] for (a) Vitiaz Strait, (b) St. George's Channel, and (c) Solomon Strait. Statistics were calculated over the deployment period and the vertical limits are the ocean surface to each channel's respective sill depth. Mean ASV sections are contoured at 5 cm/s increments and red indicates transport exiting the Solomon Sea while blue indicates transport entering. The standard deviation of the along strait velocity is contoured in 10 cm/s intervals with an additional 5 cm/s contour for Solomon Strait. Deployment-mean locations of all ADCP bins and single point current meters are indicated with black dots for the directly observed velocity sections. Note the discontinuity across Solomon Strait is due to the discontinuous transect line used for the channel cross-section (Figure 3.1b).

port. Mean total transport reverses again below 950 m with weak flow down to 2525 m depth that is into the Solomon Sea, entirely contributed by Solomon Strait East. South and upstream of the straits, Davis *et al.* (2012) and Zilberman *et al.* (2013) find mean profiles of transport per unit depth with similar vertical structure and subsurface maxima of $\sim$ 50 Sv/km at 250 m.

3.5.2 Time Varying Transports

Vitiaz Strait full depth transport ranges from 2.3-21.5 Sv over the deployment period (Figure 3.6b, solid red line). To tease apart the variance associated with seasonal and intraseasonal timescales, transport time series are low-pass filtered with a half year cut off to estimate transport variability at seasonal timescales (Figure 3.7a). The lowpass filtered seasonal estimate is removed from the unfiltered transport

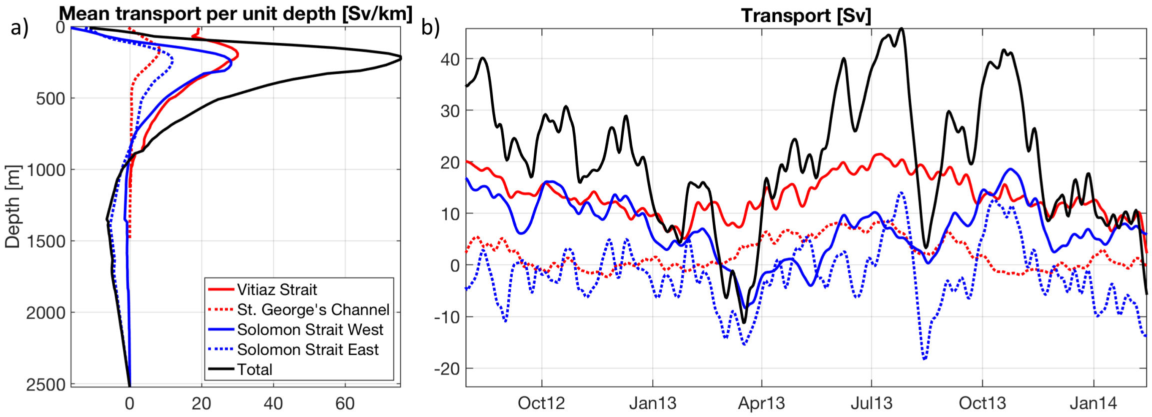

Figure 3.6: a) Mean profiles of subinertial transport per unit depth [Sv/km] and b) the surface to sill depth subinertial transport time series [Sv] for Vitiaz Strait (solid red line), St. George's Channel (dotted red line), Solomon Strait West (solid blue line), Solomon Strait East (dotted blue line), and the total of the three straits (solid black line).

to estimate the intraseasonal part of the transport signal (Figure 3.7b). In Vitiaz Strait, the lowpass filtered transport remains positive over the deployment period with a mean of 12.4 Sv and is relatively steady in time with a standard deviation of 2.3 Sv (Figure 3.7a, solid red line). Lowpass filtered transport is enhanced in July and August, consistent with the seasonal maximum observed by in altimetry by Melet *et al.* (2010*b*) and in SADCP observations by Cravatte *et al.* (2011). Transport variability is larger at seasonal timescales with nearly twice as much variance in the lowpass filtered transport compared to the intraseasonal transport for Vitiaz Strait (Figure 3.7b, solid red line).

Significant ASV variability is found over the entire water column in Vitiaz Strait with ASV standard deviations > 10 cm/s with enhanced variability in the top 100 m and just above the sill depth (Figure 3.5a). Transport in the top 100 m weakens and reverses from January through April, with maximum surface transport out of the Solomon Sea from June through September (Figure 3.8a). Mooring draw down is minimal from November through March, with ADCP coverage up to 50 m depth and resolving reversals down to 100 m depth in February, March, and November

2013 and in January 2014. Enhanced surface transports in August through October 2012 and in June through August 2013 have large uncertainties due to mooring draw down during those times. The observed seasonal variability of the surface layer in Vitiaz Strait is in agreement with surface drifter (Hristova & Kessler, 2012) and SADCP observations (Lindstrom *et al.*, 1990; Cravatte *et al.*, 2011), though no prior observations have resolved sustained reversals of transport in the top 100 m.

The NGCU core, located between 100-300 m depth, persists over the deployment period but weakens and strengthens in phase with the surface transport (Figures 3.8a), consistent with prior simulations (Melet *et al.*, 2010*a*). Below the thermocline, seasonal weakening and reversals in December 2012 and January 2013 lead surface reversals by 1-2 months and intermediate transport is enhanced in June-July 2013. While previous observations by Murray *et al.* (1995) note similar seasonal variability of intermediate transport, deep reversals have not been previously observed in Vitiaz Strait. The relative phasing of transport variability over the water column is most clear in the transport per unit depth anomaly (Figure 3.9a), which is the transport per unit depth time series (Figure 3.8) with the mean profile of transport per unit depth removed (Figure 3.6a). Negative and positive transport anomalies appear to propagate upwards from intermediate depths toward the surface in October 2012 and April 2013, with intermediate anomalies leading thermocline and surface anomalies by 2-3 months.

Full depth transport through St. George's Channel varies from 2.3 Sv entering the Solomon Sea to 8.4 Sv exiting through St. George's Channel (Figure 3.6b, dotted red line). Lowpass filtered transport remains positive over the deployment period with a mean of 2.3 Sv and standard deviation of 1.8 Sv (Figure 3.7a, dotted ref line). Intraseasonal transport in St. George's Channel has 30% less variance than the lowpass filtered signal resulting in a transport time series that varies on seasonal timescales but has intermittent periods of negative transport in October-January (Figures 3.6b, dotted red line). Intraseasonal and seasonal transport variance in St. George's Channel is comparable to that in Vitiaz Strait.

Strong ASV variability is found in St. George's Channel with standard deviations of ASV $>$ 20 cm/s over all observed depths at both moorings (Figure 3.5b). Transport above 100 m depth enters the Solomon Sea from October through February and is estimated to exit the Solomon Sea in April through August (Figure 3.8b). Mooring draw down is minimal October through February with ADCP observations extending up to 50 m during those months. ADCP coverage is reduced in March to September with significant losses of coverage in June and July 2013 resulting in greater uncertainty of surface transport estimates during these periods. SADCP observations suggest that negative transports over the top 100 m may continue into March-May but that surface transports become positive and relatively enhanced in June-August (Cravatte *et al.*, 2016).

In St. George's Channel, the NBCU persists throughout the deployment period, transporting water out of the Solomon Sea over 100-300 m depth (Figure 3.8b). Thermocline transport is reduced October through February (Figure 3.9b), in phase with surface transport reduction, and enhanced April through August, consistent with previous simulations of thermocline transport through St. George's Channel (Melet *et al.*, 2010*a*; Djath *et al.*, 2014). Below the NBCU core, transport reverses seasonally and nearly in phase with the observed surface reversals, exchanging water masses with the Bismark Sea between 400 m on a seasonal timescale. Periods of outflow are stronger and extend deeper into the water column compared to periods of transport into the Solomon Sea, resulting in a net outflow below 400 m depth on seasonal timescales. Reversal of intermediate currents through St. George's Channel on seasonal timescales has not been previously observed and prior modeling studies of circulation through the strait have not noted this feature in their results (Djath *et al.*, 2014; Coulin *et al.*, 2017). Transport anomalies are nearly in phase over the entire water column in St. George's Channel (Figure 3.9b).

Full depth transport through Solomon Strait has the largest temporal variability of the three channels with transport varying from -23.7 to 30.0 Sv over the deployment period (Figure 3.6b, blue lines). Transport at Solomon Strait West is typically positive and varies at seasonal time scales (Figure 3.7b, solid blue line). Transport across Solomon Strait East fluctuates around zero, has large variability and contributes significantly to the range of total transport over the deployment period (Figure 3.7b, dotted blue line).

Lowpass filtered total transport for Solomon Strait West is enhanced and positive in August through October and is minimum in April with a mean transport of 6.8 Sv and standard deviation of 3.6 Sv (Figure 3.7a, solid blue line). For Solomon Strait East, lowpass filtered transport is generally negative with a mean of -2.1 Sv and has relatively little variability with a standard deviation of 1.7 Sv (Figure 3.7a, dotted blue line). Lowpass filtered variability at Solomon Strait East leads that at Solomon Strait West by 1 month. In Solomon Strait, intraseasonal transport variability is the largest of the three channels, particularly on the eastern side of Solomon Strait (Figure 3.7b, blue lines). Lowpass filtered and intraseasonal transport have the equivalent variance for Solomon Strait West, while intraseasonal transport at Solomon Strait East has 10 times as much variance as the lowpass filtered transport for that section, contributing the majority of the total intraseasonal transport variability.

While transport variability is larger on the eastern side of Solomon Strait because of it's larger cross-sectional area, ASV variability is stronger across the western side with standard deviations $>$ 10 cm/s above 700 m depth at Solomon M1 and M2 due to NICU and SEC variability (Figure 3.5c). The largest variability for direct ASV is observed at 100-200 m depth, between the mean SEC inflow and NICU outflow east of New Ireland (Figure 3.5c). Across Solomon Strait West, NICU transport is strong and extends up toward the surface in August through October 2012 (Figure 3.8c). By December 2012, SEC inflow is observed, deepening and strengthening into April and May 2013 while the NICU weakens and its vertical extent decreases. In May 2013, the NICU begins to strengthen and extend upward again while the SEC weakens and shallows until December 2013 when a moderate increase in SEC transport is observed again. This interplay between the vertical extents and strength of the SEC and NICU leads to the observed subsurface maximum in ASV standard deviation east of New Ireland (Figure 3.5c).

Observed thermocline transport anomalies across Solomon Strait West are consistent with simulations by Melet *et al.* (2010*a*) and Djath *et al.* (2014) which also find the NICU to be enhanced in July-September and reduced in March-April (Figure 3.9c). Three inflow events between 800-1200 m depth are observed in Solomon Strait West in September 2012 and March and August 2013 when the lower extent of the NICU is reduced and approaches the $\sigma_0 = 26.7$ isopycnal (Figure 3.8c).

On the eastern side of Solomon Strait, ASV variability in the top 200 m is larger at Solomon M3 compared to M2 and ASV standard deviations of 20 cm/s are resolved near the surface at Solomon M3 (Figure 3.5c). Significant intraseasonal transport variability is observed over all depths at Solomon Strait East (Figure 3.8d). The surface inflow across Solomon Strait East is the combination of persistent, negative surface ASV near Solomon M2 and weak but intraseasonally variable surface velocities at Solomon M3 (Figure 3.5c). Transport per unit depth below the thermocline ($\sigma_0 = 26.7$) at Solomon Strait East is punctuated by large anomalies that span intermediate and deep density classes and sometimes extend into the thermocline as well, specifically in March and August 2013 (Figure 3.9c). Deep transport ($\sigma_0 > 27.5$)

generally enters the Solomon Sea across Solomon Strait East along the deep western boundary, although three outflow events are observed in May, August and October 2013 (Figure 3.8d). Djath *et al.* (2014) finds that this deep inflow varies seasonally, reaching a maximum in December-February and weakening in June-August. Deep transport is observed to be consistently negative in December to February but significant variability is also resolved at intraseasonal timescales even at these depths (Figure 3.8d).

Top to bottom total transport from the three channels ranges from -11.2 to 45.9 Sv over the deployment period (Figure 3.6b, solid black line). Lowpass filtered total transport is maximum in July-August and minimum in February, with the largest contribution coming from Vitiaz Strait (Figure 3.7a). Intraseasonal total transport has twice as much variance compared to lowpass filtered total transport and Solomon Strait East is responsible for the majority of intraseasonal total transport variability (Figure 3.7b). From the surface to 100 m depth, Solomon Strait SEC inflow provides the dominant contribution for both the mean and variability of the total surface transport (Figure 3.8e). Total thermocline transport varies seasonally with Vitiaz Strait and Solomon Strait West contributing comparably. Intermediate transports through Vitiaz Strait and St. George's Channel are nearly in phase with each other and out of phase and counterbalanced by intermediate transport through Solomon Strait West (Figure 3.8, note the different colorbar scales). The resulting total intermediate transport is thus well described by intermediate transport through Solomon Strait East, which is also the largest observed intermediate transport across the three channels. Solomon Strait East is the sole contributor of deep transport and transport variability.

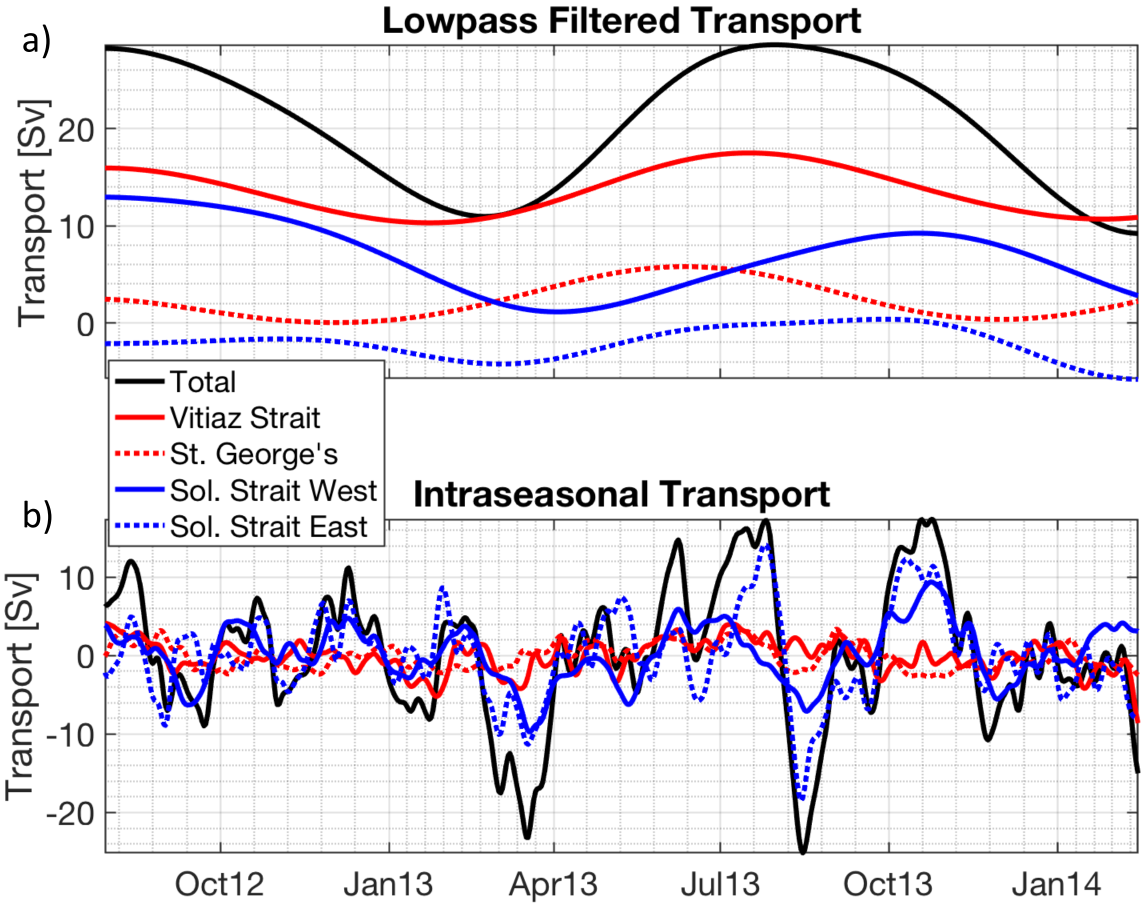

Figure 3.7: (a) Lowpass filtered and (b) intraseasonal surface to sill depth transport [Sv] for Vitiaz Strait (solid red line), St. George's Channel (dotted red line), Solomon Strait West (solid blue line), Solomon Strait East (dotted blue line), and the total of the three straits (solid black line).

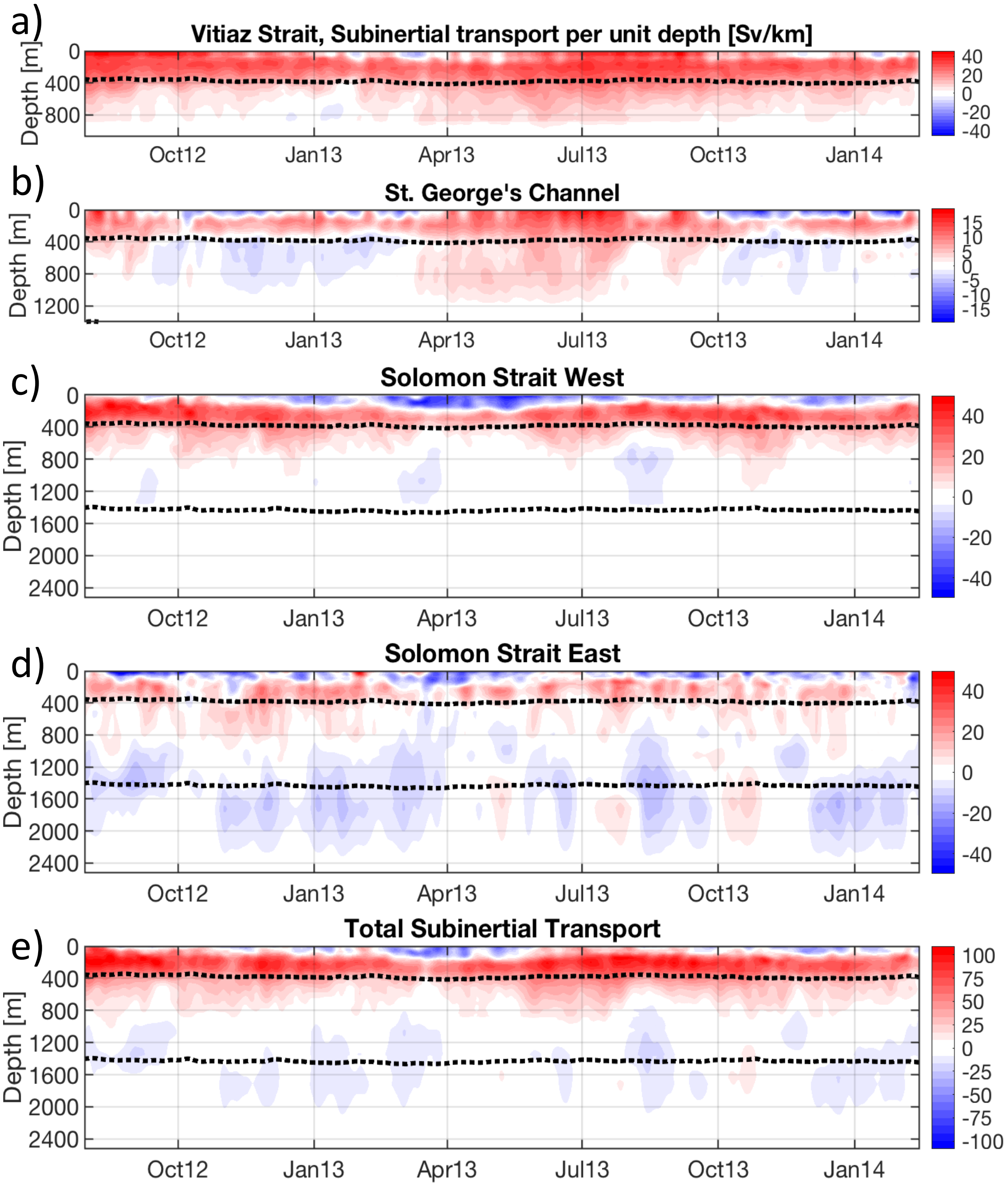

Figure 3.8: The subinertial transport per unit depth [Sv/km] for a) Vitiaz Strait, b) St. George's Channel, c) Solomon Strait West from New Ireland to Solomon M2, d) Solomon Strait East from Solomon M2 to the coast of Bougainville Island, and e) the total transport of from all three channels. Positive values (red) indicate transport exiting the Solomon Sea while negative values (blue) indicate transport entering the Solomon Sea. The dotted black lines indicate the depth of the $\sigma_0 = 26.7$ and $\sigma_0 = 27.5$ isopycnals. Note the different scales of the colorbars for each panel.

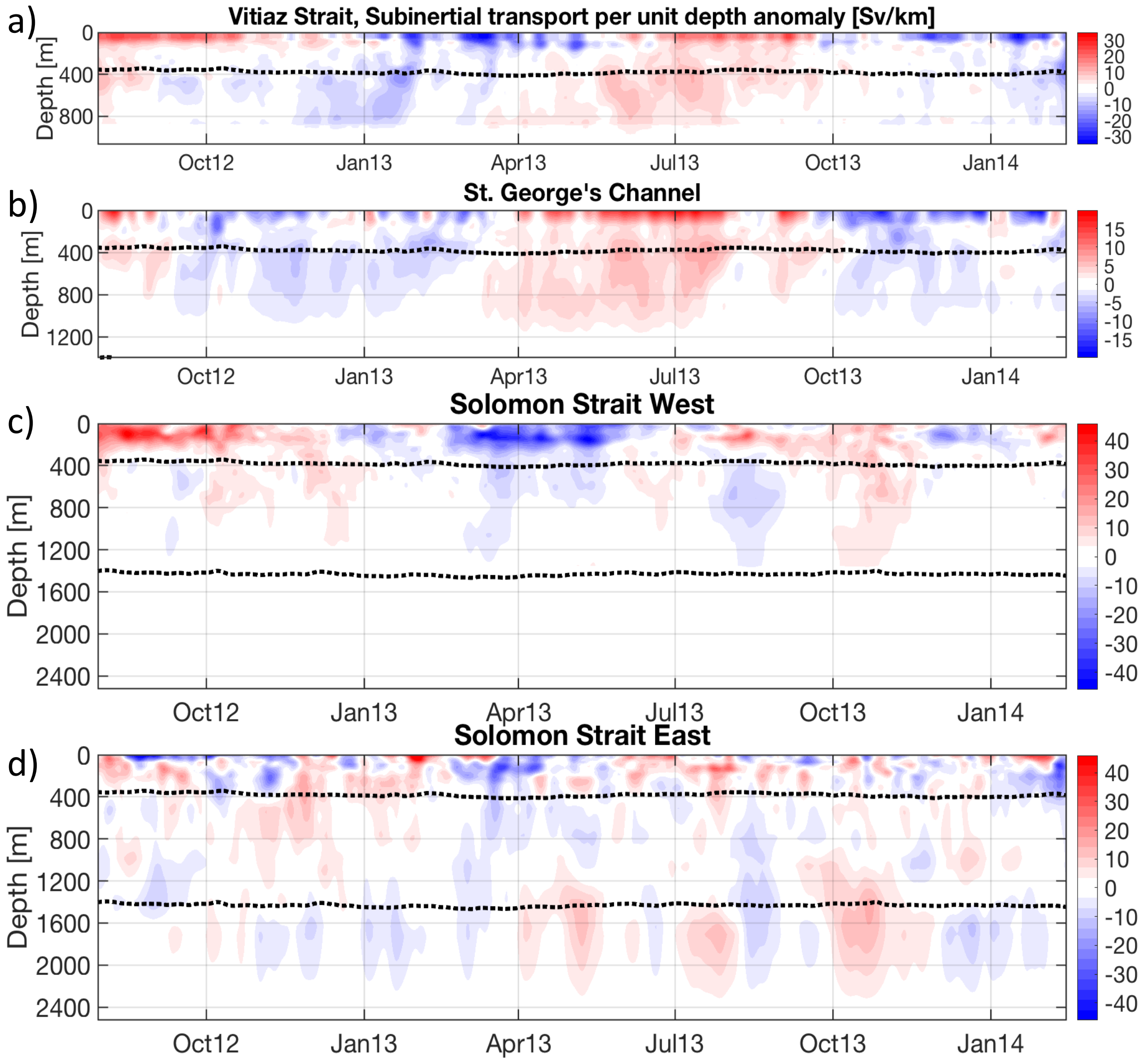

Figure 3.9: The subinertial transport per unit depth anomaly [Sv/km] for a) Vitiaz Strait, b) St. George's Channel, c) Solomon Strait West from New Ireland to Solomon M2, and d) Solomon Strait East from Solomon M2 to the coast of Bougainville Island. Positive values (red) indicate transport anomalies exiting the Solomon Sea while negative values (blue) indicate transport anomalies entering the Solomon Sea. The dotted black lines indicate the mean depths of the $\sigma_0 = 26.7$ and $\sigma_0 = 27.5$ isopycnals. Note the different scales of the colorbars for each panel.

3.6 Results: Water Mass Characteristics and Variability

3.6.1 Surface and Thermocline Waters

Due to instrument loss and mooring draw down, thermocline water properties ($23.3 < \sigma_0 \leq 26.7$) are only observed in Solomon Strait and surface water properties ($\sigma_0 \leq 23.3$) are only observed at Solomon M2 and M3 over the deployment period (Figure 3.10). Solomon moorings M2 and M3 observed similar patterns of seasonal freshening and salinification of surface waters. In August-September when SEC transport is minimum, surface waters at M2 and M3 are fresher and exhibit temperature-salinity (T-S) structure that is similar to mean surface layer profiles from the NBCU region (Figure 3.10). As the season progresses and SEC inflow increases, surface waters generally become saltier, reaching a maximum in April-May, transitioning to T-S relationships which are more similar to mean SEC surface layer water masses. While surface layer salinity varies similarly between the two moorings over the deployment period, the direction of transport is not consistent between each mooring indicating recirculation (Figure 3.10e,f).

The subsurface salinity maximum associated with SPTW is observed at all three Solomon Strait moorings but is distinctively modified compared to SPTW upstream in the NVJ or NBCU (Figure 3.10). This feature is also fresher and broader in temperature on the western side of Solomon Strait compared to the eastern side. Even across the relatively short distance between Solomon M1 and M2, SPTW transported out of the Solomon Sea (positive ASV) has a weaker salinity maximum at Solomon M1, except for the period of August-December 2012 when thermocline waters at M2 are distinctively fresher than those observed at M1. Thermocline waters at M1 and M2 that are associated with inflows (negative ASV) tend to be saltier and have T-S

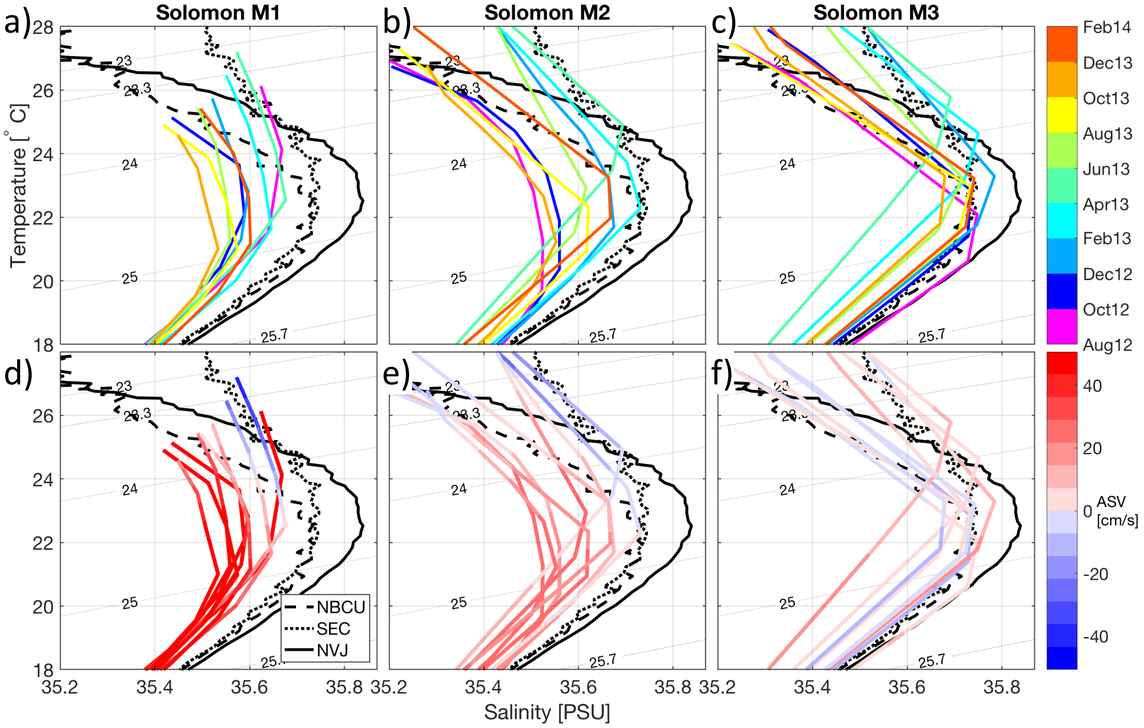

Figure 3.10: Temperature-Salinity diagrams for moorings (a,d) Solomon M1, (b,e) M2, and (c,f) M3, color-coded by average (a-c) time and (d-f) ASV [cm/s]. The Argo density-mean temperature and salinity relationships for NBCU region (dashed black line), SEC entrance region (dotted black line), and NVJ entrance region (solid black line) water masses are shown for reference. The locations of the referenced Argo profiles and full Argo density-mean T-S curves are shown in Figure 3.2.

structure that is more similar to the mean SEC T-S profile. Thermocline water mass variability at Solomon M3 is less variable and there is no clear pattern between T-S variability and transport direction.

3.6.2 Intermediate

Variability of intermediate temperature and salinity is observed at all three straits over the deployment period (Figures 3.11). A prominent salinity minimum typically associated with intermediate waters is observed in all three channels but is saltier and warmer compared to upstream characteristics at the GPC entrance. However significant variability of intermediate water properties is observed during the first half of the deployment period in Vitiaz Strait and St. George's Channel. In Vitiaz Strait, a remarkably warm and salty water mass associated with outflowing ASV is observed in August-September 2012 (Figure 3.11a & d). Over the remaining observational period, water mass properties cool and freshen, with a salinity minimum of 34.49 PSU for waters of 6.5°C emerging in April/May 2013.

In St. George's Channel, intermediate waters are also observed to be warmer and saltier in August 2012 through April 2013 (Figure 3.11b & e). In August-September 2012 warm, salty water flows out of the Solomon Sea into the Bismark Sea before transport reverses and even saltier and warmer waters from the Bismark Sea are advected through St. George's Channel in October 2012 until January 2013. Intermediate transport reverses direction again in February 2013 with water properties cooling and freshening through July 2013 as intermediate transport out of the Solomon Sea through St. George's Channel strengthens.

Intermediate water masses at Solomon M1 are observed to be cool and fresh in August 2012 through January 2013 with a salinity minimum that is salty compared to GPC waters but fresher than Equatorial Pacific Intermediate Waters generally observed in the SEC entrance region (Figure 3.11c & f). In February and March 2013, lower intermediate transport ($\sigma > 27.1$) reverses and saltier waters are advected by Solomon M1 while upper intermediate water mass temperature and salinity remain relatively constant. This period of inflow continues into May 2013 with lower intermediate water mass properties resembling those in the SEC region. However, transport changes direction again by August 2013 and intermediate waters get cooler and fresher again.

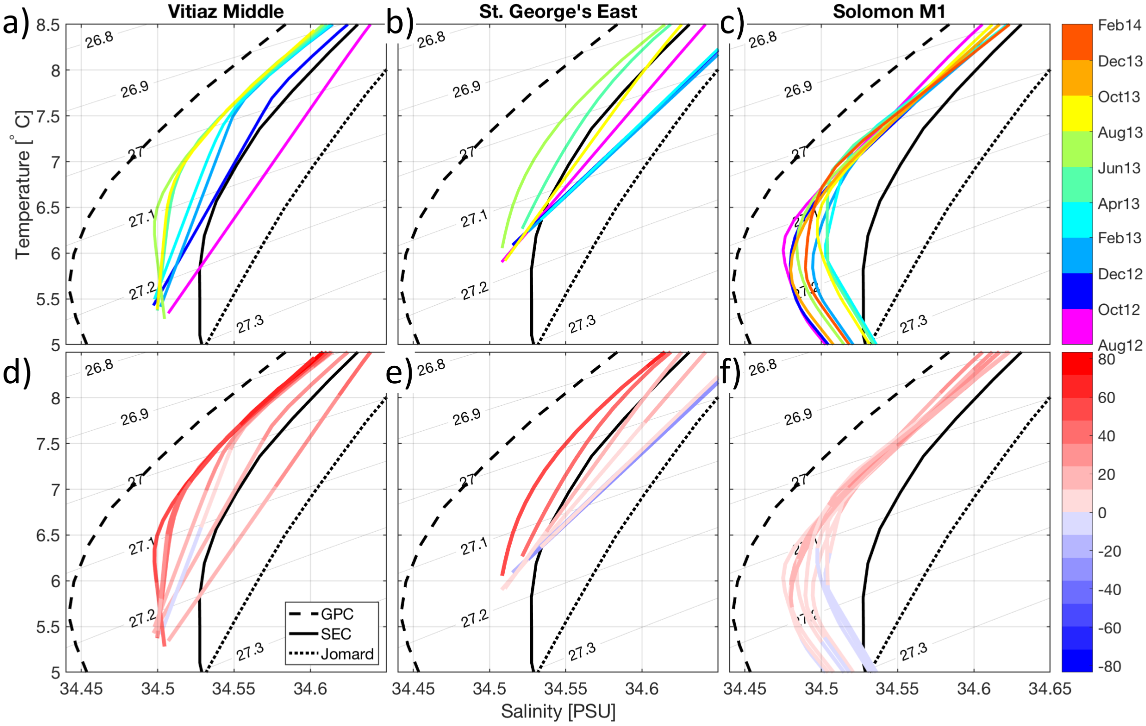

Figure 3.11: Temperature-Salinity diagrams for mooring (a,d) Vitiaz Middle, (b,e) St. George's East, and (c,f) Solomon M1, color-coded by (a-c) time and (d-f) ASV [cm/s]. The density-mean temperature and salinity relationships for the GPC inflow region (dashed black line), SEC entrance region (solid black line), and Jomard Entrance (dotted black line) are shown for reference. The locations of the referenced Argo profiles and full Argo density-mean T-S curves are shown in Figure 3.2.

3.7 Discussion

3.7.1 Summary of Results

An average of 22.8±3.5 Sv of total transport from the ocean surface to the base of AAIW ($\sigma_0 = 27.5$) is observed to exit the Solomon Sea through the combination of Vitiaz Strait, St. George's Channel, and Solomon Strait (Table 3.3). Over half of this transport exits through Vitiaz Strait with 36.2% exiting through Solomon Strait and 9.6% passing through St. George's Channel. A deep transport of -4.6 ± 1.0 Sv is observed to enter the Solomon Sea through Solomon Strait over the deployment period (Figure 3.5). In the top 100 m transport enters the Solomon Sea through Solomon Strait and is partially balanced by transport exiting the Solomon Sea through Vitiaz Strait (Figure 3.6). Total transport has a subsurface maximum at 200-300 m depth, a common feature of all three straits, though Vitiaz Strait and Solomon Strait West transport the dominant contributions. Vitiaz Strait supplies the largest fraction of the total transport, with positive mean transports at all depths, while the large intraseasonal variability of the total transport is the result of intraseasonal variability in Solomon Strait East (Figures 3.7). Over the deployment period, water mass variability is observed from the surface layer all the way down to intermediate isopycnals (Figures 3.10 & 3.11). Some of this water mass variability is linked to the direction of transport through each channel.

3.7.2 Vitiaz Strait

The annual cycle of winds stress curl over the South Pacific western subtropical gyre generates a standing Rossby wave that spins the gyre up and down in phase with wind stress curl variability (Kessler & Gourdeau, 2007). Gyre spin up from August to October reduces GPC transport, increases NVJ transport and results in an anomalously strong NGCC and NBCU (Melet *et al.*, 2010*a*). This LLWBC strengthening is observed at Vitiaz Strait, where surface and thermocline transports are found to be in phase and correlated ($R = 0.62$ for the surface & $R = 0.59$ for the thermocline) with CCMP wind stress curl over the western subtropical gyre ($13° - 20°$S, $150° - 160°$E). While there are prior synoptic observations of surface reversals in Vitiaz Strait (Cravatte *et al.*, 2011), sustained periods of surface current weakening and reversal have not previously been observed (Figure 3.8a). Surface velocities in Vitiaz Strait are found to be in phase, aligned, and well correlated with local CCMP winds ($R = 0.71$), including over the sustained periods of surface transport reversals, when ADCP coverage extends up to 50 m depth. Since Vitiaz Strait is narrow, surface flow is constrained by topography and the Coriolis force is relatively weak it this latitude, it is likely that surface flow is accelerated by and aligned with wind stress.

The variability of temperature and salinity along intermediate isopycnals in Vitiaz Strait is remarkable with temperature varying by > 0.5°C and salinity by > 0.1 PSU along the $\sigma_0 = 27.1$ isopycnal over the deployment period. The warmest and saltiest intermediate waters observed are also associated with outflowing transports, indicating an upstream origin for this water property variability. The cause of this water mass variability remains an open question. One possibility is intermittent and enhanced upstream diapycnal mixing along intermediate water pathways. A second possibility is variable sources of intermediate waters that are transported through the Solomon Sea and Vitiaz Strait. Argo observations of waters from the SEC entrance region and the Jomard entrance are warmer and saltier compared to waters that enter the Solomon Sea via the GPC and may be sources of the observed T-S variability in Vitiaz Strait (Figures 3.1a, & 3.11).

3.7.3 Solomon Strait

Seasonal variability of the SEC is driven by the annual propagation of off-equatorial Rossby waves which modulate the meridional location of the SEC and thus where the current impinges upon the eastern boundary of the Solomon Sea (Melet *et al.*, 2010*b*). Simulations by Melet *et al.* (2010*a*) also indicate a westward propagation of the annual transport anomalies across Solomon Strait with the western side lagging the eastern side by approximately one month, with maximum seasonal transport on the western side of the strait in October-November. In addition, the modeled seasonal cycle of thermocline transport is generally aligned with the channel cross-section on the eastern side while the seasonal cycle on the western side is nearly orthogonal to the western cross-section and twice as large.

As such it is not surprising that surface and thermocline transports across Solomon Strait West are well correlated ($R = -0.75$ for the surface layer & $R = -0.84$ for the thermocline) and in phase opposition with sea level anomalies (SLA) outside Solomon Strait where the annual Rossby wave is observed to reach the Solomon Sea (SLA averaged over $4°-6°$S, $155°-158°$E). Positive SLA anomalies in this region indicate the presence of a downwelling Rossby wave east of Solomon Strait that enhances westward SEC transport equatorward of the Rossby wave crest and thus transport into the Solomon Sea (Melet *et al.*, 2010*a*,0). These westward SEC anomalies manifest as negative transport anomalies across Solomon Strait West in both the surface and thermocline layers. The lowpass filtered transport out of Solomon Strait West is also maximum in October and lags seasonal timescale variability of transport through Solomon Strait East by one month, in agreement with predictions.

Thermocline transport across Solomon Strait East is only weakly correlated ($R = -0.39$) with SLA outside of Solomon Strait and surface transports across Solomon Strait East are not strongly correlated with the annual Rossby wave SLA

($|R| < 0.2$ for time lags/lead $\leq$ 100 days). The zonal orientation of the annual cycle of transport on the eastern side of Solomon Strait likely contributes to the weak correlation between upper ocean transport and SLA associated with the annual Rossby wave. Additionally, given that there is 10 times more variance at intraseasonal timescales compared to seasonal time scales in Solomon Strait East, a weak correlation with seasonal scale forcing is not surprising. Other dynamical features, such as mesoscale eddies, may have a stronger influence on transport variability across Solomon Strait East, potentially responsible for the enhanced variance observed at intraseasonal timescales. Surface eddy kinetic energy is observed and modeled to be enhanced at Solomon Strait (Melet *et al.*, 2010*b*; Hristova & Kessler, 2012; Hristova *et al.*, 2014; Djath *et al.*, 2014; Srinivasan *et al.*, 2017).

Coherent mesoscale eddies have also been observed in Solomon Strait (Melet *et al.*, 2010*b*) and modeled mean stream functions indicate a recirculation pattern where 67% of surface water transport that exits through Solomon Strait also entered through Solomon Strait approximately 45 days earlier (Melet *et al.*, 2011). Surface water properties at Solomon M2 and M3 may reflect the presence of eddies and recirculation in Solomon Strait with periods when surface ASV are in opposing directions but water mass properties are quite similar (Figure 3.10b-c & e-f).

Solomon Strait deployment mean transport at the thermocline depth (100-300 m) is estimated to be comparable to thermocline transport through Vitiaz Strait (Figure 3.6a). Solomon Sea thermocline waters are thought to be the primary source waters for the EUC, though previous simulations have traced a larger fraction of EUC transport back to Vitiaz Strait compared to Solomon Strait (Grenier *et al.*, 2011; Qin *et al.*, 2016). Models of thermocline transport have also reported nearly twice as much thermocline transport in Vitiaz Strait compared to Solomon Strait (Melet *et al.*, 2010*a*; Djath *et al.*, 2014). Because both Vitiaz Strait and Solomon

Strait transport estimates are sensitive to the cross-passage extrapolation model, it is not possible to conclusively say which strait is the primary source of thermocline transport to the equatorial Pacific, however results suggest that Solomon Strait may supply a larger fraction than previously predicted.

Thermocline T-S patterns suggest that in general NICU thermocline waters on the western side of Solomon Strait tend to be more modified compared to those more toward the center of the channel at Solomon M2. Stream functions from Melet *et al.* (2011) suggest that water parcels on the western side will have been in closer contact with the topographic boundaries of the Solomon Sea and Srinivasan *et al.* (2017) demonstrate that the LLWBCs drag against the topography generating submesoscale features in the Solomon Sea. Similar topographically induced submesoscale features have been linked to increased dissipation and water mass mixing (Molemaker *et al.*, 2015) and may be partially responsible for the asymmetric water mass modification observed across the NICU.

Transport anomalies are generally coherent over intermediate and deep isopycnals across Solomon Strait East (Figure 3.8d & 3.9d). Alternating zonal jets that are coherent vertically from 600-1500 m depth are observed to impinge upon the eastern side of the Solomon Sea at Solomon Strait (Cravatte *et al.*, 2012,0). Prior observations indicate the downward propagation of annual Rossby waves drive the seasonal variability of these zonal jets. Maximum westward anomalies are observed in December-May and eastward anomalies in June-November at the latitude and longitude of Solomon Strait. Westward anomalies of the intermediate zonal jet are expected to translate to negative transport anomalies through Solomon Strait, though interactions with topography near Solomon Strait may complicate this seasonal variability. While our observations do not offer conclusive evidence that the vertically coherent variability over intermediate and deep layers in Solomon Strait are in deed these zonal jets, understanding the fate these deep zonal jets as they approach Solomon Sea merits further investigation.

3.7.4 St. George's Channel

Planetary waves like Rossby and coastally-trapped Kelvin waves are expected to be important for modulating transport throughout the Solomon Sea. The geography around St. George's Channel, and around all three channels for that matter, complicates the propagation of these waves making the interaction of these planetary waves with the mean currents challenging to observe or model, particularly at depth.

Previous modeling work suggests that 61% of surface water transport through St. George's Channel can be traced back to Solomon Strait, suggesting that surface transport variability in Solomon Strait has a direct connection to St. George's Channel (Melet *et al.*, 2011). Surface transport through St. George's Channel is moderately correlated ($R = -0.51$) with surface transport through Solomon Strait West, with periods of anomalous SEC transport into the Solomon Sea through Solomon Strait West leading enhanced surface transport out through St. George's Strait by 45 days (Figure 3.9b-c). Surface currents in St. George's Channel are not well correlated with local winds ($R = 0.27$). While local winds are expected to have an influence on surface currents, the lack of clear relationship could stem from several issues. One is simply the large uncertainties in surface current direction and magnitude due to a lack of velocity observations in the top 100 m of the water column, especially in the months of March to September. The second is the quality of the CCMP surface winds in the narrow St George's Channel.

Simulations indicate that thermocline transport in St. George's Channel is primarily supplied by the NBCU (90%) (Melet *et al.*, 2011). Thus, the strength of thermocline transport through St. George's Channel is expected to depend upon the strength of the NBCU and the partitioning of the NBCU between St. George's Channel and Solomon. Model results indicate that NBCU transport varies seasonally and is maximum in September. Thermocline transport in St. George's Channel is maximum in May-June, 3-4 months before NBCU thermocline transport is predicted to be maximum (Figure 3.8b and 3.9b). However the sum of thermocline transport in St. George's Channel and Solomon Strait West varies seasonally and in phase with modeled NBCU transport variability suggesting that NBCU partitioning also varies seasonally. What determines the partitioning of the NBCU between the two channels remains an open question.

While intermediate transport through St. George's Channel is small, the seasonal exchange of water masses between the Solomon Sea and Bismark Sea at that depth may be of importance, particularly as deep-sea mining operations are planned for the Bismark Sea. Material transport associated with mining plumes was recently modeled by Coulin *et al.* (2017) for the region and St. George's Channel in particular. That and previous modeling studies have not noted seasonal reserving of intermediate transports. The observed sustained reversals will influence the transport of materials which current operational forecasts of the region may not resolve at present.

3.8 Final Remarks

Accurately estimating the transport and partitioning of South Pacific LLWBC transport into the Equatorial Pacific is necessary to correctly simulate EUC water mass properties and variability. These observations have, for the first time, simultaneously resolved thermocline-to-sill-depth transport, variability, and channel partitioning in the Solomon Sea over an 18-month deployment. Because transport estimates are sensitive to cross-passage extrapolation schemes, an inter-comparison of the moored velocity observations and modeled profiles of velocity in the Solomon

Sea straits is recommended to better constrain the contributions of Vitiaz Strait and Solomon Strait waters to the EUC. These results suggest that the contribution from Solomon Strait may be under estimated at present. Water parcels that travel through the Solomon Strait reach the EUC more quickly than those that pass through Vitiaz Strait (Grenier *et al.*, 2011; Qin *et al.*, 2016). As iron concentrations are related to transit times through scavenging processes, this result may have implications for understanding the nutrient sources of equatorial Pacific primary productivity.

Significant uncertainty still remains concerning the variability of surface currents in the Solomon Sea channels. In Vitiaz Strait and St. George's Channel, the strong currents and highly trafficked channels make traditional mooring observations challenging and limit observations of temperature and salinity in the upper part of the water column. In Solomon Strait, surface geostrophic velocities from satellite products have limited capabilities due to signal contamination by nearby land, limiting reliable estimates to the middle of the strait. Novel observing techniques will likely be needed if future studies wish to better resolve upper ocean currents and water properties. High-frequency radar observations could potentially be utilized to resolve surface currents, with the capability to resolve hourly currents at kilometer scale horizontal resolution across the straits (Paduan & Washburn, 2013). It should be noted however such radar systems may present operational challenges due to power consumption and maintenance requirements.

The LLWBCs of the Solomon Sea have been highlighted by the Tropical Pacific Observing System (TPOS) 2020 project as a key component of tropical circulation that requires sustained monitoring (Cravatte *et al.*, 2016). To successfully monitor transport through the Solomon Sea, planned observing systems will need to be designed such that the strong intraseasonal variability observed in Solomon Strait is not aliased onto annual and interannual time series. Longterm mooring deployments in Solomon Strait may be a potential solution given the observed large intraseasonal variability in the strait, relatively high data return, and minimal mooring draw down compared to Vitiaz Strait and St. George's Channel. Maintaining sustained moorings in Vitiaz Strait presents an engineering and operational challenge.

Additional moorings were redeployed in March 2014 at Vitiaz Strait and Solomon Strait and recovered in August 2015 during the CASSIOPEE cruise on board *R/V l'Atalante*. These observations will extend the mooring time series and help to better understand the seasonal, interannual and intraseasonal variability of the transports in the straits. During the combined mooring deployment period (July 2012 to August 2015), a pair of gliders (Davis *et al.*, 2012) and an array of bottom pressure sensors with dynamic height moorings (*Anutaliya et al. in prep*) were deployed in the southern section of the Solomon Sea, independently monitoring transport through the southern opening. The glider observations are the longest source of continuous transport observations in the Solomon Sea but their sampling scheme aliases intraseasonal transport variability. The array of bottom pressure sensors with dynamic height moorings resolve intraseasonal transport variability but do not resolve the vertical structure of transport in the Solomon Sea. All three of observing systems have different strengths and would benefit from an inter-comparison of transport estimates during the overlapping deployment periods. The results from such an inter-comparison would be very valuable for designing a long-term monitoring system for the Solomon Sea LLWBCs as recommended for TPOS 2020.

Finally, while high frequency processes are beyond the scope of this paper, these mooring observations fully resolved super-inertial time scales in all three channels over much of the water column. Velocity variance at these frequencies is significant compared to subinertial frequencies. Such processes are generally important for water mass modification and are likely influenced by the sub-inertial processes investigated within this paper.

3.A Extended Discussion of Data and Methods

3.A.1 Estimated Salinity at 1700 m depth on Mooring Solomon M2

One significant loss for the Solomon Strait moorings was the failure of the deepest conductivity, temperature and pressure sensor at 1700 m depth on mooring Solomon M2a. As the next deepest conductivity sensor on Solomon M2a was located at 700 m depth, this loss would limit the geostrophic transport estimate to above 700 m depth. In an attempt to mitigate this loss, the temperature and pressure record from a sensor deployed at 1700 m depth on Solomon M2b and nine shipboard CTD profiles from the Pandora and MoorSPICE cruises taken at the mooring location are used to estimate the missing salinity record. Over the range of temperatures observed by a thermistor at 1700 m on Solomon M2b ($3 - 2.3$°C), a tight linear relationship between temperature and salinity is found from the shipboard CTD profiles (R$= -0.99$). Thus salinity for the temperature sensor moored at 1700 m is estimated based on the linear relationship determined from the CTD profiles. To test the potential error associated with this method, a similar analysis is performed for the sensors at 1700 m depth on moorings Solomon M1 and M3. CTD casts at the locations of mooring Solomon M1 and M3 also are found to have tight linear relationships between temperature and salinity, with R$= -0.99$ for both moorings, over the temperature ranges observed by each sensor. Salinity time series are estimated from the linear relationships for both sensors and compared with the sensor's observed salinity. A root-mean-square difference between the observed and estimated salinity of 0.0017 PSU for Solomon M1 and 0.0021 PSU for Solomon M3 is found.

3.A.2 Geostrophic Velocity in Solomon Strait

Using the maximum mean ASV (60 cm/s) and channel width (185 km) which limits the lateral scale of flow, Solomon Strait is found to have a Rossby number less than unity ($Ro = 0.3$), Thus we expect that even for the fastest flows, the effect of planetary rotation is important within Solomon Strait and so we chose to use the geostrophic approximation to estimate transport in the channel.

On average, the shallowest density observations are at 170 m, 90 m, and 80 m depth for Solomon M1, M2 and M3, respectively, and extend down to 1700 m depth for all three mooring locations (Figures 3.3a-c & 3.5d, black dots indicate mean location of density observations). Discrete density observations from CTD sensors are linearly interpolated onto a regular vertical grid with 20 m spacing. Gridded density (ρ) is used to estimate vertical shear using the Thermal Wind equations:

$$-f\frac{\partial v_g}{\partial z} = g\frac{\partial \rho}{\partial x}, \quad f\frac{\partial u_g}{\partial z} = g\frac{\partial \rho}{\partial y}, \tag{3.3}$$

where u_g, v_g are geostrophic velocity, f is the Coriolis frequency, and g is gravitational acceleration. As geostrophy can only estimate the component of the flow normal to the line between profiles of density, geostrophic shear is estimated separately for Solomon Strait West and East. For Solomon Strait West (between Solomon M1 and M2), geostrophic shear in the along strait direction is estimated from 170 m down to 1350 m depth, below which a sea mount impedes the calculation. At Solomon M1 and M2, the observed ASV at 1350 m is used to integrate the shear vertically upwards and below 1350 m the directly observed ASV is used from 1350 m down to 1700 m depth. For Solomon Strait East, (between M2 and M3), the along strait component of geostrophic shear is estimated from 90 m down to 1700 m depth. At each mooring along Solomon Strait East, shear is integrated vertically and referenced to the observed ASV at 1700 m depth.

Because geostrophy estimates vertical shear from the lateral density gradient at a particular depth, it is optimal to have concurrent density observations at the same depth. While the moorings were designed to measure density at many of the same depths across Solomon Strait, mooring draw down, which varies in time and between moorings, results in sensors measuring significantly different depths across the three moorings at any given time, though increased vertical resolution of sensors helps to mitigate this problem. Nonetheless, for portions of the water column where the vertical structure of density is not well approximated by linear interpolation, namely above the thermocline, the vertical interpolation process will result in biased estimates of the density gradients across Solomon Strait. Additionally, the failure of two CTDs at 300 and 550 m depth at mooring Solomon M2 further degrades the quality of the geostrophic estimate over the latter half of the transport time series.

The same vertical and cross-passage extrapolation schemes described in Sections 3.4.2 and 3.4.3 are use to generate gridded cross-sections of geostrophic ASV. For the Satellite Inferred method, the shallowest geostrophic ASV is linearly interpolated to the satellite surface geostrophic estimate and the Ekman profile is added to the profile of geostrophic ASV. The mean ASV cross-section over the deployment period estimated from geostrophy for Solomon Strait using the Satellite Inferred, Linear to Bottom, and Boundary Intensification schemes is shown in Figure 3.12 for reference.

3.A.3 Transport from Geostrophy and Direct Observations of Velocity in Solomon Strait

The mean cross-sectional structure of ASV from the geostrophic estimate agrees well with in-situ velocity observations on the western side of the strait below 200 m depth and below 1000 m depth on the eastern side. Above 1000 m depth,

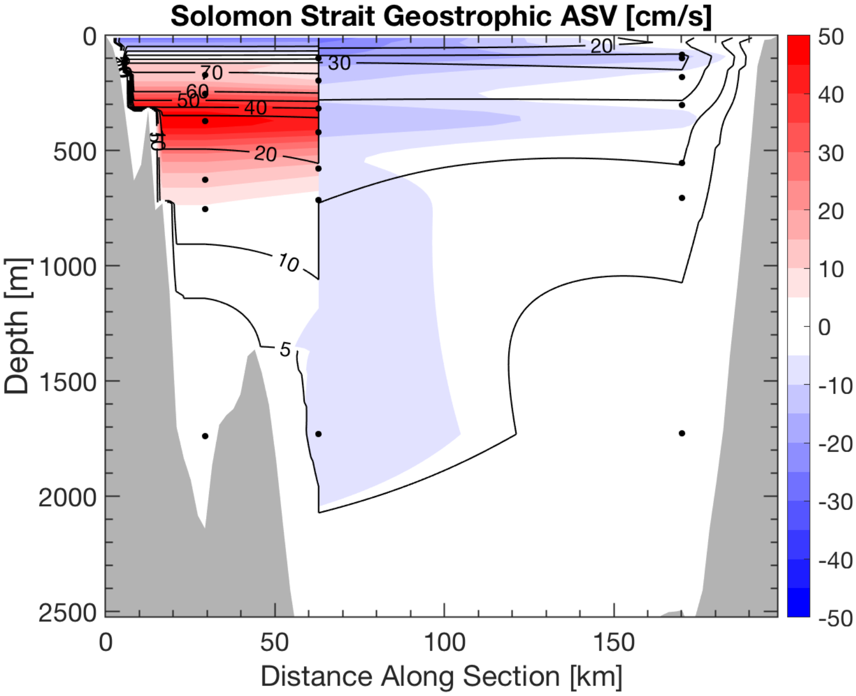

Figure 3.12: The mean (red-blue colormap) and standard deviation (black contours) of the ASV [cm/s] for Solomon Strait estimated using geostrophy. Statistics were calculated over the deployment period and the vertical limits are the ocean surface to each channel's respective sill depth. Mean ASV sections are contoured at 5 cm/s increments and red indicates transport exiting the Solomon Sea while blue indicates transport entering. The standard deviation of the along strait velocity is contoured in 10 cm/s intervals with an additional 5 cm/s contour. Deployment-mean locations of all density observations are indicated with black dots for the directly observed velocity sections. Note the discontinuity across Solomon Strait is due to the discontinuous transect line used for the channel cross-section (Figure 3.1b).

geostrophic transport is estimated to flow in the opposite direction through Solomon Strait East compared to in-situ velocity observations. Only the Satellite Inferred surface scheme replicates the shallow inflow above 100 m depth that is also observed in the mean SADCP cross-section on the western side of the strait as the geostrophic estimate can not on average resolve the top 170 m of the water column at Solomon Strait West.

Total transport time series estimated using geostrophy and in-situ velocity observations in Solomon Strait are compared in Figure 3.13a, with individual lines representing each permutation of the various extrapolation methods. Solomon Strait transports from the surface to the base of the thermocline ($\sigma_0 = 26.7$) estimated from geostrophy and in-situ velocity observations are well correlated from July 2012 until April 2013 ($R = 0.59$, $p-$value$= 0.00$), but are weakly ($R = 0.12$) and less statistically significantly correlated ($p-$value$= 0.03$) after the loss of the CTD at 550 m depth in April 2013 (Figure 3.13b). Below the base of the thermocline, transports remain well correlated over the entire deployment period ($R = 0.81$, $p-$value$= 0.00$), but the range of transport from the geostrophic estimate increases significantly compared to the transport estimate from direct observations after April 2013 (Figure 3.13c). The reasonable agreement in transport variability prior to the loss of CTD coverage on Solomon M2a suggests that transport estimated from in-situ velocity observations may be a reasonable estimate of mesoscale transport.

3.A.4 Sensitivity of Transport to Vertical Extrapolation

To investigate the consistency of the vertical extrapolation schemes compared to previous observations, historical (Cravatte *et al.*, 2011) and recent (Germineaud *et al.*, 2016; Ganachaud *et al.*, 2017) shipboard ADCP (SADCP) profiles located within 20 km of the above defined channel cross-sections (Figure 3.1b) were projected

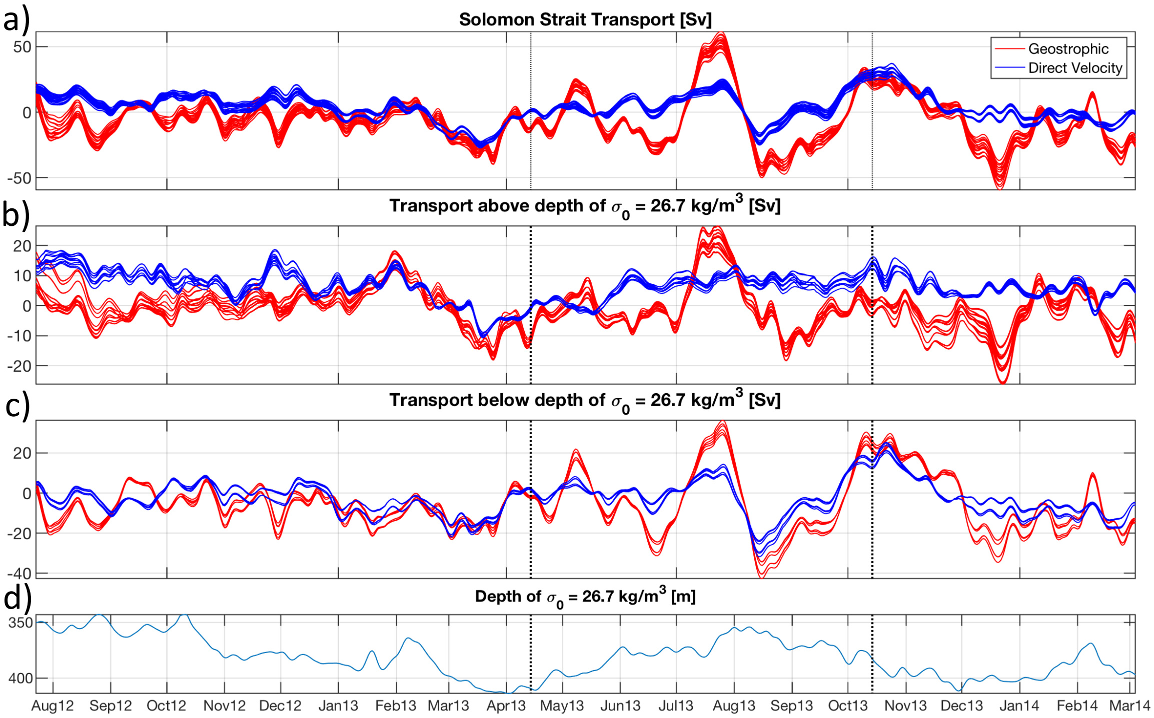

Figure 3.13: Transport time series at Solomon Strait from (a) the surface to sill depth, (b) the surface the depth of the $\sigma_0 = 26.7$ isopycnal, and (c) the depth of the $\sigma_0 = 26.7$ isopycnal to the sill depth for all model combinations using geostrophy (red lines) and in-situ velocity (blue lines) to estimate transport. (d) Time series of mean $\sigma_0 = 26.7$ isopycnal depth in Solomon Strait. The time of instrument failures on mooring Solomon M2 are demarcated by the dotted black lines in all panels.

onto the along-strait direction and averaged across each channel to produce mean ASV cross-sections (Figures 3.3 & 3.4, black contours). It should be noted that profiles at these locations are predominately from the months of February to July, with the largest data contribution coming from July 2012 and March 2014, thus seasonal bias likely contributes to the SADCP mean ASV cross-channel structure. These mean SADCP sections are compared to examples of ASV cross sections produced using the different vertical schemes for each channel (Figures 3.3 & 3.4, red-blue filled contours).

In Solomon Strait, Constant Shear and Satellite Inferred surface models both replicate the shallow reversal of the flow near New Ireland and produce surprisingly similar estimates of the mean ASV cross-section, with deployment mean transport differing by only 0.9% (Figure 3.3f-g, Table 3.4). An additional Satellite Inferred surface model was tested for Solomon Strait using Eulerian surface velocities (Ekman + Geostrophic) from the GlobCurrent analysis (http://globcurrent.ifremer.fr/, Rio *et al.* (2014)). Solomon Strait transport was insensitive to the choice of GlobCurrent, with transport changing by $< 3\%$ compared to the previously described Satellite Inferred method.

The mean SADCP section in Solomon Strait does indicate that the western inflow has a subsurface maximum rather than being surface intensified as is suggested by the Satellite Inferred schemes (Figure 3.3). While this shallow inflow is above the mean depth of the shallowest ADCP bin (70 m depth) of Solomon M1, the upward looking ADCP at M1 does resolve a pronounced inflow from the surface extending down to 200 m in February-June 2013 when mooring draw down is minimal and coverage extends up to 10-30 m depth. As most SADCP profiles are also from these months, it is possible that this is a seasonal feature over represented in the SADCP data and not representative of mean vertical structure. There remains uncertainty for both the SADCP and moored ASV mean sections in the top 70 m near New Ireland during the months of September-December.

In Vitiaz Strait, the Slab to Surface vertical extrapolation scheme is most representative of the mean SADCP transect (Figure 3.4a-b) and consistent with observations of the mean ASV cross-section by Cravatte *et al.* (2011). In addition, transport through Vitiaz Strait is relatively insensitive to the chosen surface model with the deployment-mean total transport decreasing by 3.7% when the Constant Shear surface model is used rather than the Slab model (Table 3.4).

For St. George's Channel the Constant Shear model is a better approximation of the mean SADCP ASV cross-section, which is strongly sheared above 200 m and reverses direction from inflow to outflow below 100 m depth (Figure 3.4c-d). Mean ASV cross-sections in St. George's Channel from Cravatte *et al.* (2011) also indicate that the current is sheared above 200 m, approaching zero or potentially reversing above 50-100 m depth. Since on average the top 100 m of the water column in St. George's Channel was unresolved, transport through St. George's Channel is more sensitive to the surface model with the deployment-mean total transport decreasing by 9.6% when the Constant Shear model is used compared to the Slab to Surface model (Table 3.4).

In Solomon Strait, transport is sensitive to the bottom extrapolation scheme. Relatively strong flow (mean ASV of 8 cm/s) is observed entering the Solomon Sea at 1700 m depth at Solomon M2 and is interpolated across a vertical extent of 825 m to the channel's sill depth (2525 m depth). Deployment-mean transport increases by 43.2% when Linear to Bottom is used rather than Slab to Bottom. No published observations exist to support a choice for the most appropriate near-bottom extrapolation model for Solomon Strait, however the linear interpolation to zero at bottom is the more conservative choice.

The transport through Vitiaz Strait is not sensitive to the bottom model (Table 3.4), as the ADCP observations extend nearly to the sill depth for the entire deployment period (Figure 3.5a-b). The estimated transport is essentially insensitive to the bottom model in St. George's Channel as well, with only a 0.6% decrease in deployment-mean transport when the Linear to Bottom model is employed rather than Slab to Bottom.

3.A.5 Sensitivity of Transport to Cross-Passage Extrapolation

Deployment mean transport is sensitive to the lateral interpolation model for all three channels (Table 3.4). Cross channel ASV structure similar to the Linear and Nearest Across Channel methods are found in synoptic observations of Vitiaz Strait and St. George's Channel, indicating temporally varying velocity structure. Furthermore, the Linear Across Channel scheme provides a conservative, lower bound for the mean transport while the Nearest Across Channel is likely an upper bound for all three channels. Modeled and observed ASV cross-sections are found to have enhanced velocities along the western boundary in Vitiaz and Solomon Strait and along the eastern boundary in St. George's Channel (Lindstrom *et al.*, 1990; Cravatte *et al.*, 2011; Djath *et al.*, 2014; Germineaud *et al.*, 2016). This cross-channel structure is best approximated by the Boundary Intensification method.

Solomon Strait mean transport increases by 41.6% when the Nearest Across Channel method is used compared to Linear Across Channel (Table 3.4). The Boundary Intensification model similarly increases mean transport by 55.5% compared to the Linear method. These sensitivity estimates indicate that Solomon Strait mean transport is most sensitive to extrapolation of ASV at Solomon M1 to the western boundary. Observations by Cravatte *et al.* (2011) and the mean SADCP ASV along the mooring transect indicate that NICU ASV extends from the current core to the western boundary (Figure 3.3). In both the moored and SADCP mean ASV cross-sections, the NICU also extends almost 100 km east from the coast of New Ireland (Figure 3.3).

In Vitiaz Strait, mean transport increases by 63.5% using the Boundary Intensification model compared to Linear Across Channel and nearly doubles when the Nearest scheme is used rather than Linear (Table 3.4). Mean SADCP cross-sections of ASV by Cravatte *et al.* (2011) indicate that ASV is enhanced on the western side of the channel with ASV decreasing to 50 cm/s on the eastern side of the channel. Reasonable agreement in mean ASV cross-channel current structure is found between the Boundary Intensification scheme and mean SADCP channel cross-section for Vitiaz Strait (Figure 3.4). Synoptic observations by Lindstrom *et al.* (1990) find western boundary intensification of the NGCU in Vitiaz Strait in January 1986 but also suggest variability in the ASV current structure as the NGCU had a double core in the center of the channel in July 1985. However, both synoptic cross-sections have weaker ASV on the eastern side of Vitiaz Strait. Transects by Germineaud *et al.* (2016) indicate slight western intensification of ASV in Vitiaz Strait with ASV of 80-100 cm/s extending to both sidewalls. These observations suggest that the Linear model likely underestimates transport through Vitiaz Strait while the Boundary Intensification or Nearest Across Channel models provide more realistic estimates.

Mean transport through St. George's Channel increases by 24.2% or 42.4% when the Boundary Intensification or Nearest Across Channel schemes, respectively, are used to estimate cross-channel ASV structure rather than the Linear model. Eastern boundary intensification is observed for the mean ASV cross-section by Cravatte *et al.* (2016) and in synoptic surveys by Lindstrom *et al.* (1990). While the Boundary Intensification scheme produces an estimate of mean ASV with cross-channel current structure that is similar to prior observations, there are not sufficient SADCP profiles near the mooring transect for a conclusive comparison with the interpolation schemes (Figure 3.4c-d).

Acknowledgements

The moorings deployment and recovery were made possible through concurrent contributions of national funding agencies. The MoorSPICE and Pandora cruises have been co-funded by NSF grant OCE1029487, and by ANR project ANR-09-BLAN-0233-01 and INSU/LEFE project Solwara (IDAO and CYBER). We thank the technical division of INSU (DT-INSU, O. Desprez de Gesincourt, L. Fichen, F. Perault, E. de Saint-Leger, C. Brachet and L. Souarnec); US-IMAGO (J. Grelet, J.-L. Fuda, D. Varillon), for the design of the moorings, their efforts to ensure a timely delivery of instruments or participation at different stages of the cruise organization. We thank the Hydraulics Laboratory at SIO for their mooring expertise (P. Harvey, S. Kawamoto). We are grateful to the crews of the R/V l'Atalante and R/V Thomas G. Thompson for their assistance at sea and dedication to oceanographic research. The Pandora and MoorSPICE cruises are contributions to the CLIVAR/SPICE and GEOTRACES International programs. This publication benefited from several insightful conversations with William Kessler.

The GEBCO_2014 Grid and SID Grid, version 20150318 can be accessed at www.gebco.net. CCMP Version-2.0 vector wind analyses are produced by Remote Sensing Systems. Data are available at www.remss.com. The Ssalto/Duacs altimeter products were produced and distributed by the Copernicus Marine and Environment Monitoring Service (CMEMS) (http://www.marine.copernicus.eu). Historical SADCP observations in the Solomon Sea are available at http://solomonseaoceanography.org/solomonsea/sadcp-data. Pandora and MoorSPICE data can be found at http://www.obs-vlfr.fr/proof/cruises.php. Moor-

SPICE data can also be found through Cruise https://doi.org/10.7284/903044.

Chapter Three is currently being prepared for submission for publication of the material. Alberty, M. S., Sprintall, J., MacKinnon, J., Ganachaud, A., Cravatte, S., and Germineaud, C. The dissertation author was the primary investigator and author of this paper.

Chapter 4

Observations of Submesoscale Mixed Layer Processes in the Arctic

4.1 Introduction

Arctic sea ice extent and volume are decreasing rapidly, creating large new areas of open water during the summer months and influencing regional biology and physics (Kwok *et al.*, 2009; McLaughlin *et al.*, 2011; Wood *et al.*, 2015). Some of the observed Arctic sea ice loss has been attributed to a range of global scale changes such as atmospheric warming of the surface layer (Perovich *et al.*, 2008; Toole *et al.*, 2010), warming of Atlantic and Pacific waters that are advected into the Arctic Ocean (Shimada *et al.*, 2006; Polyakov *et al.*, 2010; Timmermans *et al.*, 2018), anomalous atmospheric circulation (Zhang *et al.*, 2008), and positive ice-albedo feedbacks (Timmermans, 2015). However, only 25% of simulations from the Coupled Model Intercomparison Project Phase 5 (CMIP5) produce sea ice losses as strong or stronger than the observed losses over the satellite era (Stroeve *et al.*, 2012). While the mixed layer heat budget is dominated by solar radiation (Maykut & McPhee, 1995; McPhee *et al.*, 2003; Perovich *et al.*, 2007,0,0), inadequate simulation and parameterization of the advection and mixing of heat in the upper ocean has been identified as a potential contributor to this mismatch in simulated and observed sea ice extent (Flato *et al.*, 2013).

The largest sea ice loss, in both extent and volume, has occurred in the Canada Basin (McLaughlin *et al.*, 2011), the region of the Arctic Ocean north of Canada and Alaska (Figure 4.1). During spring and summer, the atmosphere warms, heating the ocean surface mixed layer, melting sea ice and supplying freshwater to the surface mixed layer. Rivers flux additional fresh water into the basin along the margins and warm Pacific summer water is advected through the Bering Strait and stirred in along the boundary (Rudels *et al.*, 1996; Carmack *et al.*, 2016). These inherently patchy sources of buoyancy are strained and stirred by the mesoscale velocity field and result in complicated patterns of sea surface temperature (SST) and salinity characterized by eddies and fronts (Figure 4.1). In September, the Arctic transitions from net heat gain to net heat loss as the atmosphere cools. The heat that has accumulated in the ocean surface mixed layer is released to the atmosphere until the surface has been cooled enough to form sea ice again. The timing of seasonal ice formation is directly tied to the amount of heat that accumulates in the surface mixed layer over the summer months (Serreze *et al.*, 2009; Serreze & Barry, 2011). Because the Arctic Ocean is salinity stratified however, any heat transported or vertically mixed below the summer halocline can be stored late into the season and cause wintertime sea ice loss when the summer halocline is finally mixed through (Jackson *et al.*, 2010,0). The strength and variability of the vertical heat fluxes within the surface mixed layer during the summer months play a crucial role in the variability of sea ice extent and volume in the Arctic Ocean.

Surface wind stress, surface convection, and near-inertial shear at the base of the mixed layer are understood to drive turbulent mixing within the ocean surface mixed layer (Niiler, 1977; Large *et al.*, 1994). The effects of these processes on the evolution of the surface mixed layer are well approximated by one dimensional models but do not explicitly consider potential interactions between these processes and laterally varying buoyancy and velocity fields (Large *et al.*, 1994). However, recent observational and modeling results indicate mixed layer evolution in the presence of fronts can differ significantly from estimates by one-dimensional models (Weller *et al.*, 1991; Mahadevan, 2006; Mahadevan & Tandon, 2006; Capet *et al.*, 2008; Fox-Kemper *et al.*, 2008; D'asaro *et al.*, 2011; Thomas *et al.*, 2013,0). The processes that develop in the presences of such fronts have small lateral scales ($\mathcal{O}(1)$ km horizontal scale), $\mathcal{O}(1)$ Rossby numbers, and are referred to as submesoscale dynamics.

A range of processes fall under the submesoscale umbrella with some dynamics resulting in enhanced shear and mixing along fronts (Thomas *et al.*, 2013,0) while other submesoscale processes restratify the surface mixed layer and inhibit vertical mixing (Boccaletti *et al.*, 2007; Fox-Kemper *et al.*, 2008). High resolution simulations indicate that a combination of processes are present over the evolution of individual submesoscale fronts with different processes producing competing effects to mix or restratify the surface mixed layer (Mahadevan, 2006; Mahadevan & Tandon, 2006; Capet *et al.*, 2008; Sarkar *et al.*, 2016). There are only a few observations resolving submesoscales in the Arctic (Timmermans *et al.*, 2012; Timmermans & Winsor, 2013; Mensa *et al.*, 2018), however these studies all indicate that such dynamics are likely important for seasonal evolution of the surface mixed layer. In addition, the role of submesoscale dynamics in the surface mixed layer is expected to change as a larger area of Arctic Ocean surface is in direct contact with the atmosphere and for an increasing amount of time each summer (Rainville *et al.*, 2011).

These results raise some of the following questions: Given the rich field of buoyancy fronts during the summer months in the Canada Basin, how do submesoscale dynamics interact with and modulate the one-dimensional processes that control vertical mixing, and thus heat fluxes, in the Arctic surface mixed layer? How do submesoscale gradients evolve over the summer months and inter-annually within the Canada basin? Do seasonal and interannual variability of the submesoscale field translate to seasonal and interannual variability of mixing in the surface layer?

If the Arctic upper ocean heat budget and sea ice are to be correctly modeled, it is necessary to quantify the submesoscale lateral gradients that characterize the Canada Basin in the summer months and investigate the role of submesoscale dynamics on heat fluxes and the evolution of the summer surface mixed layer. A fundamental goal of this chapter is to improve our estimates of submesoscale gradients in the Canada Basin and to investigate the relationship between vertical turbulent heat fluxes in the mixed layer and the strength of submesoscale lateral gradients.

To investigate the relationship between submesoscale dynamics and vertical heat fluxes in the Canada Basin summer surface mixed layer, high resolution observations of the top 20 m were made in the Beaufort Sea of the Canada Basin during September 2015 and 2018. Submesoscale filaments and fronts were observed throughout the study area, including in regions of ice melt and formation (Figure 4.1). The distribution of lateral scales is quantified from horizontal wavenumber spectra of temperature and density at 3-6 m depth and mixed layer observations are also used to estimate the dissipation of thermal variance, which gives an estimate of how vigorously heat is mixed vertically. A positive relationship is found between the variance of temperature over submesoscale and the rate of dissipation of thermal variance in the surface mixed layer.

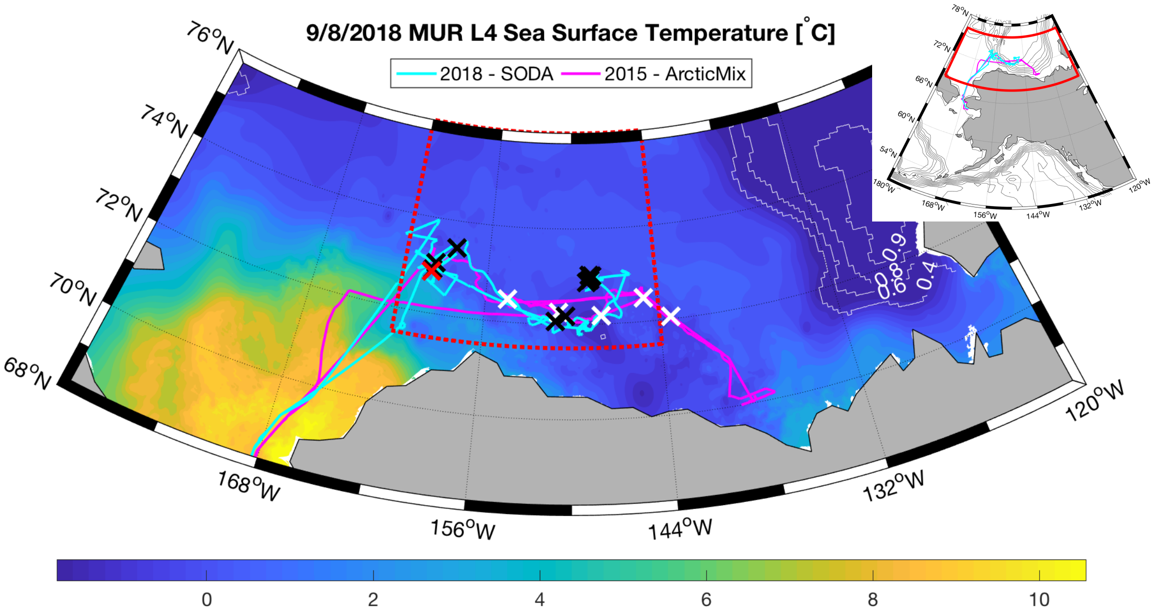

Figure 4.1: Map of the study region with MUR L4 SST [°C] (colormap) and sea ice concentrations (white contours) on September 8, 2018. Cruise tracks are shown for the September 2015 ArcticMix cruise (magenta line) and September 2018 SODA cruises (cyan line). The location of individual bow chain deployments are indicated with x's for September 2015/ArcticMix (white), September 2018/SODA (black), and the September 8, 2018 deployment on SODA (red). The bounds over which satellite SST is analyzed is demarcated by the dotted red lines. The inset map shows the region of interest in the Beaufort Sea, north of Alaska, with the two cruises tracks. The boundary of the main panel is shown by the red box in the inset map.

Given the positive relationship observed between submesoscale variance and the mixing of heat, September sea surface temperature (SST) variance is investigated over interannual timescales using satellite observations from 2000-2017. High resolution, swath SST observations were used to characterize mean September SST lateral variance and investigation into the interannual variability of lateral SST variance is on going.

4.2 Data

4.2.1 In-situ Observations

In-situ observations of the Canada Basin were made 24 August to 26 September 2015 during the ArcticMix cruise (MacKinnon *et al.*, 2016) and 1 to 30 September 2018 during the Stratified Ocean Dynamics of the Arctic (SODA) cruise, both of which were on the R/V *Sikuliaq* (see Figure 4.1 for cruise tracks). The primary goal of the ArcticMix cruise was to observe the turbulent processes controlling the distribution of heat and salt in the Beaufort Sea, while the objective of the SODA cruise was to determine the processes setting stratification in the Beaufort Sea. During both cruises, a suite of in-situ observations were made to resolve temperature, salinity, velocity (u, v), thermal variance dissipation rate (χ_T) and rate of dissipation of kinetic energy (ϵ) in the upper Arctic Ocean (see Figure 4.2 for sample observations).

High-resolution observations of surface mixed layer temperature were made using a bow-mounted chain with fast-response thermistors installed at ~ 1 m spacing and temperature, conductivity, depth (CTD) sensors installed at ~ 5 m spacing over the top 20 m of the water column (Figure 4.2a). The bow-mounted system allows the sensors to pass through undisturbed water, resolving a surface layer uncontaminated by ship wake. The bow chain was towed by the ship at 0.5-2 m/s and temporal

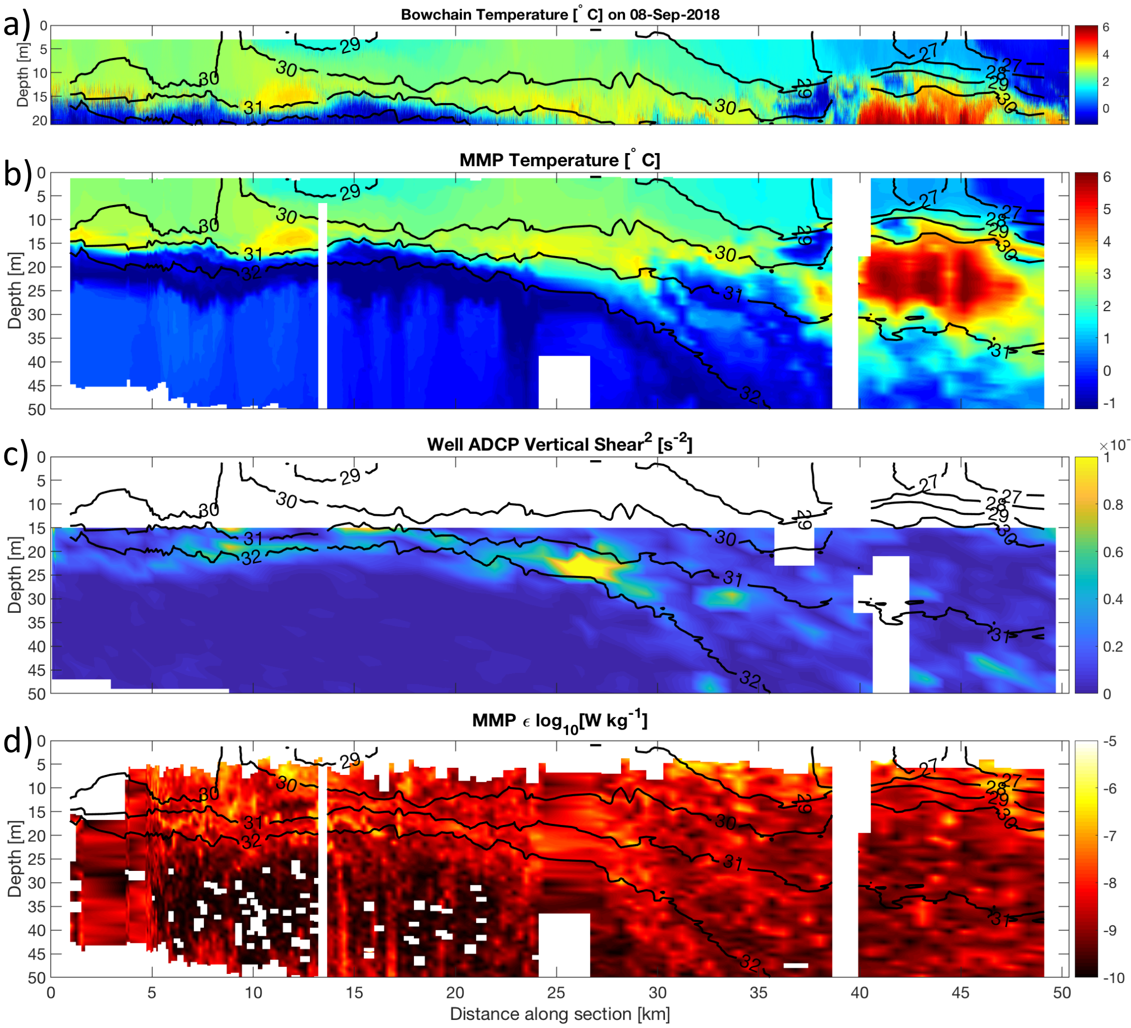

a) Bowchain Temperature [$^{\circ}$ C] on 08-Sep-2018

b) MMP Temperature [$^{\circ}$ C]

c) Well ADCP Vertical Shear^2 [s^{-2}]

d) MMP ϵ log$_{10}$[W kg^{-1}]

Figure 4.2: Sample observations of (a) bow chain temperature [°C], (b) MMP temperature [°C], (c) ADCP squared shear [s^{-2}], and (d) MMP rate of dissipation of kinetic energy, ϵ [log_{10}(W kg^{-1})], for a deployment on September 8, 2108. MMP Salinity [PSU] is contoured in black on all panels. Location of this transect is indicated by the red x in Figure 4.1.

sampling of the different sensors varied from 1-6 Hz, resulting in horizontal resolution $\mathcal{O}(1 \text{ m})$. Pressure observations are linearly interpolated between sensors and all temperature observations are interpolated onto regularly spaced vertical and along-transect distance or time grids. For this study, 4 deployments are analyzed from the ArcticMix cruise and 10 deployments from the SODA cruise. Individual deployments ranged from 10-85 km in length and lasted for 1-30 hrs. An average deployment extended for 40 km and 13 hrs.

For both experiments, χ_T, ϵ, and CTD profiles were made using a Modular Microstructure Profiler (MMP, Wesson & Gregg (1994), Figure 4.2b & d). For the ArcticMix cruise, all MMP profiles were made off the ship's fantail resulting in contamination of the measured fields by the ship's wake over the top 10-20 m of the water column. MMP deployments were moved to a boom on the starboard side of the ship during the SODA cruise, which significantly reduced contamination of the measured fields by ship wake to only the top 4-5 m of the water column. The processing of the MMP observations is discussed in detail by Fine *et al.* (2018). Acoustic Doppler Current Profilers (ADCP) were deployed on both cruises in the ship's well to resolve currents from 10-125 m depth (Figure 4.2c). Unfortunately, ADCP data quality during the ArcticMix cruise was poor, particularly in the top 20 m, due to low scatters in the Beaufort Sea and instrument issues. 300 kHz ADCPs deployed during the SODA cruise were selected and programed to address challenges that arose during the ArcticMix cruise resulting in improved data quality.

4.2.2 Satellite SST

Regional SST and it's seasonal and interannual variability are investigated using daily un-gridded Moderate-resolution Imaging Spectroradiometer (MODIS) Level 2 nighttime swath observations at $\sim$ 1 km horizontal resolution from the National

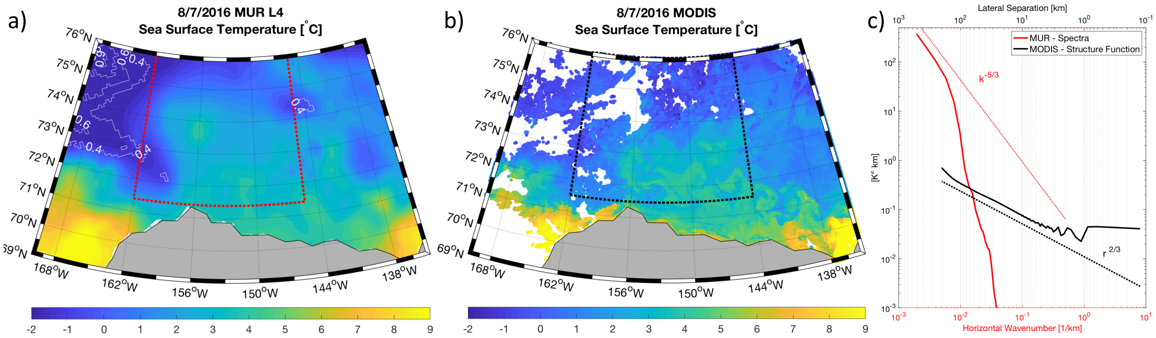

Figure 4.3: Sample observations of SST [°C] on August 7, 2016 from (a) the blended, gridded MUR L4 product and (b) un-gridded MODIS L2P swath observations. (c) The horizontal wavenumber spectra from MUR SST (red line) and structure function from MODIS SST (black line) are calculated over the corresponding boxed regions in panels (a) and (b). Note that the structure function horizontal axis is decreasing in magnitude from left to right for easier comparison with corresponding wavenumbers.

Aeronautics and Space Administration (NASA) Aqua and Terra satellites, each of which image the entire earth every 1-2 days (Figure 4.3b, JPL/OBPG/RSMAS (2016*a*,0)). Satellite SST observations over the Beaufort Sea (71.5°N, 162°W to 76°N, 144°W; Figure 4.1, dotted red box) are investigated during August to October with MODIS SST from 2000-2017. The daily temporal and 1 km spatial resolution make MODIS the preferred dataset for investigations of submesoscale SST structures, however observations of Arctic SST are often obscured by cloud cover, reducing the spatial and temporal coverage. This is demonstrated in Figure 4.3b, where large regions of the study area are not resolved. Uncertainties of ~ 0.1 K are reported for current MODIS SST products (Kilpatrick *et al.*, 2015).

Daily SST observations from the Multi-scale Ultra-high Resolution (MUR) Level 4 blended, gridded product at 0.01° horizontal resolution (Figure 4.3a, JPL MUR MEaSUREs Project (2015)) were also investigated. While MUR L4 SST has significantly better spatial and temporal coverage compared to MODIS swath SST, the blending and griding procedure for the product smooths over temperature variability on scales smaller than 100 km, effectively remove both mesoscale and submesoscale

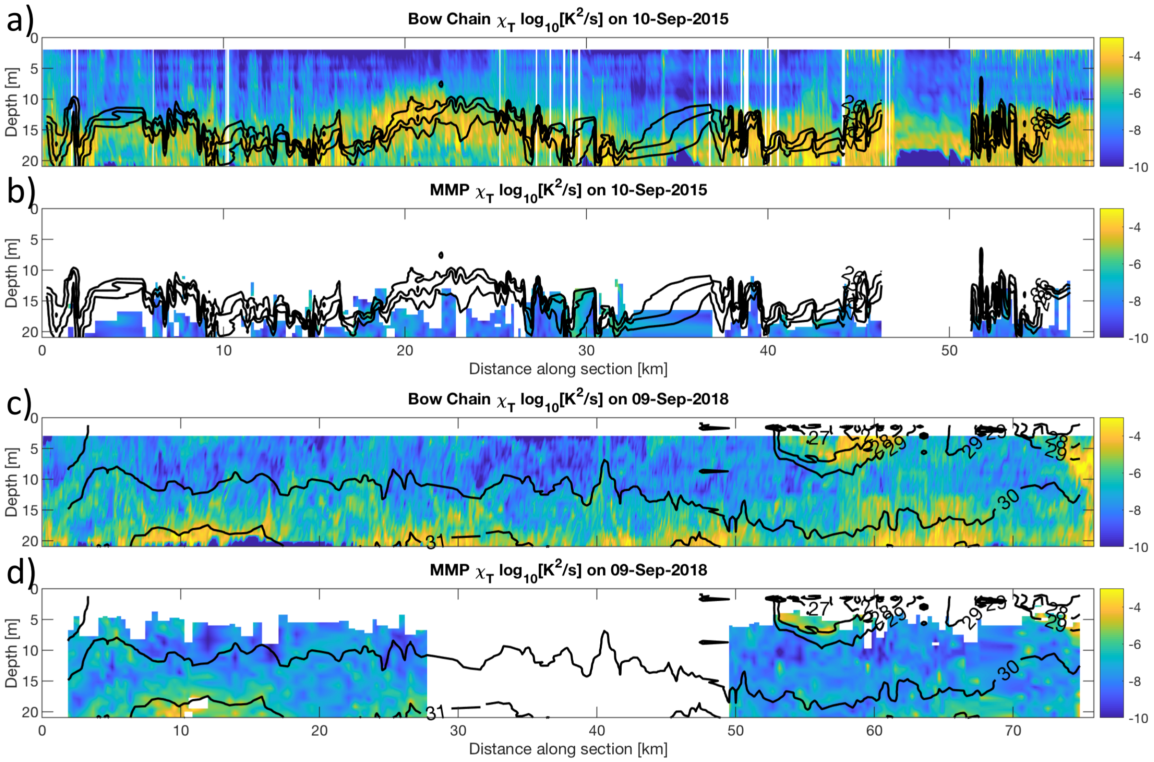

Figure 4.4: Example observations of thermal variance dissipation rate, χ_T $[log_{10}(\mathrm{K}^2\ \mathrm{s}^{-1})]$, estimated from (a,c) bow chain and (b,d) MMP observations during the (a-b) September 8, 2018 and (c-d) September 9, 2018 deployments. MMP salinity observations are contoured in black on all panels.

SST variability (Figure 4.3).

4.3 Methods

4.3.1 Estimating χ_T

Bow chain temperature observations at 1 Hz are used to estimate χ_T following the methods of Moum & Nash (2009) and Zhang & Moum (2010) (Figure 4.4). Time series of temperature along the bow chain are converted into a lateral record of temperature using the estimated flow speed past each sensor and assuming that the timescale of the observations is much smaller compared to the timescale of the dynamics of interest. Flow speed is estimated from the measured ship velocity over ground and ADCP velocity observations. Spectra of the lateral gradient of temperature are fitted to estimate Bachelor spectra and estimate χ_T (Batchelor, 1959). As our observations are made at varying depths due to ship heave, additional work is needed to estimate and remove the fraction of the signal that is due to vertical motions of the sensor through vertical temperature gradients. Ideally, the vertical motion is independently measured by high resolution accelerometers installed on the bow chain alongside the thermistors and CTDs (Zhang & Moum, 2010). However no accelerometers were installed during the ArcticMix and SODA bow chain deployments. The uncontaminated signal is estimated by removing the fraction of the measured signal that is coherent with the temperature gradient spectra induced by the vertical motion of the bow chain through the water column. The vertical motion is estimated from the temporal derivative of pressure observations on the bow chain, which Zhang & Moum (2010) have shown leads to over-estimates of χ_T when compared to independent microstructure observations. An estimate of χ_T at 5 minute intervals is made by fitting the corrected temperature gradient spectra to theoretical spectra over the inertial convective subrange ($0.05 < f < 0.5$ Hz) (Moum & Nash, 2009).

4.3.2 Spectra and Structure Functions

One method of deducing the observed mesoscale and submesoscale field is through the use of horizontal wavenumber spectra. In simplest terms, spectra quantify the contribution of different wavenumbers or frequencies to the variance of the observed quantity. As such, spectra are a tool commonly used to infer how quantities, like energy for example, are distributed over a range of scales. Dimensional arguments have been use to determine theoretical spectral slopes of energy and passive tracers for different dynamical processes (Charney, 1971; Blumen, 1978; Boyd, 1992), and have been widely used in observational oceanography to infer a system's relevant dynamics (Ferrari & Rudnick, 2000; Callies & Ferrari, 2013; Klymak *et al.*, 2015; Kunze *et al.*, 2015; Rocha *et al.*, 2016).

To calculate horizontal wavenumber spectra of temperature, the Fourier transform of segments of temperature (T),

$$\Phi_T(k) = \mathcal{F}\left(\mathbf{T} * W(k)\right), \tag{4.1}$$

which is a function of horizontal wavenumber, k, is taken after removing a linear fit from each segment and then convolving the data with a variance preserving window, $W(k) = w(k)/\sqrt{\frac{\sum w(k)^2}{M}}$, where $w(k)$ is an M-point Hanning window equal in length to the segment of T. The spectra

$$S(k) = \frac{\Delta x}{2\pi M} 2[\Phi_r^2(k) + \Phi_i^2(k)] \tag{4.2}$$

is formed from the real and imaginary Fourier coefficients, where $\Phi(k) = \Phi_r(k) + i\Phi_i(k)$, normalized by $\frac{\Delta x}{2\pi M}$ such that Parseval's theorem is satisfied, where Δx is the lateral grid spacing. Horizontal wavenumber spectra of potential density from bow chain CTD observations are calculated in an identical manner. For in-situ observations all horizontal wavenumber spectra are calculated at 3-6 m depth, which is within the surface mixed layer and the shallowest, common depth resolved during a particular deployment. For regularly gridded satellite observations, the two-dimensional wavenumber spectra are averaged azimuthally into a single wavenumber spectrum (Figure 4.3c, red line).

MOIDS SST swath observations are not uniformly gridded and have large, irregular gaps in the spatial coverage. These issues rule out the method of horizontal wavenumber spectra, which require regularly spaced and continuous observations over the domain. Instead, structure functions are used to quantify the variance of

SST over a range of scales. Classically, Kolmogorov (1941) used both spectra and structure functions to describe the turbulent cascade of kinetic energy from large to small scales, formalizing the power laws in relation to both distances and wavenumbers. Oboukhov (1949) performed an analogous derivation for the temperature field of turbulence in the atmosphere assuming that temperature is a passive tracer. Contemporary use of structure functions for inferring three dimensional turbulence from geophysical observations of temperature has been more common within atmospheric community (Frehlich, 1992; Frehlich & Sharman, 2004). However, recent work by Renosh *et al.* (2015) used structure functions of MODIS SST characterize the variance of temperature and test a less computationally demanding scaling method. To the best of our knowledge, this is the only other published work on MODIS SST observations at this time.

The structure function,

$$D(r) = \frac{r}{2\pi M(r)} \Sigma_{i=1}^{M(r)} 2([T(x+r) - T(x)]^2) \tag{4.3}$$

is constructed from observations of temperature differences separated by a distance, r. Differences are binned over regularly spaced r at 0.25 km spacing and $M(r)$ is the number of pairs of observations within each r bin. Error is assessed for each bin assuming a chi-square distribution which is a function of $M(r)$. For this work, temperature structure functions are normalized to have the same units as horizontal wavenumber spectra with the intention of comparing the two quantities (Figure 4.3c, black line). For MODIS observations, SST differences are only calculated over individual nights to limit temporal aliasing and overlapping satellite passes allow for horizontal resolution which is smaller than 1 km. Structure functions are computationally expensive. For a MODIS swath with n observations over the study region, $\frac{1}{2}n(n-1)$ differences are required to evaluate the structure function for that swath, though Renosh *et al.* (2015) find that structure function statistics converge by 10^6 differences for their study region.

The structure function for a passive tracer in fully developed turbulence has a power law of $r^{2/3}$, which is analogous to a power spectrum of the passive tracer with a power law of $k^{-5/3}$ (Oboukhov, 1949). Because structure functions are computationally expensive, particularly compared to spectral analysis, analogous power relationship have not been developed for structure functions for quasi-geostrophic or other dynamics. Nonetheless, temperature structure functions still quantify the distribution of temperature variance as a function of horizontal length scale. This facilitates inter-comparisons of a temporally evolving SST field where the relative changes in the magnitude and power law of the structure functions indicate changes in the variance of temperature and it's distribution across a range of length scales.

As surface dynamics are expected to differ over the range of observed lateral scales, two wavenumber bounds are defined and calculated for each deployment which may help to separate these dynamical regimes in wavenumber space. The first is a surface-layer Rossby wavenumber, $k_{Rossby} = [NH/f]^{-1}$, where N is the mean surface layer buoyancy frequency over the deployment, H is the depth of the surface layer, and f is the local Coriolis frequency. Here H is the depth where density is 0.5 kg m^{-3} greater than the shallowest observed density, typically at 2-5 m depth. This wavenumber is simply the inverse of the internal Rossby radius in the surface layer and a relevant length scale for surface mixed layer submesoscale dynamics (Boccaletti *et al.*, 2007). The second is a mixed layer wavenumber, $k_{MLD} = 1/H$, which is the inverse of the surface mixed layer depth. Motions with horizontal scales equal to or smaller than the mixed layer depth will have aspect ratios of $\mathcal{O}(1)$ and are governed by different dynamics.

To ensure no overlap in wavenumber space of temperature spectra used to quantify variance at $k > k_{Rossby}$ and temperature observations used to estimate χ_T, an additional wavenumber limit, $k_{ship} \equiv f_{IC}/|3\overline{U_{ship}}|$ is defined, where $f_{IC} = 0.05$ Hz is the lower integration limit used to estimate χ_T and $|\overline{U_{ship}}|$ is the mean ship speed over a deployment. An additional factor of 3 is included to account for the variability of the ship speed over a deployment period.

4.4 Results

4.4.1 Bow Chain Temperature Spectra

While temperature is thermodynamically relevant in the Arctic, density is salinity controlled and temperature is nearly a passive tracer (Timmermans & Jayne, 2016). On average temperature contributes only about 10% of the lateral density variability observed by bow chain CTDs within the the surface mixed layer. Nonetheless, it is desirable to work with temperature as SST has been measured continuously for nearly two decades by MODIS sensors on the NASA satellites Aqua and Terra. Thus horizontal wavenumber spectra of temperature and density from bow chain CTD observations at 3-6 m depth are compared.

Two sets of example spectra, both at 5 m depth, are shown in Figure 4.5a, with one set from the ArcticMix cruise (2015, blue lines) and one from the SODA cruise (2018, red lines). Horizontal wavenumber spectra from bow chain CTD observations exhibit power laws ranging from k^{-3} to k^{-1} for wavenumbers less than k_{Rossby}, with most observations exhibiting k^{-2} behavior (Figure 4.5a & b). For wavenumbers larger than k_{Rossby}, spectra flatten, shifting toward a power law of k^{-1} though this portion of the wavenumber spectra is observed to have power laws ranging from k^{-3} to k^{0} (Figure 4.5a & d).

For both density and passive tracers, spectra that exhibit a power law of k^{-2},

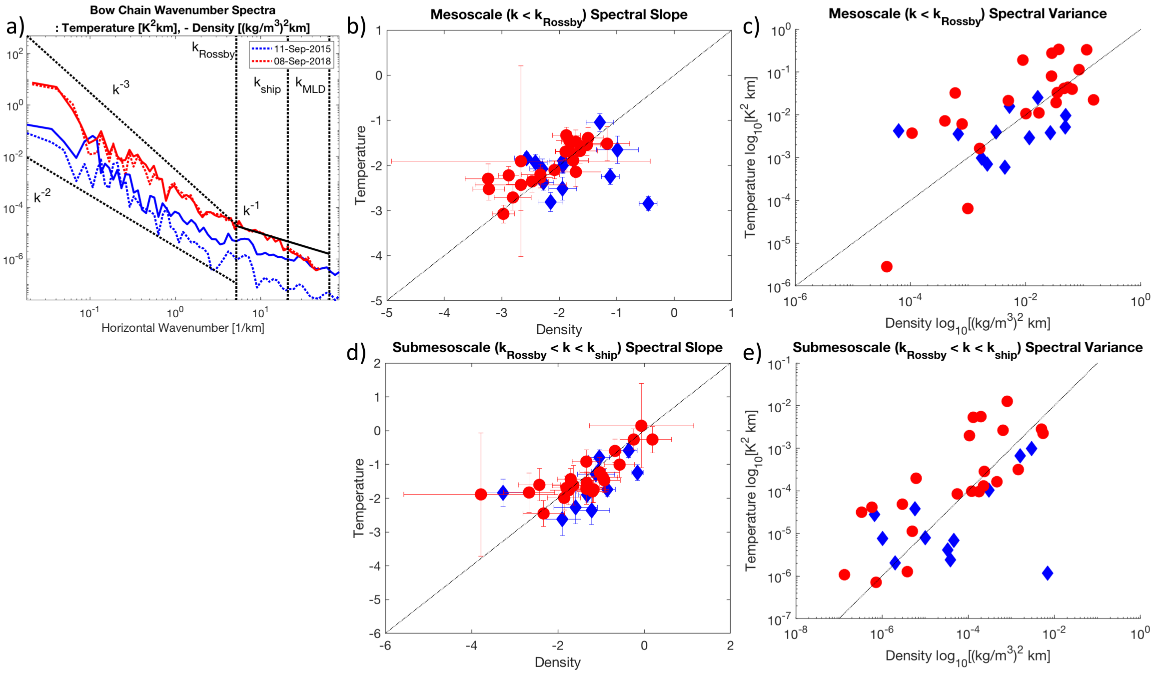

Figure 4.5: (a) Sample bow chain temperature (dotted lines) and density (solid lines) horizontal wavenumber spectra from September 11, 2015 on the ArcticMix cruise (blue lines) and September 8, 2018 on the SODA cruise (red lines). The locations of k_{Rossby}, k_{ship}, and k_{MLD} averaged over the two cruises are denoted with vertical dotted black lines, though all three vary between deployments. Wavenumber slopes of -2, -3, and -1 are given for reference. (b) Spectral slope estimated from a linear fit for wavenumbers $k < k_{Rossby}$ for density compared to temperature spectra. Error bars are the 95% confidence bounds for the linear fits to the spectra. (c) Variance of density compared to temperature horizontal wavenumber spectra, integrated over wavenumbers $k < k_{Rossby}$. (d) Spectral slope estimated from a linear fit for wavenumbers $k_{Rossby} < k < k_{ship}$ for density compared to temperature spectra. Error bars are the 95% confidence bounds for the linear fits to the spectra. (e) Variance of density compared to temperature horizontal wavenumber spectra, integrated over wavenumbers $k_{Rossby} < k < k_{ship}$. (b-e) Observations from ArcticMix/September 2015 are indicated by blue diamonds while those from SODA/September 2018 are indicated by red circles.

or a wavenumber slope of -2 in log-log space, are suggestive of a dynamical field with significant ageostrophic motions that result in strong fronts in density, passive tracers, and the lateral velocity field (Boyd, 1992). Quasi-geostrophic flows exhibit steeper slopes of -3 for density wavenumber spectra (Charney, 1971), though passive tracers stirred by quasi-geostrophic motions are predicted to exhibit slopes of -1. However, theory predicts that such interior quasi-geostrophic dynamics are modified at the ocean surface resulting in spectra for density and tracers that are flatter compared to interior quasi-geostrophic dynamics with slops of $-5/3$ (Blumen, 1978).

The spectral variance of temperature and density are also compared, though these quantities do have different units (Figure 4.5c & e). For both wavenumber ranges ($k < k_{Rossby}$ & $k > k_{Rossby}$), variance from temperature and density spectra are observed to have positive relationships indicating that when temperature variance is relatively enhanced, variance of potential density is also elevated. In other words, stronger or more energetic lateral gradients in temperature also indicate enhanced and more energetic lateral gradients in buoyancy, for both meso- and submesoscales in the Beaufort Sea.

4.4.2 Bow Chain χ_T

Estimates of χ_T from bow chain observations are compared with independent and collocated estimates from MMP observations above the mixed layer depth from the ArcticMix and SODA cruises (Figures 4.4 and 4.6). Qualitatively, χ_T from both MMP and bow chain observations are enhanced at the base of the mixed layer and along sloping isohalines within the mixed layer (Figure 4.4). When MMP observations extend up to 5-10 m depth, the two estimates observe similar patterns of χ_T, though the bow chain estimate is clearly biased high along the base of the mixed layer, where vertical temperature gradients are strongest and result in stronger contamination of

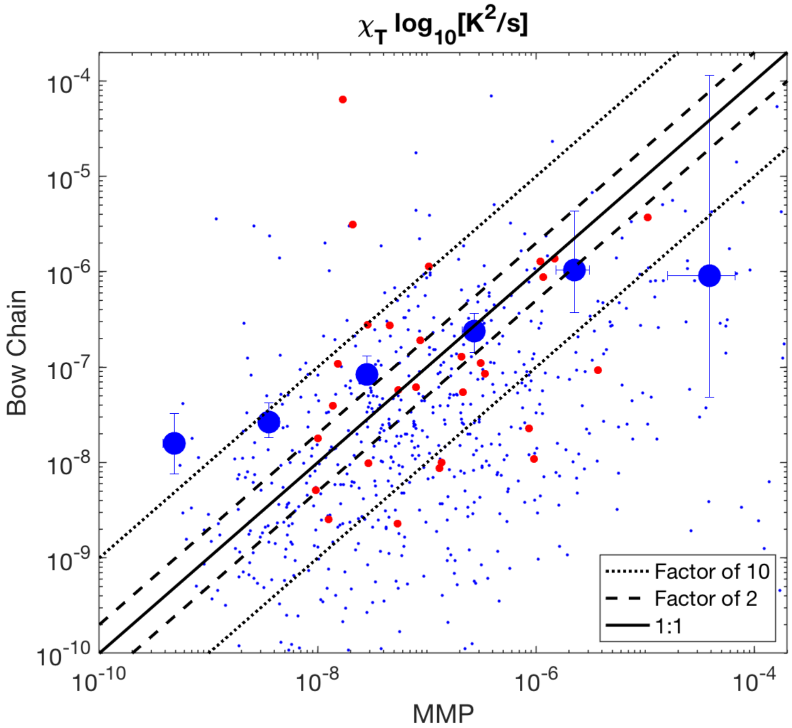

Figure 4.6: Comparison of collocated observations of χ_T from MMP and bow chain observations bin-averaged over decades of MMP χ_T for all depths above the mixed layer depth (blue circles). Error bars indicate the 95% bootstrap confidence intervals for each mean. Red circles indicate individual collocated observations of MMP and bow chain χ_T at 5 m depth while blue dots indicated all collocated observations above the surface mixed layer depth. Black lines indicating a 1:1 agreement (solid), agreement within a factor of 2 (dashed), and agreement within a factor of 10 (dotted) are shown.

the signal due to ship heave. It is evident that at these depths the method does not entirely remove this ship heave contamination from the horizontal temperature gradient spectra without independent accelerometer observations. However away from the mixed layer depth, the bow chain estimate does appear to observe the same patterns of χ_T as observed by the MMP and even reasonably estimates the magnitude.

A more quantitative comparison of χ_T from MMP and bow chain observations is given in Figure 4.6, where individual, collocated estimates of χ_T at least 3 m above the mixed layer depth for both system are shown as small blue dots. The median of MMP χ_T binned over decades and the median of the collocated estimates from bow chain temperature are represented by large blue circles with error bars indicating the 95% bootstrap confidence intervals. A positive relationship is found between estimates of χ_T from bow chain and MMP observations, though a weaker relationship than a 1:1 ratio. Bow chain observations generally over-estimate χ_T over the lower range of χ_T observed by the MMP and underestimate χ_T over the upper range observed by the MMP. Agreement between the two systems is improved when only considering observations at 5 m depth (Figure 4.6, red circles), with most observations falling within a factor of 10 agreement, though there remains significant spread even at that depth.

4.4.3 Mixed Layer χ_T and Surface Mixed Layer Spectra

Horizontal wavenumber spectra for 30 km segments of bow chain observations at 3-6 m depth are calculated for all deployments. A segment length of 30 km was chosen to include shorter deployments but also to achieve some overlap in wavenumber space between in-situ and satellite observations. To estimate the variance contained in the submesoscales, spectra are integrated from k_{Rossby} to k_{ship}, allowing the wavenumber range to vary for each deployment, and normalized by the wavenumber

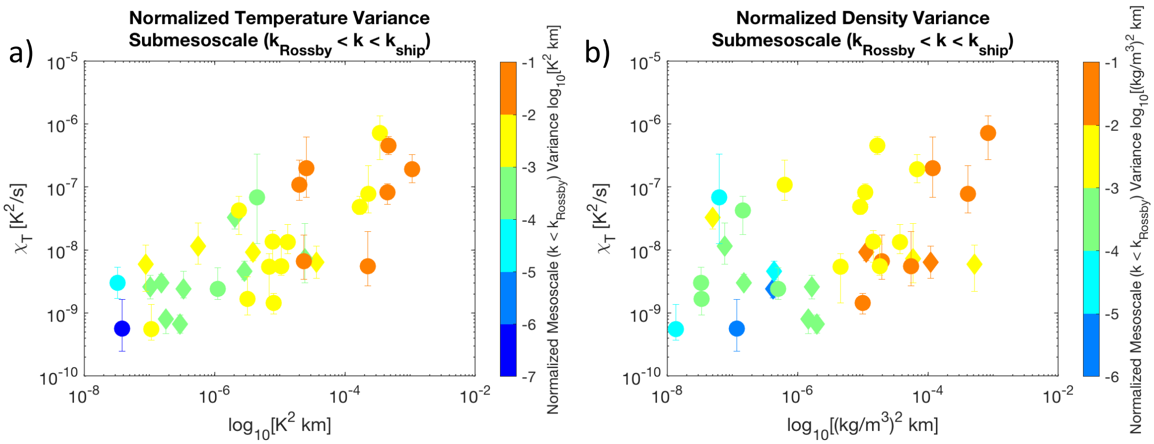

Figure 4.7: Variance for (a) temperature and (b) density horizontal wavenumber spectra at 3-6 m depth integrated over and normalized by the wavenumber range $k_{Rossby} < k < k_{ship}$ compared to segment-mean χ_T from the same depth. Observations are also colored by the normalized spectral variance for $k < k_{Rossby}$. Vertical error bars give the 95% bootstrap confidence intervals for each segment. Observations from September 2015 are indicated by diamonds while those from September 2018 are indicated by circles.

integration range. For the same segments and depth, median χ_T is estimated and 95% bootstrap confidence levels are used to assess errors. A relationship is found between median bow chain χ_T and the normalized variance in both temperature and density for $k_{Rossby} < k < k_{ship}$ (Figure 4.7). A secondary relationship between normalized variance at meso- ($k < k_{Rossby}$) and submesoscales ($k > k_{Rossby}$) is also noted though there is not a strong relationship between mesoscale temperature variance and χ_T.

4.4.4 Annual and Interannual SST Variability

Daily temperature differences calculated from all years of MODIS SST are combined into mean structure functions for two-week windows beginning in August and going through October (Figure 4.8a). Structure functions are only considered for $r > 3$ km as instrument artifacts are observed for smaller scales, potentially related to instrument issues discussed in Kilpatrick *et al.* (2015). Assuming a chi-square distribution, 95% confidence intervals are calculated for each two-week average and shown

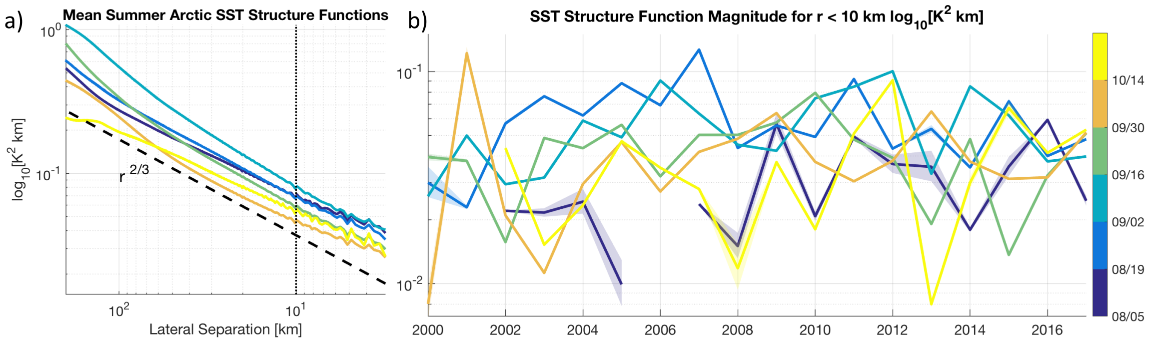

Figure 4.8: (a) Mean weekly September structure functions from MODIS 2000-2017 observations. The location of $r = 10$ km is denoted with vertical dotted line. (b) The magnitude of the weekly September SST structure functions for $r < 10$ km from 2000 to 2017. Error bounds in both panels are the 95% confidence intervals assuming a chi-square distribution for the structure functions.

as shading around each line in Figure 4.8a, however error bars are indistinguishable from the lines due to the number of realizations. Temperature structure functions have moderate magnitude in early August and increasing into the first half of September, particularly at the largest scales. By the second half of September, variance is uniformly reduced at all scales, relative to the first half of September. SST variance continues to decrease through October with the largest reductions in variance at the largest scales.

A preliminary analysis of interannual changes in SST variance using the two-week averages of SST structure function magnitude for $r > 10$ km is shown in Figure 4.8b. SST variance is relatively steady from year-to-year for the last two weeks in August and the month of September, but is more variable at the beginning of August and during October. Additional work is need to further investigate this temporal variability, including efforts to extend this analysis down to ¡ 1 km resolution, making use of the overlapping swath observations in a single nighttime.

4.5 Discussion

High resolution in-situ observations of the Beaufort Sea surface mixed layer were made in September 2015 and 2018, resolving a rich field of fronts and filaments in the top 20 m of the water column (Figure 4.2). Horizontal wavenumber spectra of temperature and density generally capture similar wavenumber spectra, particularly over submesoscales (Figure 4.5). Estimates of χ_T from bow chain observations capture the independently resolved patterns observed by MMP observations (Figure 4.4) and even reasonably approximate the same magnitude of χ_T at 5 m depth, away from the mixed layer (Figure 4.6). A relationship is found between in-situ submesoscale temperature variance and χ_T over 3-6 m depth in the surface mixed layer, with a weaker relationship between mesoscale variance and χ_T (Figure 4.7). Finally, MODIS SST observations from 2000-2017 are analyzed using structure functions to quantify mean and interannual variability of summer submesoscale SST variance (Figure 4.8). On average, submesoscale SST variance increases during August, reaches a maximum in early September and then decreases through the end of October.

These results inform the hypothesis that enhanced variance of temperature, and also buoyancy, results in enhanced dissipation of thermal variance and thus vertical heat fluxes in the surface mixed layer in the Beaufort Sea. These observations indicate that over the submesoscale range, enhanced lateral variance of surface mixed layer temperature is also indicative of a relative increase in surface mixed layer buoyancy variance. A surface mixed layer with increased spectral variance corresponds to a surface mixed layer with relatively enhanced lateral gradients, in this case for both temperature and buoyancy. Frontogenesis is one mechanism for which enhanced lateral buoyancy gradients drive strong vertical velocities and may be responsible for some of the enhanced χ_T observed in this study (Mahadevan & Tandon, 2006; Thomas *et al.*, 2008). Frontogenesis arises from lateral buoyancy gradients which sharpen due to nonlinear interactions. As the front strains, a secondary ageostrophic circulation results in localized regions of large vertical velocities. Frontogenesis can drive strong subduction over a narrow region on the less buoyant side of the front but also results in increased shear from the ageostrophic circulation at the front itself. The importance of frontogenesis for the Beaufort Sea will depend upon the strength and distribution of buoyancy fronts within the basin.

Satellite SST observations indicate a seasonally varying surface mixed layer in the Beaufort Sea. The observed pattern in SST variance may reflect the seasonal shift in surface buoyancy forcing (Carmack *et al.*, 2015). During the period of net heat gain in the Arctic before mid-September, buoyancy sources of fresh water originate at the boundaries and are heterogeneously input within the Beaufort Sea from melting sea ice flows. These sources inherently create lateral density gradients of varying temperature which can be stirred by the mesoscale eddy field before filamenting and forming a rich submesoscale field. However in autumn and winter, surface heat loss to the atmosphere results in sea ice formation and a homogenization and deepening of the surface mixed layer due to convective mixing. As the spatial scales of autumn and wintertime buoyancy loss are dictated by the atmosphere and are on the scale of the Beaufort Sea, this buoyancy loss is a mechanism to destroy SST variance.

4.6 Ongoing Work

Additional work is planned to improve our understanding of the connections between structure functions and horizontal wavenumber spectra. Structure function calculation are currently underway to resolve the temperature and density structure functions of bow chain observations. The calculation is being done over the same depths used for the horizontal wavenumber spectra to allow one-to-one comparisons of the resulting power laws from the two methods. We expect that these results may be useful in further interpreting the observed power laws for satellite SST structure functions.

Additional work is also required to extend the SST structure function calculation to submesoscales $\mathcal{O}(1)$ km. Artifacts are observed in the lateral gradients at scales less than 3 km. Discussion with NASA scientist are being initiated to fully understand the sources of these biases. The ultimate goal is to use over lapping MODIS swath observations within a single night to estimate submesoscale SST variance on scales smaller than 1 km. Our approach will likely depend on the particulars of the source of this SST bias at these small scales.

Acknowledgements

Bow chain processing code for MATLAB is freely available at https://github.com/dswinters/BowChain. The Group for High Resolution Sea Surface Temperature (GHRSST) Multi-scale Ultra-high Resolution (MUR) SST data were obtained from the NASA EOSDIS Physical Oceanography Distributed Active Archive Center (PO.DAAC) at the Jet Propulsion Laboratory, Pasadena, CA (http://dx.doi.org/10.5067/GHGMR-4FJ01). We would like to thank Seth Danielson sharing his ADCP for the SODA cruise.

Chapter Four is currently being prepared for submission for publication of the material. Alberty, M. S., MacKinnon, J., Sprintall, J., Alford, M., Mickett, J., and Fine, E. The dissertation author was the primary investigator and author of this paper.

Chapter 5

Conclusions

5.1 Solomon Sea Mixing

Observations from the Solomon Sea indicate a highly dynamic region for both mixing and transport. Indirect observations find strong dissipation of kinetic energy in the thermocline, decreasing by 2-3 orders of magnitude by 2000 m depth. Eddy diffusivity is more uniform over the water column and in good agreement with estimates from a simple advective-diffusive model. Dissipation also varies by 2-3 orders of magnitude along isopycnal layers and is well correlated with tides and topographic roughness for deep and intermediate layers. Shipboard observations indicate seasonal variability of thermocline mixing, which may complicate mean spatial patterns of mixing in the Solomon Sea. These are the first estimates of this kind for the region and lend credit to the hypothesis that vertical mixing is important for modifying water properties in the Solomon Sea.

These results do raise new questions and may be helpful in guiding further work in the region. The spatial patterns of mixing in the thermocline do not clearly indicate a single dominant process for water mass modification. Given the range of processes that occur in the upper ocean, the strength and variability of mixing in the thermocline may be tied to a combination of processes. The following are some of the potentially important processes for thermocline mixing and work which may be pursued to determine the relative importance of these processes in the Solomon Sea.

- **Shear instability** As critical Richardson numbers are observed in profiles with large overturns in density, shear instability presents itself as a potentially important mechanism for turbulence in this region of strongly sheared low latitude western boundary currents. A set of numerical simulations may present the best approach for understanding the necessary conditions in the Solomon Sea for generating shear instabilities. This would be particularly helpful before any future field campaign is proposed to investigate the importance of shear instabilities for thermocline mixing. If observing such features is the object of the study, simulations could be used to determine the locations where these features are most likely to develop and the time of year and phase of the tide for which shear instabilities are most likely.

- **Internal Wave-Eddy Interactions** As has been mentioned, there is evidence of temporally variable mixing in the thermocline, particularly from shipboard observations of density overturns. A fraction of this temporal variability may be related to interactions between the temporally and spatially varying mesoscale eddy field and wind-driven near-inertial waves (Whalen *et al.*, 2018). The existing moored ADCP observations in the Solomon Strait may present a first tool for characterizing the temporal variability of near-inertial shear in the Solomon Sea and specifically how it varies in relation to local eddy kinetic energy which can be estimated from satellite altimetry observations. Further observational or numerical studies could be developed based on those results.

- **Submesoscale Instabilities** Recent work by Srinivasan *et al.* (2017) indicate interactions between the currents and topography in the Solomon Sea may lead to the generation of submesoscale instabilities along the boundaries of the Solomon Sea, resulting in enhanced thermocline mixing and vertical fluxes in theses areas. Their work has identified the regions of the Solomon Sea and the seasons where this mechanism may be important, thus providing critical information for planning future process studies in the Solomon Sea. An observational process study could be designed based on the work by Srinivasan *et al.* (2017) to observe the development of these topographic instabilities and measure the resulting heat and buoyancy fluxes across the thermocline.

5.2 Solomon Sea Transport

Solomon Sea mean transport is observed to primarily pass through Vitiaz Strait, though a larger fraction of thermocline transport than previously estimated is observed to pass through Solomon Strait. While transport variability is relatively weak in Vitiaz Strait, Solomon Strait is observed to have significant temporal variability, particularly at intraseasonal timescales. Only a small fraction of total transport passes through St. George's Channel, although intermediate transport is observed to reverse on seasonal time scales. Prior simulations of transport through St. George's Channel have not noted this observed reversal of intermediate transport. Such simulations are being used to determine the potential transport and dispersion of deep plumes for planned mining operations and our results suggest that such simulations may incorrectly project the plume transport near St. George's Channel. These observations are the first simultaneous transport observations from all three channels and now provide a long-awaited ground truth for regional and global models of ocean circulation and climate. An inter-comparison of mooring observations with existing regional models such as has been described in Grenier *et al.* (2011), Djath *et al.* (2014), Qin *et al.* (2016), or Srinivasan *et al.* (2017) is highly recommended, particularly to understand the sensitivity of EUC water properties in relation to Solomon Strait thermocline transport variability. Such a study could also present an opportunity to compare parameterized patterns of diapycnal diffusivity with estimates from Chapter 2.

Due to the uncertainties in transport estimates as a result of unresolved surface currents and cross-channel current structure, further work is needed to improve and constrain transport estimates. A valuable first step will be an inter-comparison of transport estimates from moored observations with observing systems which simultaneously observed Solomon Sea transport but at the southern boundary. These complimentary observations were made by gliders (Davis *et al.*, 2012) and a system of dynamic height moorings and bottom pressure sensors (*Anutaliya et al. in prep*). Comparing the observations from the three different systems will likely help to constrain the different estimates and improve our understanding of each system's strengths and weaknesses. Such a study will be instrumental in designing future observing systems in the Solomon Sea, which TPOS 2020 has prioritized as a key part of the tropical Pacific observational network (Cravatte *et al.*, 2016).

5.3 Arctic Mixed Layers

Temperature fronts and filaments are observed over a range of scales in the surface mixed layer of the Beaufort Sea in both in-situ and satellite observations. High resolution bow chain observations are used to estimate spatial variability of the dissipation of thermal variance and compared with temperature variance over submesoscale horizontal wavenumbers. Increased submesoscale temperature variance is positively correlated with increased dissipation of thermal variance, suggesting that a more energetic submesoscale field results in enhanced dissipation within the surface mixed layer. Satellite observations also indicate that the submesoscale temperature field is energetic in August and early September but loses energy as September progresses. The results from in-situ observations lead to the hypothesis that seasonal variability of submesoscale variance will result in seasonally varying vertical heat fluxes in the surface mixed layer. The mechanism for this energy transfer from submesoscales down to dissipative scales remains an open question and the focus of work planned for the author's post-doctoral fellowship. The author proposes to use a high resolution process-scale simulation of the Beaufort Sea surface mixed layer to determine the processes which result in the downscale transfer of energy for the Arctic.

These results also lead to the question: what is the influence of seasonally varying mixed layer heat fluxes on sea ice formation during the seasonal refreeze? This question may be addressed by parameterizing the effects of submesoscale dynamics on mixed layer heat fluxes and implementing the parameterization in a global climate model. Preliminary analysis will be needed to determine if the chosen model replicates the seasonal variability of mesoscale SST as observed by satellites and to characterize upper ocean dynamics in the control run. The response of sea ice to the mixed layer parameterization may help to quantify the importance of such upper ocean processes for simulating sea ice retreat over the satellite era. This work will also be pursued during the author's post-doctoral fellowship.

References

Alberty, Marion S, Germineaud, Cyril, Sprintall, Janet, Ganachaud, Alexandre & Cravatte, Sophie 2017 Spice mooring data report: Description and quality control. *Tech. Rep.*. UC San Diego: Scripps Institution of Oceanography, Retrieved from https://escholarship.org/uc/item/6xd149s8.

Alford, Matthew H 2001 Internal swell generation: The spatial distribution of energy flux from the wind to mixed layer near-inertial motions. *Journal of Physical Oceanography* **31** (8), 2359–2368.

Alford, Matthew H 2003*a* Improved global maps and 54-year history of wind-work on ocean inertial motions. *Geophysical Research Letters* **30** (8).

Alford, Matthew H 2003*b* Redistribution of energy available for ocean mixing by long-range propagation of internal waves. *Nature* **423** (6936), 159–162.

Alford, Matthew H, MacKinnon, Jennifer A, Nash, Jonathan D, Simmons, Harper, Pickering, Andy, Klymak, Jody M, Pinkel, Robert, Sun, Oliver, Rainville, Luc, Musgrave, Ruth & others 2011 Energy flux and dissipation in Luzon Strait: Two tales of two ridges. *Journal of Physical Oceanography* **41** (11), 2211–2222.

Alford, Matthew H, Peacock, Thomas, MacKinnon, Jennifer A, Nash, Jonathan D, Buijsman, Maarten C, Centuroni, Luca R, Chao, Shenn-Yu, Chang, Ming-Huei, Farmer, David M, Fringer, Oliver B & others 2015 The formation and fate of internal waves in the South China Sea. *Nature* **521** (7550), 65–69.

Alford, Matthew H & Whitmont, Maya 2007 Seasonal and spatial variability of near-inertial kinetic energy from historical moored velocity records. *Journal of Physical Oceanography* **37** (8), 2022–2037.

Amante, Christopher & Eakins, Barry W 2009 *ETOPO1 1 arc-minute global relief model: procedures, data sources and analysis*. US Department of Commerce, National Oceanic and Atmospheric Administration, National Environmental Satellite, Data, and Information Service, National Geophysical Data Center, Marine Geology and Geophysics Division Colorado.

Atlas, Robert, Hoffman, Ross N, Ardizzone, Joseph, Leidner, S Mark, Jusem, Juan Carlos, Smith, Deborah K & Gombos, Daniel 2011 A cross-calibrated, multiplatform ocean surface wind velocity product for meteorological and oceanographic applications. *Bulletin of the American Meteorological Society* **92** (2), 157–174.

Batchelor, George K 1959 Small-scale variation of convected quantities like temperature in turbulent fluid part 1. general discussion and the case of small conductivity. *Journal of Fluid Mechanics* **5** (1), 113–133.

Blumen, William 1978 Uniform potential vorticity flow: Part I. Theory of wave interactions and two-dimensional turbulence. *Journal of the Atmospheric Sciences* **35** (5), 774–783.

Boccaletti, Giulio, Ferrari, Raffaele & Fox-Kemper, Baylor 2007 Mixed layer instabilities and restratification. *Journal of Physical Oceanography* **37** (9), 2228–2250.

Boyd, John P 1992 The Energy Spectrum of Fronts: Time Evolution of Shocks in Burgers Equation. *Journal of the Atmospheric Sciences* **49** (2), 128–139.

de Boyer Montégut, Clément, Madec, Gurvan, Fischer, Albert S, Lazar, Alban & Iudicone, Daniele 2004 Mixed layer depth over the global ocean: An examination of profile data and a profile-based climatology. *Journal of Geophysical Research: Oceans* **109** (C12).

Butt, Jeff & Lindstrom, Eric 1994 Currents off the east coast of New Ireland, Papua New Guinea, and their relevance to regional undercurrents in the western equatorial Pacific Ocean. *Journal of Geophysical Research: Oceans* **99** (C6), 12503–12514.

Callies, Jörn & Ferrari, Raffaele 2013 Interpreting energy and tracer spectra of upper-ocean turbulence in the submesoscale range (1–200 km). *Journal of Physical Oceanography* **43** (11), 2456–2474.

Capet, Xavier, McWilliams, JAMES C, Molemaker, M JEROEN & Shchepetkin, AF 2008 Mesoscale to submesoscale transition in the California Current System. Part I: Flow structure, eddy flux, and observational tests. *Journal of physical oceanography* **38** (1), 29–43.

Carmack, Eddy, Polyakov, I, Padman, Laurie, Fer, Ilker, Hunke, E, Hutchings, Jennifer, Jackson, Jennifer, Kelley, D, Kwok, Ronald, Layton, Chantelle & others 2015 Toward quantifying the increasing role of oceanic heat in sea ice loss in the new Arctic. *Bulletin of the American Meteorological Society* **96** (12), 2079–2105.

Carmack, Edward C, Yamamoto-Kawai, Michiyo, Haine, Thomas WN, Bacon, Sheldon, Bluhm, Bodil A, Lique, Camille, Melling, Humfrey, Polyakov, Igor V, Straneo, Fiamma, Timmermans, M-L & others 2016 Freshwater and its role in the Arctic Marine System: Sources, disposition, storage, export, and physical and biogeochemical consequences in the Arctic and global oceans. *Journal of Geophysical Research: Biogeosciences* **121** (3), 675–717.

Charney, Jule G 1971 Geostrophic turbulence. *Journal of the Atmospheric Sciences* **28** (6), 1087–1095.

Coulin, Jade, Haley, PJ, Jana, Sudip, Kulkarni, Chinmay S, Lermusiaux, Pierre FJ & Peacock, Thomas 2017 Environmental ocean and plume modeling for deep sea mining in the Bismarck Sea. In *OCEANS-Anchorage, 2017*, pp. 1–10. IEEE.

Cravatte, Sophie, Ganachaud, Alexandre, Duong, Quoc-Phi, Kessler, William S, Eldin, Gérard & Dutrieux, Pierre 2011 Observed circulation in the Solomon Sea from SADCP data. *Progress in Oceanography* **88** (1), 116–130.

Cravatte, Sophie, Kessler, William, Smith, Neville, Wijffels, Susan & Contributing Authors 2016 First Report of TPOS 2020. *Tech. Rep.* GOOS-215.

Cravatte, Sophie, Kessler, William S & Marin, Frédéric 2012 Intermediate zonal jets in the tropical Pacific Ocean observed by Argo floats. *Journal of Physical Oceanography* **42** (9), 1475–1485.

Cravatte, Sophie, Kestenare, Elodie, Marin, Frédéric, Dutrieux, Pierre & Firing, Eric 2017 Subthermocline and intermediate zonal currents in the tropical Pacific Ocean: paths and vertical structure. *Journal of Physical Oceanography* **47** (9), 2305–2324.

D'asaro, Eric, Lee, Craig, Rainville, Luc, Thomas, Leif & Harcourt, Ramsey 2011 Enhanced turbulence and energy dissipation at ocean fronts. *science* p. 1201515.

Davis, Russ E, Kessler, William S & Sherman, Jeffrey T 2012 Gliders Measure Western Boundary Current Transport from the South Pacific to the Equator*. *Journal of Physical Oceanography* **42** (11), 2001–2013.

Delcroix, Thierry, Radenac, Marie-Hélène, Cravatte, Sophie, Alory, Gaël, Gourdeau, Lionel, Léger, Fabien, Singh, Awnesh & Varillon, David 2014 Sea surface temperature and salinity seasonal changes in the western Solomon and Bismarck Seas. *Journal of Geophysical Research: Oceans* **119** (4), 2642–2657.

Dillon, TM 1982 Vertical overturns: A comparison of Thorpe and Ozmidov length scales. *J. Geophys. Res* **87** (C12), 9601–9613.

Djath, Bughsin', Verron, Jacques, Melet, Angelique, Gourdeau, Lionel, Barnier, Bernard & Molines, Jean-Marc 2014 Multiscale dynamical analysis of a high-resolution numerical model simulation of the Solomon Sea circulation. *Journal of Geophysical Research: Oceans* **119** (9), 6286–6304.

Egbert, GD & Ray, RD 2000 Significant dissipation of tidal energy in the deep ocean inferred from satellite altimeter data. *Nature* **405** (6788), 775–778.

Egbert, Gary D & Erofeeva, Svetlana Y 2002 Efficient inverse modeling of barotropic ocean tides. *Journal of Atmospheric and Oceanic Technology* **19** (2), 183–204.

Ferrari, Raffaele & Rudnick, Daniel L 2000 Thermohaline variability in the upper ocean. *Journal of Geophysical Research: Oceans* **105** (C7), 16857–16883.

Fine, Elizabeth C, MacKinnon, Jennifer A, Alford, Matthew H & Mickett, John B 2018 Microstructure observations of turbulent heat fluxes in a warm-core Canada Basin eddy. *Journal of Physical Oceanography* (2018).

Fine, Rana A, Lukas, Roger, Bingham, Frederick M, Warner, Mark J & Gammon, Richard H 1994 The western equatorial Pacific: A water mass crossroads. *Journal of Geophysical Research: Oceans (1978–2012)* **99** (C12), 25063–25080.

Flato, Gregory, Marotzke, Jochem, Abiodun, Babatunde, Braconnot, Pascale, Chou, S Chan, Collins, William, Cox, Peter, Driouech, F, Emori, S, Eyring, V & others 2013 Evaluation of climate models.

Fox-Kemper, Baylor, Ferrari, Raffaele & Hallberg, Robert 2008 Parameterization of mixed layer eddies. Part I: Theory and diagnosis. *Journal of Physical Oceanography* **38** (6), 1145–1165.

Frants, Marina, Damerell, Gillian M, Gille, Sarah T, Heywood, Karen J, MacKinnon, Jennifer & Sprintall, Janet 2013 An assessment of density-based finescale methods for estimating diapycnal diffusivity in the Southern Ocean. *Journal of Atmospheric and Oceanic Technology* **30** (11), 2647–2661.

Frehlich, Rod 1992 Laser scintillation measurements of the temperature spectrum in the atmospheric surface layer. *Journal of the atmospheric sciences* **49** (16), 1494–1509.

Frehlich, Rod & Sharman, Robert 2004 Estimates of turbulence from numerical weather prediction model output with applications to turbulence diagnosis and data assimilation. *Monthly Weather Review* **132** (10), 2308–2324.

Galbraith, Peter S & Kelley, Dan E 1996 Identifying overturns in CTD profiles. *Journal of Atmospheric and Oceanic Technology* **13** (3), 688–702.

Ganachaud, Alexandre, Cravatte, Sophie, Melet, A, Schiller, A, Holbrook, NJ, Sloyan, BM, Widlansky, MJ, Bowen, M, Verron, J, Wiles, P & others 2014 The Southwest Pacific Ocean circulation and climate experiment (SPICE). *Journal of Geophysical Research: Oceans* **119** (11), 7660–7686.

Ganachaud, Alexandre, Cravatte, Sophie, Sprintall, Janet, Germineaud, Cyril, Alberty, Marion, Jeandel, Catherine, Eldin, Gerard, Metzl, Nicolas, Bonnet, Sophie, Benavides, Mar & others 2017 The Solomon Sea: its circulation, chemistry, geochemistry and biology explored during two oceanographic cruises. *Elem Sci Anth* **5**.

Gasparin, Florent, Ganachaud, Alexandre, Maes, Christophe, Marin, Frédéric & Eldin, Gérard 2012 Oceanic transports through the Solomon Sea: the bend of the New Guinea Coastal Undercurrent. *Geophysical Research Letters* **39** (15).

Germineaud, Cyril, Ganachaud, Alexandre, Sprintall, Janet, Cravatte, Sophie, Eldin, Gérard, Alberty, Marion S & Privat, Emilien 2016 Pathways and Water Mass Properties of the Thermocline and Intermediate Waters in the Solomon Sea. *Journal of Physical Oceanography* **46** (10), 3031–3049.

Gourdeau, Lionel, Verron, J, Melet, A, Kessler, W, Marin, Frédéric & Djath, B 2014 Exploring the mesoscale activity in the Solomon Sea: A complementary approach with a numerical model and altimetric data. *Journal of Geophysical Research: Oceans* **119** (4), 2290–2311.

Gregg, MC 1989 Scaling turbulent dissipation in the thermocline. *Journal of Geophysical Research: Oceans* **94** (C7), 9686–9698.

Grenier, Mélanie, Cravatte, Sophie, Blanke, Bruno, Menkes, Christophe, Koch-Larrouy, Ariane, Durand, Fabien, Mélet, Angélique & Jeandel, Catherine 2011 From the western boundary currents to the Pacific Equatorial Undercurrent: Modeled pathways and water mass evolutions. *Journal of Geophysical Research: Oceans* **116** (C12).

Grenier, Mélanie, Jeandel, Catherine & Cravatte, Sophie 2014 From the subtropics to the equator in the Southwest Pacific: Continental material fluxes quantified using neodymium data along modeled thermocline water pathways. *Journal of Geophysical Research: Oceans* **119** (6), 3948–3966.

Hristova, Hristina G & Kessler, William S 2012 Surface Circulation in the Solomon Sea Derived from Lagrangian Drifter Observations*. *Journal of Physical Oceanography* **42** (3), 448–458.

Hristova, Hristina G, Kessler, William S, McWilliams, James C & Molemaker, M Jeroen 2014 Mesoscale variability and its seasonality in the Solomon and Coral Seas. *Journal of Geophysical Research: Oceans* **119** (7), 4669–4687.

Hu, DX, Cui, MC, Qu, TD & Li, YX 1991 A subsurface northward current off Mindanao identified by dynamic calculation. *Elsevier oceanography series* **54**, 359–365.

Jackson, Jennifer M, Carmack, EC, McLaughlin, FA, Allen, Susan E & Ingram, RG 2010 Identification, characterization, and change of the near-surface temperature maximum in the canada basin, 1993–2008. *Journal of Geophysical Research: Oceans* **115** (C5).

Jackson, Jennifer M, Williams, William J & Carmack, Eddy C 2012 Winter sea-ice melt in the Canada Basin, Arctic Ocean. *Geophysical Research Letters* **39** (3).

Johnson, Gregory C & McPhaden, Michael J 1999 Interior pycnocline flow from the subtropical to the equatorial Pacific Ocean. *Journal of Physical Oceanography* **29** (12), 3073–3089.

JPL MUR MEaSUREs Project 2015 GHRSST Level 4 MUR Global Foundation Sea Surface Temperature Analysis (v4.1). Ver. 4.1. PO.DAAC,CA,USA. Dataset accessed [2018-03-09] at http://dx.doi.org/10.5067/GHGMR-4FJ04.

JPL/OBPG/RSMAS 2016*a* GHRSST Level 2P Global Skin Sea Surface Temperature from the Moderate Resolution Imaging Spectroradiometer (MODIS) on the NASA Aqua satellite. Ver. 2014.0. PO.DAAC,CA,USA. Dataset accessed [2018-07-31] at http://dx.doi.org/10.5067/GHMDA-2PJ02.

JPL/OBPG/RSMAS 2016*b* GHRSST Level 2P Global Skin Sea Surface Temperature from the Moderate Resolution Imaging Spectroradiometer (MODIS) on the NASA Terra satellite. Ver. 2014.0. PO.DAAC,CA,USA. Dataset accessed [2018-07-31] at http://dx.doi.org/10.5067/GHMDT-2PJ02.

Kashino, Yuji, Ueki, Iwao, Kuroda, Yoshifumi & Purwandani, Andri 2007 Ocean variability north of New Guinea derived from TRITON buoy data. *Journal of oceanography* **63** (4), 545–559.

Kawabe, Masaki, Kashino, Yuji & Kuroda, Yoshifumi 2008 Variability and Linkages of New Guinea coastal undercurrent and lower equatorial intermediate current. *Journal of Physical Oceanography* **38** (8), 1780–1793.

Kessler, William S & Cravatte, Sophie 2013 Mean circulation of the Coral Sea. *Journal of Geophysical Research: Oceans* **118** (12), 6385–6410.

KESSLER, WILLIAM S & GOURDEAU, LIONEL 2007 The annual cycle of circulation of the southwest subtropical pacific, analyzed in an ocean gcm. *Journal of Physical Oceanography* **37** (6), 1610–1627.

KIDA, SHINICHIRO & WIJFFELS, SUSAN 2012 The impact of the Indonesian Throughflow and tidal mixing on the summertime sea surface temperature in the western Indonesian Seas. *Journal of Geophysical Research: Oceans* **117** (C9).

KILPATRICK, KA, PODESTÁ, G, WALSH, S, WILLIAMS, E, HALLIWELL, V, SZCZODRAK, M, BROWN, OB, MINNETT, PJ & EVANS, R 2015 A decade of sea surface temperature from MODIS. *Remote Sensing of Environment* **165**, 27–41.

KLYMAK, JODY M, CRAWFORD, WILLIAM, ALFORD, MATTHEW H, MACKINNON, JENNIFER A & PINKEL, ROBERT 2015 Along-isopycnal variability of spice in the North Pacific. *Journal of Geophysical Research: Oceans* **120** (3), 2287–2307.

KLYMAK, JODY M, MOUM, JAMES N, NASH, JONATHAN D, KUNZE, ERIC, GIRTON, JAMES B, CARTER, GLENN S, LEE, CRAIG M, SANFORD, THOMAS B & GREGG, MICHAEL C 2006 An estimate of tidal energy lost to turbulence at the Hawaiian Ridge. *Journal of Physical Oceanography* **36** (6), 1148–1164.

KLYMAK, JODY M, PINKEL, ROBERT & RAINVILLE, LUC 2008 Direct breaking of the internal tide near topography: Kaena Ridge, Hawaii. *Journal of Physical Oceanography* **38** (2), 380–399.

KOCH-LARROUY, ARIANE, ATMADIPOERA, AGUS, VAN BEEK, PIETER, MADEC, GURVAN, AUCAN, JÉRÔME, LYARD, FLORENT, GRELET, JACQUES & SOUHAUT, MARC 2015 Estimates of tidal mixing in the Indonesian archipelago from multidisciplinary INDOMIX in-situ data. *Deep Sea Research Part I: Oceanographic Research Papers* **106**, 136–153.

KOCH-LARROUY, ARIANE, LENGAIGNE, MATTHIEU, TERRAY, PASCAL, MADEC, GURVAN & MASSON, SEBASTIEN 2010 Tidal mixing in the Indonesian Seas and its effect on the tropical climate system. *Climate Dynamics* **34** (6), 891–904.

KOCH-LARROUY, ARIANE, MADEC, GURVAN, BOURUET-AUBERTOT, PASCALE, GERKEMA, THEO, BESSIÈRES, LAURENT & MOLCARD, ROBERT 2007 On the transformation of Pacific Water into Indonesian Throughflow Water by internal tidal mixing. *Geophysical Research Letters* **34** (4).

KOLMOGOROV, ANDREY NIKOLAEVICH 1941 The local structure of turbulence in incompressible viscous fluid for very large Reynolds numbers. In *Dokl. Akad. Nauk SSSR*, , vol. 30, pp. 299–303.

KUNZE, ERIC, FIRING, ERIC, HUMMON, JULIA M, CHERESKIN, TERESA K & THURNHERR, ANDREAS M 2006 Global abyssal mixing inferred from lowered ADCP shear and CTD strain profiles. *Journal of Physical Oceanography* **36** (8), 1553–1576.

Kunze, E, Klymak, JM, Lien, R-C, Ferrari, R, Lee, CM, Sundermeyer, MA & Goodman, L 2015 Submesoscale water-mass spectra in the Sargasso Sea. *Journal of Physical Oceanography* **45** (5), 1325–1338.

Kwok, R, Cunningham, GF, Wensnahan, M, Rigor, I, Zwally, HJ & Yi, D 2009 Thinning and volume loss of the Arctic Ocean sea ice cover: 2003–2008. *Journal of Geophysical Research: Oceans* **114** (C7).

Labatut, M, Lacan, F, Pradoux, C, Chmeleff, J, Radic, A, Murray, James W, Poitrasson, Franck, Johansen, AM & Thil, F 2014 Iron sources and dissolved-particulate interactions in the seawater of the Western Equatorial Pacific, iron isotope perspectives. *Global Biogeochemical Cycles* **28** (10), 1044–1065.

Large, William G, McWilliams, James C & Doney, Scott C 1994 Oceanic vertical mixing: A review and a model with a nonlocal boundary layer parameterization. *Reviews of Geophysics* **32** (4), 363–403.

Levine, Murray D & Boyd, Timothy J 2006 Tidally forced internal waves and overturns observed on a slope: Results from HOME. *Journal of physical oceanography* **36** (6), 1184–1201.

Lindstrom, Eric, Butt, Jeffrey, Lukas, Roger & Godfrey, Stuart 1990 The flow through Vitiaz Strait and St. George's Channel, Papua New Guinea. In *The Physical Oceanography of Sea Straits*, pp. 171–189. Springer.

Lindstrom, Eric, Lukas, Roger, Fine, Rana, Firing, Eric, Godfrey, Stuart, Meyers, Gary & Tsuchiya, Mizuki 1987 The western equatorial Pacific Ocean circulation study. *Nature* **330** (6148), 533–537.

Mackey, DJ, O'Sullivan, JE OSullivan & Watson, RJ 2002 Iron in the western Pacific: a riverine or hydrothermal source for iron in the Equatorial Undercurrent? *Deep Sea Research Part I: Oceanographic Research Papers* **49** (5), 877–893.

MacKinnon, Jennifer A, Nash, Jonathan D, Alford, Matthew H, Lucas, Andrew J, Mickett, John B, Shroyer, Emily L, Waterhouse, Amy F, Tandon, Amit, Sengupta, Debasis, Mahadevan, Amala & others 2016 A tale of two spicy seas. *Oceanography* **29** (2), 50–61.

Mahadevan, Amala 2006 Modeling vertical motion at ocean fronts: Are nonhydrostatic effects relevant at submesoscales? *Ocean Modelling* **14** (3-4), 222–240.

Mahadevan, Amala & Tandon, Amit 2006 An analysis of mechanisms for submesoscale vertical motion at ocean fronts. *Ocean Modelling* **14** (3-4), 241–256.

Mater, Benjamin D, Venayagamoorthy, Subhas K, St. Laurent, Louis & Moum, James N 2015 Biases in Thorpe-scale estimates of turbulence dissipation.

Part I: Assessments from large-scale overturns in oceanographic data. *Journal of Physical Oceanography* **45** (10), 2497–2521.

Maykut, GA & McPhee, Miles G 1995 Solar heating of the Arctic mixed layer. *Journal of Geophysical Research: Oceans* **100** (C12), 24691–24703.

McCartney, MS 1977 Subantarctic mode water. in. *A Voyage of Discovery, Deep Sea Research* **24**, 103–119.

McCreary, Julian P & Lu, Peng 1994 Interaction between the subtropical and equatorial ocean circulations: The subtropical cell. *Journal of Physical Oceanography* **24** (2), 466–497.

McLaughlin, Fiona, Carmack, Eddy, Proshutinsky, Andrey, Krishfield, Richard A, Guay, Christopher, Yamamoto-Kawai, Michiyo, Jackson, Jennifer M & Williams, Bill 2011 The rapid response of the Canada Basin to climate forcing: From bellwether to alarm bells. *Oceanography* **24** (3), 146–159.

McPhee, Miles G, Kikuchi, Takashi, Morison, James H & Stanton, Timothy P 2003 Ocean-to-ice heat flux at the North Pole environmental observatory. *Geophysical Research Letters* **30** (24).

Melet, Angélique, Gourdeau, Lionel, Kessler, William S, Verron, Jacques & Molines, Jean-Marc 2010*a* Thermocline Circulation in the Solomon Sea: A Modeling Study*. *Journal of Physical Oceanography* **40** (6), 1302–1319.

Melet, Angélique, Gourdeau, Lionel & Verron, Jacques 2010*b* Variability in Solomon Sea circulation derived from altimeter sea level data. *Ocean dynamics* **60** (4), 883–900.

Melet, Angélique, Gourdeau, Lionel, Verron, Jacques & Djath, Bughsin 2013 Solomon Sea circulation and water mass modifications: response at ENSO timescales. *Ocean Dynamics* **63** (1), 1–19.

Melet, Angélique, Legg, Sonya & Hallberg, Robert 2016 Climatic Impacts of Parameterized Local and Remote Tidal Mixing. *Journal of Climate* **29** (10), 3473–3500.

Melet, Angélique, Verron, Jacques, Gourdeau, Lionel & Koch-Larrouy, Ariane 2011 Equatorward pathways of Solomon Sea water masses and their modifications. *Journal of Physical Oceanography* **41** (4), 810–826.

Mensa, JA, Timmermans, M-L, Kozlov, IE, Williams, WJ & Özgökmen, TM 2018 Surface Drifter Observations From the Arctic Ocean's Beaufort Sea: Evidence for Submesoscale Dynamics. *Journal of Geophysical Research: Oceans* **123** (4), 2635–2645.

Molemaker, M Jeroen, McWilliams, James C & Dewar, William K 2015 Submesoscale instability and generation of mesoscale anticyclones near a separation of the california undercurrent. *Journal of Physical Oceanography* **45** (3), 613–629.

Morgan, Phillip P 1994 *SEAWATER: A library of MATLAB computational routines for the properties of sea water: Version 1.2*. CSIRO Marine Laboratories.

Moum, JN & Nash, JD 2009 Mixing measurements on an equatorial ocean mooring. *Journal of Atmospheric and Oceanic Technology* **26** (2), 317–336.

Moum, James N, Perlin, Alexander, Nash, Jonathan D & McPhaden, Michael J 2013 Seasonal sea surface cooling in the equatorial Pacific cold tongue controlled by ocean mixing. *Nature* **500** (7460), 64–67.

Munk, Walter & Wunsch, Carl 1998 Abyssal recipes II: energetics of tidal and wind mixing. *Deep Sea Research Part I: Oceanographic Research Papers* **45** (12), 1977–2010.

Murray, S, Lindstrom, E, Kindle, J & Weeks, E 1995 Transport through Vitiaz Strait. *WOCE notes* **7** (1), 21–23.

Niiler, PP 1977 One-dimensional models of the upper ocean. *Modelling and Prediction of the Upper Layers of the Ocean* pp. 143–172.

Niwa, Yoshihiro & Hibiya, Toshiyuki 2014 Generation of baroclinic tide energy in a global three-dimensional numerical model with different spatial grid resolutions. *Ocean Modelling* **80**, 59–73.

Oakey, NS 1982 Determination of the rate of dissipation of turbulent energy from simultaneous temperature and velocity shear microstructure measurements. *Journal of Physical Oceanography* **12** (3), 256–271.

Oboukhov, AM 1949 Structure of the temperature field in turbulent flows. *Isv. Geogr. Geophys. Ser.* **13**, 58–69.

Osborn, TR 1980 Estimates of the local rate of vertical diffusion from dissipation measurements. *Journal of Physical Oceanography* **10** (1), 83–89.

Paduan, Jeffrey D & Washburn, Libe 2013 High-frequency radar observations of ocean surface currents. *Annual review of marine science* **5**, 115–136.

Peltier, WR & Caulfield, CP 2003 Mixing efficiency in stratified shear flows. *Annual review of fluid mechanics* **35** (1), 135–167.

Pennington, J Timothy, Mahoney, Kevin L, Kuwahara, Victor S, Kolber, Dorota D, Calienes, Ruth & Chavez, Francisco P 2006 Primary production in the eastern tropical Pacific: A review. *Progress in Oceanography* **69** (2), 285–317.

Perovich, Donald K, Light, Bonnie, Eicken, Hajo, Jones, Kathleen F, Runciman, Kay & Nghiem, Son V 2007 Increasing solar heating of the Arctic Ocean and adjacent seas, 1979–2005: Attribution and role in the ice-albedo feedback. *Geophysical Research Letters* **34** (19).

Perovich, Donald K, Richter-Menge, Jacqueline A, Jones, Kathleen F & Light, Bonnie 2008 Sunlight, water, and ice: Extreme Arctic sea ice melt during the summer of 2007. *Geophysical Research Letters* **35** (11).

Perovich, Donald K, Richter-Menge, Jacqueline A, Jones, Kathleen F, Light, Bonnie, Elder, Bruce C, Polashenski, Christopher, Laroche, Daniel, Markus, Thorsten & Lindsay, Ronald 2011 Arctic sea-ice melt in 2008 and the role of solar heating. *Annals of Glaciology* **52** (57), 355–359.

Polyakov, Igor V, Timokhov, Leonid A, Alexeev, Vladimir A, Bacon, Sheldon, Dmitrenko, Igor A, Fortier, Louis, Frolov, Ivan E, Gascard, Jean-Claude, Hansen, Edmond, Ivanov, Vladimir V & others 2010 Arctic Ocean warming contributes to reduced polar ice cap. *Journal of Physical Oceanography* **40** (12), 2743–2756.

Polzin, Kurt, Kunze, Eric, Hummon, Jules & Firing, Eric 2002 The finescale response of lowered ADCP velocity profiles. *Journal of Atmospheric and Oceanic Technology* **19** (2), 205–224.

Polzin, Kurt L, Naveira Garabato, Alberto C, Huussen, Tycho N, Sloyan, Bernadette M & Waterman, Stephanie 2014 Finescale parameterizations of turbulent dissipation. *Journal of Geophysical Research: Oceans* **119** (2), 1383–1419.

Polzin, Kurt L, Toole, John M & Schmitt, Raymond W 1995 Finescale parameterizations of turbulent dissipation. *Journal of physical oceanography* **25** (3), 306–328.

Price, James F & Yang, Jiayan 1998 Marginal sea overflows for climate simulations. In *Ocean Modeling and Parameterization*, pp. 155–170. Springer.

Qin, Xuerong, Gupta, Alex Sen & Van Sebille, Erik 2015 Variability in the origins and pathways of pacific equatorial undercurrent water. *Journal of Geophysical Research: Oceans* **120** (4), 3113–3128.

Qin, Xuerong, Menviel, Laurie, Sen Gupta, Alex & Sebille, Erik 2016 Iron sources and pathways into the Pacific Equatorial Undercurrent. *Geophysical Research Letters* **43** (18), 9843–9851.

Qu, Tangdong & Lindstrom, Eric J 2002 A climatological interpretation of the circulation in the western south pacific. *Journal of Physical Oceanography* **32** (9), 2492–2508.

Qu, Tangdong & Lindstrom, Eric J 2004 Northward intrusion of Antarctic Intermediate Water in the western Pacific. *Journal of Physical Oceanography* **34** (9), 2104–2118.

Qu, Tangdong, Mitsudera, Humio & Yamagata, Toshio 1998 On the western boundary currents in the Philippine Sea. *Journal of Geophysical Research: Oceans* **103** (C4), 7537–7548.

Radic, Amandine, Lacan, Francois & Murray, James W 2011 Iron isotopes in the seawater of the equatorial pacific ocean: New constraints for the oceanic iron cycle. *Earth and Planetary Science Letters* **306** (1-2), 1–10.

Rainville, Luc, Lee, Craig M & Woodgate, Rebecca A 2011 Impact of wind-driven mixing in the Arctic Ocean. *Oceanography* **24** (3), 136–145.

Reid, Joseph L 1997 On the total geostrophic circulation of the Pacific Ocean: flow patterns, tracers, and transports. *Progress in Oceanography* **39** (4), 263–352.

Reid Jr, Joseph L 1965 Intermediate waters of the Pacific Ocean. *Tech. Rep.*. SCRIPPS INSTITUTION OF OCEANOGRAPHY LA JOLLA CA.

Renosh, PR, Schmitt, Francois G & Loisel, Hubert 2015 Scaling analysis of ocean surface turbulent heterogeneities from satellite remote sensing: use of 2D structure functions. *PloS one* **10** (5), e0126975.

Rio, M-H, Mulet, S & Picot, N 2014 Beyond GOCE for the ocean circulation estimate: Synergetic use of altimetry, gravimetry, and in situ data provides new insight into geostrophic and Ekman currents. *Geophysical Research Letters* **41** (24), 8918–8925.

Rocha, Cesar B, Chereskin, Teresa K, Gille, Sarah T & Menemenlis, Dimitris 2016 Mesoscale to submesoscale wavenumber spectra in Drake Passage. *Journal of Physical Oceanography* **46** (2), 601–620.

Rudels, B, Anderson, LG & Jones, EP 1996 Formation and evolution of the surface mixed layer and halocline of the Arctic Ocean. *Journal of Geophysical Research: Oceans* **101** (C4), 8807–8821.

Ryan, John P, Ueki, Iwao, Chao, Yi, Zhang, Hongchun, Polito, Paulo S & Chavez, Francisco P 2006 Western Pacific modulation of large phytoplankton blooms in the central and eastern equatorial Pacific. *Journal of Geophysical Research: Biogeosciences (2005–2012)* **111** (G2).

Santiago-Mandujano, Fernando & Firing, Eric 1990 Mixed-layer shear generated by wind stress in the central equatorial pacific. *Journal of physical oceanography* **20** (10), 1576–1582.

Sarkar, Sutanu, Pham, Hieu T, Ramachandran, Sanjiv, Nash, Jonathan D, Tandon, Amit, Buckley, Jared, Lotliker, Aneesh A & Omand, Melissa M 2016 The interplay between submesoscale instabilities and turbulence in the surface layer of the Bay of Bengal. *Oceanography* **29** (2), 146–157.

Serreze, MC, Barrett, AP, Stroeve, JC, Kindig, DN & Holland, MM 2009 The emergence of surface-based Arctic amplification. *The Cryosphere* **3** (1), 11–19.

Serreze, Mark C & Barry, Roger G 2011 Processes and impacts of Arctic amplification: A research synthesis. *Global and planetary change* **77** (1-2), 85–96.

Shimada, Koji, Kamoshida, Takashi, Itoh, Motoyo, Nishino, Shigeto, Carmack, Eddy, McLaughlin, Fiona, Zimmermann, Sarah & Proshutinsky, Andrey 2006 Pacific Ocean inflow: Influence on catastrophic reduction of sea ice cover in the Arctic Ocean. *Geophysical Research Letters* **33** (8).

Simmons, Harper L & Alford, Matthew H 2012 Simulating the long-range swell of internal waves generated by ocean storms. *Oceanography* .

Simmons, Harper L, Hallberg, Robert W & Arbic, Brian K 2004 Internal wave generation in a global baroclinic tide model. *Deep Sea Research Part II: Topical Studies in Oceanography* **51** (25), 3043–3068.

Slemons, Lia, Paul, Barbara, Resing, Joseph & Murray, James W 2012 Particulate iron, aluminum, and manganese in the Pacific equatorial undercurrent and low latitude western boundary current sources. *Marine Chemistry* **142**, 54–67.

Slemons, Lia O, Murray, James W, Resing, Joseph, Paul, Barbara & Dutrieux, Pierre 2010 Western Pacific coastal sources of iron, manganese, and aluminum to the Equatorial Undercurrent. *Global Biogeochemical Cycles* **24** (3).

Smith, Walter HF & Sandwell, David T 1997 Global sea floor topography from satellite altimetry and ship depth soundings. *Science* **277** (5334), 1956–1962.

Sokolov, Serguei & Rintoul, Stephen 2000 Circulation and water masses of the southwest Pacific: WOCE section P11, Papua New Guinea to Tasmania. *Journal of Marine Research* **58** (2), 223–268.

SPICE Community 2012 Naming a western boundary current from Australia to the Solomon Sea. *CLIVAR Newsletter Exchanges No. 58* **17** (1), 28.

Srinivasan, Kaushik, McWilliams, James C, Renault, Lionel, Hristova, Hristina G, Molemaker, Jeroen & Kessler, William S 2017 Topographic and Mixed Layer Submesoscale Currents in the Near-Surface Southwestern Tropical Pacific. *Journal of Physical Oceanography* **47** (6), 1221–1242.

St Laurent, Louis 2008 Turbulent dissipation on the margins of the South China Sea. *Geophysical Research Letters* **35** (23).

St Laurent, LC, Simmons, HL & Jayne, SR 2002 Estimating tidally driven mixing in the deep ocean. *Geophysical Research Letters* **29** (23).

St. Laurent, Louis C, Toole, John M & Schmitt, Raymond W 2001 Buoyancy forcing by turbulence above rough topography in the abyssal Brazil Basin. *Journal of Physical Oceanography* **31** (12), 3476–3495.

Stroeve, Julienne C, Kattsov, Vladimir, Barrett, Andrew, Serreze, Mark, Pavlova, Tatiana, Holland, Marika & Meier, Walter N 2012 Trends in Arctic sea ice extent from CMIP5, CMIP3 and observations. *Geophysical Research Letters* **39** (16).

Talley, Lynne D 1999 Some aspects of ocean heat transport by the shallow, intermediate and deep overturning circulations. *Geophysical Monograph-American Geophysical Union* **112**, 1–22.

Talley, Lynne D & Sprintall, Janet 2005 Deep expression of the Indonesian Throughflow: Indonesian intermediate water in the South Equatorial Current. *Journal of Geophysical Research: Oceans* **110** (C10).

Thomas, Leif N, Tandon, Amit & Mahadevan, Amala 2008 Submesoscale processes and dynamics. *Ocean modeling in an Eddying Regime* **177**, 17–38.

Thomas, Leif N, Taylor, John R, D'Asaro, Eric A, Lee, Craig M, Klymak, Jody M & Shcherbina, Andrey 2016 Symmetric instability, inertial oscillations, and turbulence at the Gulf Stream front. *Journal of Physical Oceanography* **46** (1), 197–217.

Thomas, Leif N, Taylor, John R, Ferrari, Raffaele & Joyce, Terrence M 2013 Symmetric instability in the Gulf Stream. *Deep Sea Research Part II: Topical Studies in Oceanography* **91**, 96–110.

Thompson, Andrew F, Gille, Sarah T, MacKinnon, Jennifer A & Sprintall, Janet 2007 Spatial and temporal patterns of small-scale mixing in Drake Passage. *Journal of physical oceanography* **37** (3), 572–592.

Thorpe, SA 1977 Turbulence and mixing in a Scottish loch. *Philosophical Transactions of the Royal Society of London A: Mathematical, Physical and Engineering Sciences* **286** (1334), 125–181.

Timmermans, M-L 2015 The impact of stored solar heat on Arctic sea ice growth. *Geophysical Research Letters* **42** (15), 6399–6406.

Timmermans, Mary-Louise, Cole, Sylvia & Toole, John 2012 Horizontal density structure and restratification of the Arctic Ocean surface layer. *Journal of Physical Oceanography* **42** (4), 659–668.

Timmermans, Mary-Louise & Jayne, Steven R 2016 The Arctic Ocean spices up. *Journal of Physical Oceanography* **46** (4), 1277–1284.

Timmermans, Mary-Louise, Toole, John & Krishfield, Richard 2018 Warming of the interior Arctic Ocean linked to sea ice losses at the basin margins. *Science advances* **4** (8), eaat6773.

Timmermans, Mary-Louise & Winsor, Peter 2013 Scales of horizontal density structure in the Chukchi Sea surface layer. *Continental Shelf Research* **52**, 39–45.

Tomczak, Matthias & Godfrey, J Stuart 2013 *Regional oceanography: an introduction*. Elsevier.

Toole, John M, Timmermans, M-L, Perovich, Donald K, Krishfield, Richard A, Proshutinsky, Andrey & Richter-Menge, Jackie A 2010 Influences of the ocean surface mixed layer and thermohaline stratification on Arctic Sea ice in the central Canada Basin. *Journal of Geophysical Research: Oceans* **115** (C10).

Tsuchiya, Mizuki 1968 Upper waters of the intertropical Pacific Ocean. *Johns Hopkins Oceanographic Studies* **4**, 50p.

Tsuchiya, Mizuki 1981 The origin of the Pacific equatorial 13 C water. *Journal of Physical Oceanography* **11** (6), 794–812.

Tsuchiya, Mizuki 1991 Flow path of the Antarctic Intermediate Water in the western equatorial South Pacific Ocean. *Deep Sea Research Part A. Oceanographic Research Papers* **38**, S273–S279.

Tsuchiya, Mizuki, Lukas, Roger, Fine, Rana A, Firing, Eric & Lindstrom, Eric 1989 Source waters of the Pacific equatorial undercurrent. *Progress in Oceanography* **23** (2), 101–147.

Waterhouse, Amy F, MacKinnon, Jennifer A, Nash, Jonathan D, Alford, Matthew H, Kunze, Eric, Simmons, Harper L, Polzin, Kurt L, St. Laurent, Louis C, Sun, Oliver M, Pinkel, Robert & others 2014 Global patterns of diapycnal mixing from measurements of the turbulent dissipation rate. *Journal of Physical Oceanography* **44** (7), 1854–1872.

Waterman, Stephanie, Polzin, Kurt L, Naveira Garabato, Alberto C, Sheen, Katy L & Forryan, Alexander 2014 Suppression of internal wave breaking in the Antarctic Circumpolar Current near topography. *Journal of Physical Oceanography* **44** (5), 1466–1492.

Weller, RA, Rudnick, DL, Eriksen, CC, Polzin, KL, Oakey, NS, Toole, JW, Schmitt, RW & Pollard, RT 1991 Forced ocean response during the frontal air-sea interaction experiment. *Journal of Geophysical Research: Oceans* **96** (C5), 8611–8638.

Wentz, FJ, Scott, J, Hoffman, R, Leidner, M, Atlas, R & Ardizzone, J 2015 Remote Sensing Systems Cross-Calibrated Multi-Platform (CCMP) 6-hourly ocean vector wind analysis product on 0.25 deg grid, Version 2.0, 2012-2014. Remote Sensing Systems, Santa Rosa, CA. Available online at www.remss.com/measurements/ccmp. Accessed 23 Oct 2017.

Wesson, JC & Gregg, MC 1994 Mixing at Camarinal sill in the Strait of Gibraltar. *Journal of Geophysical Research: Oceans* **99** (C5), 9847–9878.

Whalen, CB, MacKinnon, JA & Talley, LD 2018 Large-scale impacts of the mesoscale environment on mixing from wind-driven internal waves. *Nature Geoscience* **11** (11), 842.

Whalen, CB, Talley, LD & MacKinnon, JA 2012 Spatial and temporal variability of global ocean mixing inferred from Argo profiles. *Geophysical Research Letters* **39** (18).

Whalen, Caitlin B, MacKinnon, Jennifer A, Talley, Lynne D & Waterhouse, Amy F 2015 Estimating the mean diapycnal mixing using a finescale strain parameterization. *Journal of Physical Oceanography* **45** (4), 1174–1188.

Winkel, David P, Gregg, Michael C & Sanford, Thomas B 2002 Patterns of shear and turbulence across the Florida Current. *Journal of physical oceanography* **32** (11), 3269–3285.

Wood, Kevin R, Bond, Nicholas A, Danielson, Seth L, Overland, James E, Salo, Sigrid A, Stabeno, Phyllis J & Whitefield, Jonathan 2015 A decade of environmental change in the Pacific Arctic region. *Progress in Oceanography* **136**, 12–31.

Zhang, Jinlun, Lindsay, Ron, Steele, Mike & Schweiger, Axel 2008 What drove the dramatic retreat of arctic sea ice during summer 2007? *Geophysical Research Letters* **35** (11).

Zhang, Yanwei & Moum, James N 2010 Inertial-convective subrange estimates of thermal variance dissipation rate from moored temperature measurements. *Journal of Atmospheric and Oceanic Technology* **27** (11), 1950–1959.

Zilberman, NV, Roemmich, DH & Gille, ST 2013 The mean and the time variability of the shallow meridional overturning circulation in the tropical South Pacific Ocean. *Journal of Climate* **26** (12), 4069–4087.